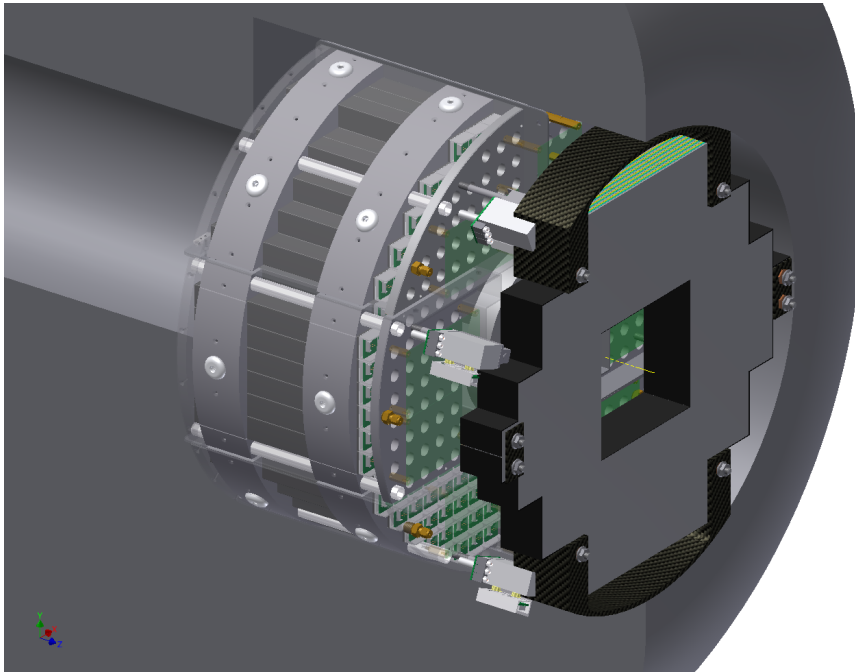# *A Proposal for the Muon Piston Calorimeter Extension (MPC-EX) to the PHENIX Experiment at RHIC*

Brookhaven National Laboratory

Relativistic Heavy Ion Collider

October, 2011

Introduction and Executive Summary

This is where the introduction and executive summary will go.

Contents

Chapter 1

Physics Overview

This is where the physics section (CNM and spin) will go.

1.1 Cold Nuclear Matter, the Initial State of the sQGP and low-x Physics

1.1.1 Introduction

The behavior of partons distributions in a heavy nucleus such as Au is of interest since the parton distributions are not simply a superposition of nucleon parton distributions, but display effects related the nuclear environment. These phenomena vary as a function of x. Of particular importance is the gluon distribution at low-x where a variety of models predict strong suppression. Very little is known about the gluon distribution function at x$< 10^{-2}$. Fig. 1.1 shows a variety of fits to the data of the gluon nuclear modification factor

$$R_g^A(x, Q^2) = \frac{f_g^A(x, Q^2)}{f_g^{proton}(x, Q^2)}$$

the ratio of the gluon distribution function in a nucleus as compared to the proton. A strong suppression could explain the reduction in p+A collisions relative to p+p collisions of pions, and pion pairs at forward rapidity [15, 5] as well as the stronger suppression of J/ψ at forward rapidity as compared to mid-rapidity [4].

The need to understand such effects has taken on a new urgency because of the discovery of the sQGP at RHIC. The measurement of the low-x gluon distribution of the nucleus, is the first step in understanding the formation of the sQGP since the bulk of the particles at $p_T \sim$ few times the initial temperature ($\sim$ 1 GeV, assuming an initial temperature of 300-600 MeV), are formed from gluons within a nucleus with x$< 10^{-2}$. It is crucial to make such a measurement both at RHIC and at the LHC, since the initial state for the formation of the sQGP, could be very different at the two machines. The pertinent x at RHIC is $\sim 10^{-2}$ and smaller, whereas at the LHC it is at least an order of magnitude lower, hence the relevant gluon distributions could be in a quite different region.

A variety of models have attempted to explain the suppressed cross sections at low-x, or forward rapidity. These fall into two classes. The first class of these models extend pQCD calculations into the non-pertubative regime, via the addition of multiple scattering or higher twist effects[14]. A second class of models is referred to as the Color Class Condensate (CGC)[30, 26] and assume that the density of gluons is high enough that to first order, they can be treated classically (quantum corrections are added as a second order effect). In its region of applicability the CGC is a rigorous QCD calculation with essentially one free parameter - the saturation scale Q$_{sat}$, although in practice other parameters or assumptions are invoked in order to make comparisons with experimental data. The two contrasting sorts of models could be two equivalent descriptions of the same phenomena, with one being more appropriate than the other depending on the kinematic range in question.

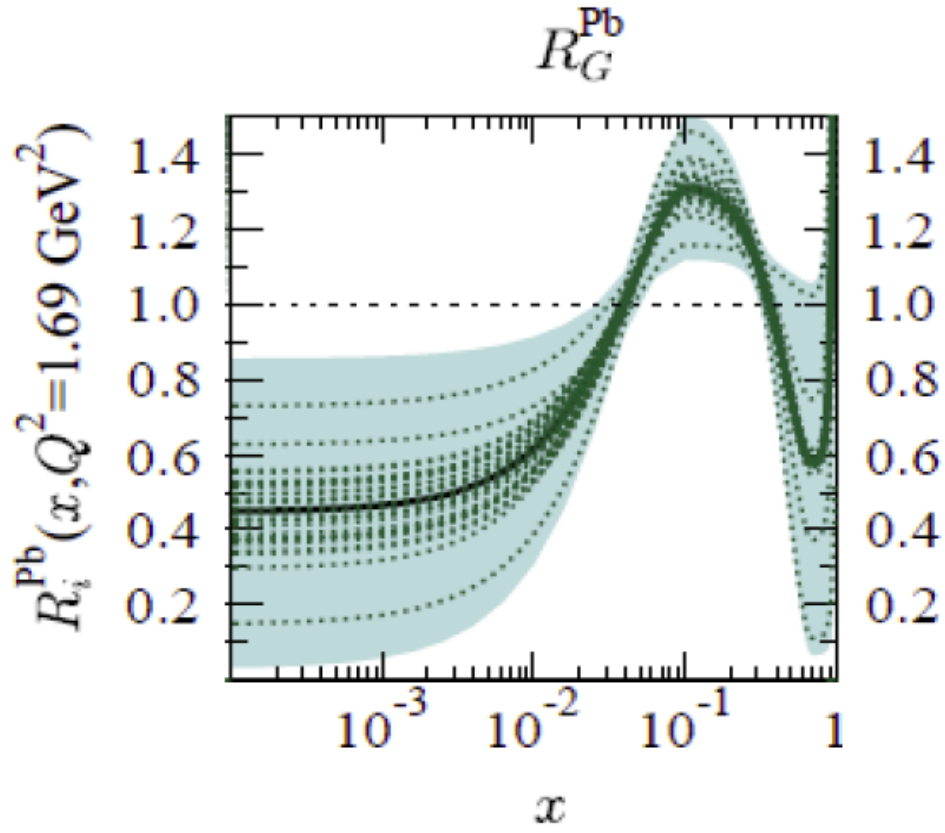The CGC is a non-pertubative model since it is for high density systems. However, it

Figure 1.1: EPS09 gluon nuclear modification ratio, i.e. the ratio between the gluon PDF in a heavy nucleus (Pb) and in a proton. The lines correspond to the various possibilities which are consistent with world data. At low x, there is virtually no constraint.

requires that the system be weakly interacting and is appropriate only in a regime in which the density is high enough that $\alpha_S(Q_{sat})$ is small. One must establish whether such calculations are applicable at RHIC. The partons which produce the bulk of particles constituting the hot-dense matter at RHIC have an $x_{BJ} \sim 10^{-2}$ with the saturation parameter Q_{sat} in the CGC model $\sim 3T_{init}$. Assuming a value of $T_{init} \sim$ 300-600 MeV, coming from the PHENIX thermal photon measurement, gives $Q_{sat} \sim$ 1-2 GeV/c[27]. This is on the edge of the boundary in which the CGC model is the correct description since $\alpha_S \sim 0.5$. Pion suppression and correlation data from RHIC[15, 5] seem to be consistent with the CGC hypothesis, however alternate explanations also may explain the data. It is almost certainly true, however, that the LHC, where the relevant x is less than 10^{-3}, is well into the saturation region. Mid-rapidity d+Au pion data at RHIC showed no suppression[6], while it is almost certain that similar data from the LHC will show suppression if the CGC model is correct. Hence, it is not clear that the initial conditions which lead to the formation of the sQGP at the two machines are the same.

For the purposes of this proposal, a parametrization of the modification of the gluon distribution function in nuclei, $R_g^A(x,Q^2)$, obtained by fitting deep-inelastic scattering

events, Drell Yan pairs, and RHIC mid-rapidity π^0s[23] is used and shown in fig. 1.1. The various lines represent different sets of parmetrizations consistent with the data, where the colored region corresponds to the 90% confidence level band. There is a large uncertainty at x$\sim 10^{-2}$.

Low-x phenomena can be studied using direct photon production at forward rapidities with the MPC-EX. Direct photons can be correlated with either a pion or a jet opposite in azimuth, to determine x_{gluon} to leading order with reasonable accuracy. In a CGC these opposite side correlated particles are suppressed since the recoil is absorbed by the CGC (like the Mossbauer effect). In fact the gluon PDF which gives the distribution of gluons with a fraction x of the nucleon's momentum, assumes a pQCD like picture, which is not consistent with the CGC model. In this case one can use three handles to constrain the theory: the rapidity dependence, centrality dependence (i.e. dependence on Q_{sat}), and the p_T balance of the recoiling particles. This would yield a centrality and x-dependent set of measurements, allowing a differentiation between various models. The x in question here would be the effective x as measured in the experiment since the variable x_{BJ} is not well defined in the CGC model. The centrality dependence of most pQCD inspired models follows a Glauber distribution, since they are proportional to the thickness function of the nucleus, while for the CGC it is given by the relationship between the saturation parameter Q_{sat} and the assumed gluon density. Other models, which involve radiative energy loss of quarks traversing cold nuclear matter or absorption, in the case of quarkonia show a non-linear behavior with the nuclear thickness function, uncharacteristic of the Glauber distribution as well. [references from Mike]. In addition, PHENIX data on the J/ψ already indicate that cold nuclear matter effects are non-linear. Such effects may be due to final state effects (absorption and energy loss), or initial state effects (e.g. the gluon PDF)[4].

Present data from d+Au collisions already shows a suppression of correlated pions[5] in a manner consistent with the CGC. Further theoretical analysis will be necessary to differentiate this interpretation from other nuclear effects. The analysis could also be complicated by the presence of hadron pairs arising from multiparton interactions (MPI)[35] in which case these pairs would not be made by this mechanism would not be probing the gluons at low-x.

Most importantly, however, a careful measurement of the gluons in a nucleus would set the initial conditions for the creating of the sQGP, which in turn would allow for the interpretation of jet and flow measurements in terms of interesting physical quantities, e.g. the sheer and bulk viscosity (Fig. 1.2), diffusion coefficients, the speed of sound, and the jet quenching parameter $\hat{q}$. Recall that for creation of the bulk hot-dense matter in A+A collisions, the relevant x is below 10^{-2}. For x_{gluon} less than 10^{-2}, as discussed above, there is very little constraint, hence the region most necessary for setting the initial state of the sQGP is not well known.

To give a specific example, one of the critical elements in the measurement of η/s is the geometric shape of the initial condition. The CGC model gives a larger initial eccentricity to the initial state which allows for a larger η/s. Specifically, if one assumes a Glauber

initial state one gets $\eta/s = 1/4\pi$ while a CGC initial condition yields a value about twice as high[29] (Fig. 1.2).
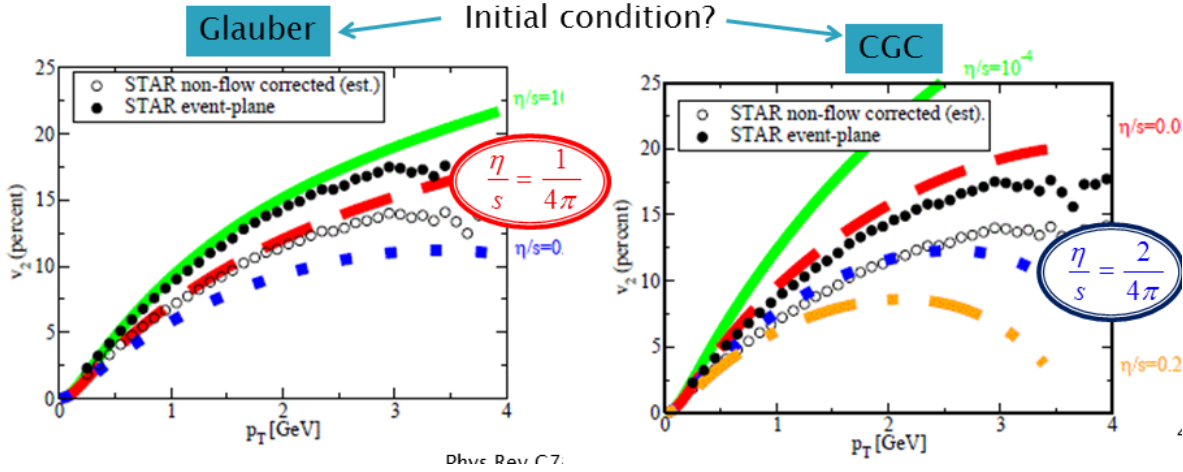

Figure 1.2: Fits of the elliptic flow parameter v_2 to Glauber initial conditions and CGC initial conditions for various values of η/s. One should compare theoretical curves to the non-flow corrected data points (open circles). Glauber initial conditions would favor a value near the conjectured lower bound from AdS/CFT calculations, while CGC would favor a value about twice that[29].

1.1.2   Direct Photons

Measurements at forward rapidity (low x), from hadrons have an ambiguity since they involve a fragmentation function. Direct photons originating from the primary vertex should clarify the situation. Fig. 1.3, left shows the basic first-order production diagram for direct photons at forward rapidities. The primary interaction is between a quark in the deuteron and the gluon of interest in the gold nucleus, producing an outgoing photon and jet.

Fig. 1.4 shows that the rapidity of the direct photon directly related to the x_2 of the gluon. Once the direct photon is observed the x_2 can be reasonably determined by including a correlation with a π^0 originating from the opposite side jet. If one assumes that the pseudorapidity of the pion is the same as the pseudorapidity of the jet, one can deduce the x_2 of the gluon to leading order through the relationship

$$x_2 = p_{T\gamma}(e^{-\eta_\gamma} + e^{-\eta_\pi})/\sqrt{s}$$

where $p_{T\gamma}$ and η_γ refer to the direct photon, η_π is the pseudorapidity of the π^0 and $\sqrt{s}$ is the nucleon-nucleon center of mass energy. We are currently exploring our capability to measure the complete jet to improve the resolution on x_{gluon}. Fig. 1.5 shows that the
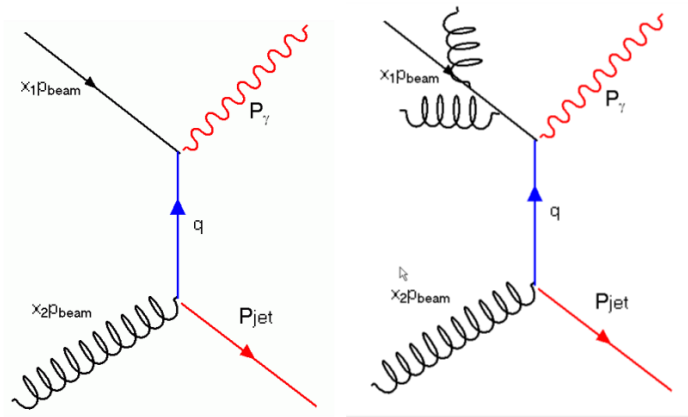
Figure 1.3: Diagrams for the production of direct photons in hadron-hadron collisions. To the left is a first order diagram, the right shows an example of a higher order diagram.
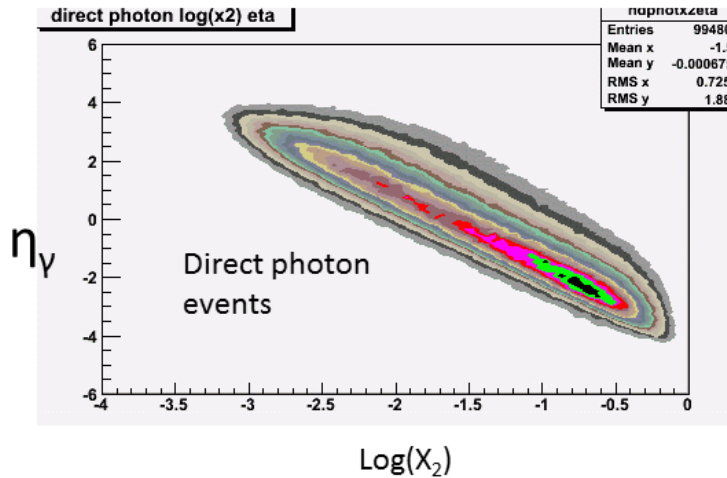

Figure 1.4: Direct photon events: η_γ vs log(x_2), showing the correlation between the pseudorapidity of the photon and x_2. In this figure no correlated hadron is required.

measured value of x_2 is nicely correlated with the true x_2 assuming that the first order scattering diagram dominates.

This will then allow us to vary the x of the gluon in the following manner. We first require that the direct photon be in the positive rapidity MPC-EX. To reach the lowest values of x, we require the correlated pion to be in the same MPC-EX (and be opposite in azimuth). To reach moderate values of x, we will require a hadron to be stopped in the positive rapidity muon arm (note that we only need the rapidity of the pion, and not its momentum). To reach yet higher values of x, we will require that the pion be in the VTX or central arms. We also plan also to measure the jet angle, using the MPC-EX on both sides, and the new silicon detectors - the VTX at mid-rapidity (installed in 2010) and and the FVTX at forward
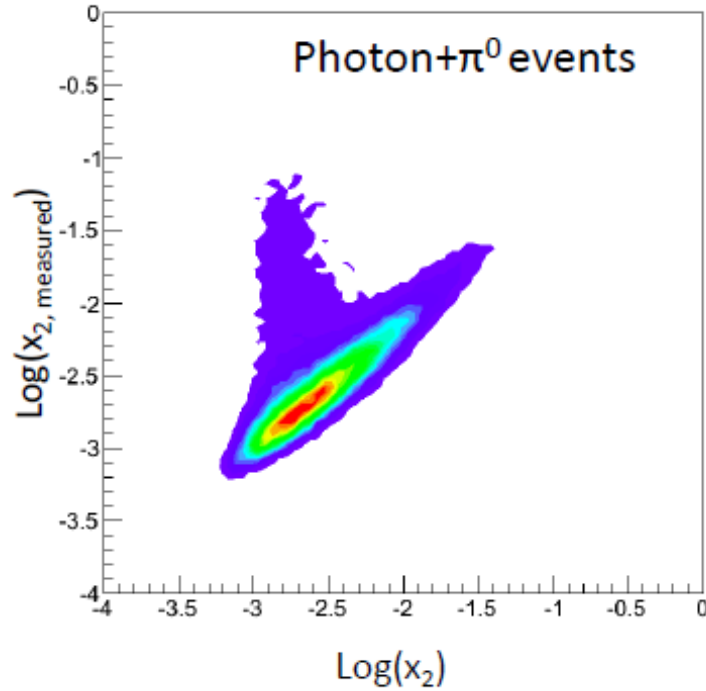
Figure 1.5: $x_{measured}$ vs x_2 as described in the text. The non-diagonal portion of the plot corresponds to cases in which the detected π^0 was did not give a good estimate of the direction of the outgoing jet, as in the case in which the detected pion was not the leading particle. Such events form about 10% of the events which had a detected photon and π^0 in the MPC-EX.

rapidity (to be installed in late 2011) to cover essentially the full range in x.

As mentioned previously, for the purposes of this proposal, we will quantify the capabilities of the MPC-EX assuming the suppression effects arise from modifications of the nuclear structure functions as parametrized in EPS09[23]. Shown in (Fig. 1.1 is a ratio of the nPDF to the nucleon PDF, and a range of possibilities consistent with world data. The spread of lines at low x reflects the lack of data needed to constrain the PDF - which the MPC-EX should provide.

If the effects of suppression are due to the suppression of the gluon nuclear structure function with no alteration of the outgoing jet, then the photon transverse momentum and the jet transverse momentum should balance, though higher order effects and or energy loss would smear out this relationship somewhat. In any case the standard fragmentation functions should be able to predict with reasonable accuracy the momentum of the outgoing pion. If however, as in the CGC case, the outgoing jet is strongly modified (since the balance in transverse momentum is taken up by the condensate as a whole), there should be a strong p_T imbalance if the jet is measured in the standard way by assuming a jet cone radius, or if one assumes that a leading pion carries a fraction of the momentum of the jet.

It will then be important to look at the direct photon, and study the characteristics of the outgoing particles on the other side to discriminate between a standard modification of the nPDF (ala EPS09) or a CGC model.

For the following illustration we assume that there is no modification of the outgoing jet, hence we are assuming that it is a good representation of what one might see in the case of a suppressed nPDF. We have added to the EPS09 distributions a centrality dependence coming from a Glauber model. Shown in Fig. 1.6 left, is the ratio

$$R_{dAu} = \frac{(dN/d\eta_\pi)_{dAu}}{N_{coll}(dN/d\eta_\pi)_{pp}}$$

, where we have required the direct photon to be in the MPC-EX and η_π is the pseudorapidity of the pion. Values for the central(black), the minimum(red) and maximum(blue) values of EPS09 are shown for central collisions, where "central", "minimum", and "maximum", refer to the central, minimum, and maximum values of the nuclear modification factor as given by Fig. 1.1.
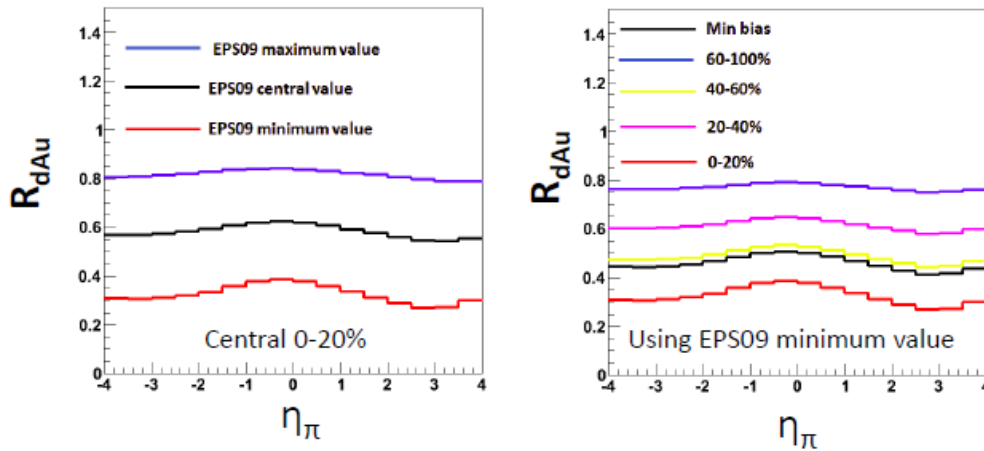

Figure 1.6: Left: R_{dAu} as measured in the MPC-EX vs η of the π^0 as described in the text. The three lines correspond to the EPS09 maximum, central and minimum values. Right: R_{dAu} as measured in the MPC-EX vs η of the π^0 as a function of centrality for EPS09 minimum values.

As mentioned previously a Glauber assumption is put into our model of EPS09. Fig. 1.6 right, shows the centrality dependent suppression. The CGC should show a different, somewhat flatter centrality dependence, with less dependence at the more central values and a steeper dependence for more peripheral events. The rapidity dependence (i.e. x dependence, where we note that for the CGC model, $x_{2,measured}$ may simply be an experimental parameter) should yield a value of Q_{sat}, or constrain the values of the nPDF. The models will probably have validity in different kinematic ranges - the CGC model at low-x and the nPDFs at higher x giving us a transition from the centrality dependence of the Glauber to CGC geometries as a function of η_π.

It must be said, as we conclude this section, that the interpretation of our results will need to be in close coordination with theorists, as in any measurement of a PDF, since, in reality the diagram shown in Fig. 1.3, left, is only a first order diagram, and higher orders (e.g Fig. 1.3,right) will contribute. What these measurements will give, however, are data to to clarify out understanding of cold nuclear matter and to constrain the initial condition leading to the formation of the sQGP.

1.2   Nucleon Spin Structure

1.2.1   Nucleon Structure: Transverse Spin Physics

Since the observation of surprisingly large single transverse spin asymmetries (SSAs) in $p^\uparrow + p \rightarrow \pi + X$ at Fermilab in the 1980s [?], the exploration of the physics behind the observed SSAs has become a very active research branch in hadron physics, and has played an important role in our efforts to understand QCD and nucleon structure. The field of transverse spin physics has now become one of the hot spots in high energy nuclear physics, generating tremendous excitements on both theoretical and experimental fronts. Fermilab E704's observation of large SSA [3] initially presented a challenge for QCD theorists, contradicted the general expectation from pQCD of vanishingly small SSA assuming it is originated from a helicity flip of a collinear parton. It was even more startling that the SSA discovered by E704 at $\sqrt{s} = 20$ GeV did not vanish at all, as expected from pQCD, at the much higher $\sqrt{s}$ of 62.4 GeV and 200 GeV from the BRAHMS [16] and the STAR [2] experiments. The surprisingly large SSA of π^0 mesons observed at STAR, as a function of Feynman x, is shown in Fig. 1.7. Although theory calculations based on a fit [21] of Sivers Transverse Momentum Dependent parton distributions (TMD) and a twist-3 calculation [28] roughly described the x_F dependencies of SSAs, they failed to describe the trend of transverse momentum (p_T) dependencies of SSA, as shown in Fig. 1.8. PHENIX preliminary results of forward rapidity "single-cluster" MPC hits (presumably π^0s) SSA A_N, as in Fig. 1.9, also showed similar large size asymmetries. One might question whether the forward reactions are hard enough to apply perturbative QCD, but as shown in Fig. 1.10 the cross sections of $p + p \rightarrow \pi^0 + X$ are reasonably described by NLO pQCD [?] as well as by PYTHIA simulations [33]. The existence of large single spin asymmetries at very forward rapidities at RHIC, along with the good theoretical understanding of the unpolarized cross-sections gives hope that transverse spin phenomena in polarized pp collisions at RHIC can be used as a tool to probe the correlation between parton's transverse motion and the nucleon's spin in order to provide a 3-dimensional topological image of the nucleon.

In order to explain these large single-spin asymmetry phenomena associated with transversely polarized $p + p$ collisions, three basic mechanisms have been introduced (although they can not be clearly separated from each other in inclusive hadron SSA measurements):

1. The "Collins Effect": quark's transverse spin [32] (transversity) generates a left-right bias during the (spin-dependent) quark fragmentation process [?].

2. The "Sivers Effect": parton's transverse motion generates a left-right bias [?]. The existence of the parton's Sivers distribution functions ($f_{1T}^\perp$), one of the eight leading order Transverse Momentum Dependent parton distributions (TMDs), which is naive T-odd and describes the correlation between parton's transverse momentum and the nucleon's transverse spin, allows a left-right bias to appear in the final
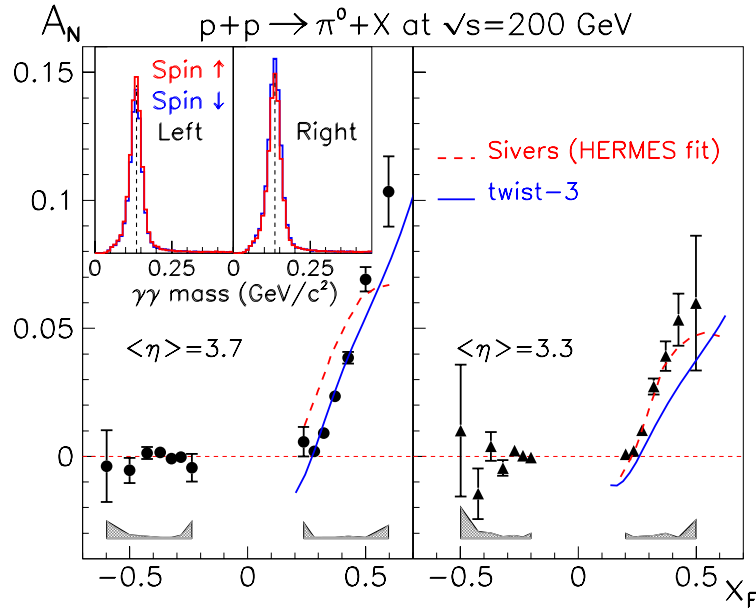
Figure 1.7: Single spin asymmetry A_N from π^0 mesons at two different forward rapidity bins ($\langle\eta\rangle = 3.3, 3.7$) as a function of Feynman x_F, measured at the STAR experiment from transversely polarized $p + p$ collisions at $\sqrt{s} = 200$ GeV [2]. The calculations are: i) a fit [21] of quark Sivers function from HERMES proton Sivers results, ii) a twist-3 calculation [28] as described later in the text. The inset shows examples of the spin-sorted invariant mass distributions. The vertical lines mark the π^0 mass.

    hadron's azimuthal distribution. This "TMD factorization approach" is valid in the low p_T region ($p_T \sim \Lambda_{QCD} \ll Q$).

3. The so-called "twist-3 colinear factorization approach", valid in high p_T region ($p_T \gg \Lambda_{QCD}$): a higher twist (twist-3) mechanism in the initial and/or final state [?] that describes SSA in terms of twist-3 transverse-spin-dependent correlations between quarks and gluons. It was shown theoretically that in the intermediate p_T region ($\Lambda_{QCD} \ll p_T \ll Q$) that overlap between the TMD factorization approach and the twist-3 approach, as in the case of SSAs measured at RHIC $p + p$ collisions, both methods describe the same physics such that a link between the moments of twist-3 three-parton correlation function $T_{q,F}(x, x)$, and the quark Sivers distribution $f_{1T}^{\perp q}(x)$ can be established [?, 25].

The Collins and the Sivers effects, although not possible to be separated in inclusive hadron SSA in $p + p$ collisions, can be clearly separated through azimuthal angle dependence of SSA measured in semi-inclusive deep-inelastic scattering (SIDIS) reactions. It has been a world-wide effort over the last several years to measure SSA in SIDIS reactions. The HERMES experiment at DESY carried out the first SSA measurement in SIDIS reaction on a transversely polarized proton target [7, 8]. The COMAPSS experiment at CERN carried out similar SSA measurements on transversely polarized deuteron and proton
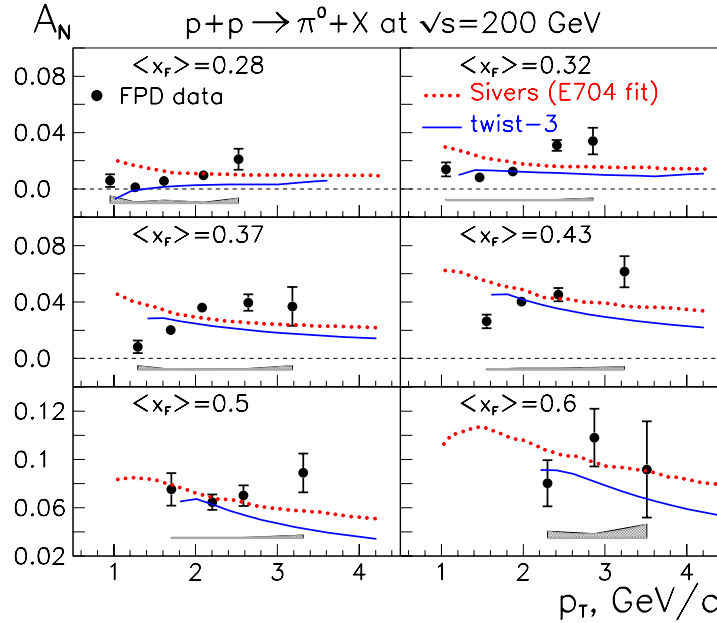
Figure 1.8: Data from STAR: Transverse momentum (p_T) dependence of Single spin asymmetry A_N in fixed x_F bins of π^0 mesons production in $p + p$ collisions at $\sqrt{s} = 200$ GeV. [2]. The calculations are: i) a fit [21] of quark Sivers function from HERMES proton Sivers results, ii) a twist-3 calculation [28] as described later in the text.
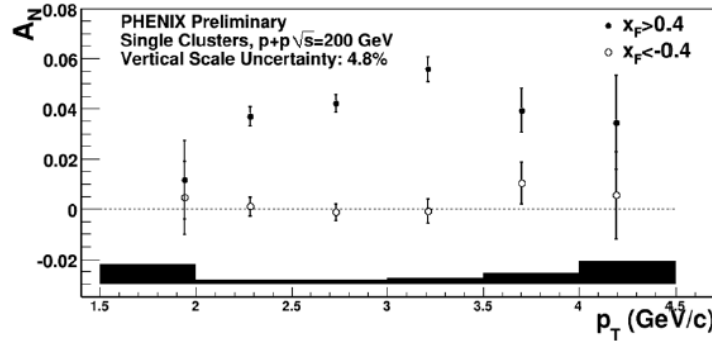

Figure 1.9: PHENIX preliminary results of single spin asymmetry A_N of forward rapidity MPC single-cluster hits (presumably π^0s) in $p + p$ collisions at $\sqrt{s} = 200$ GeV.

targets [9, 10]. Most recently, Jefferson Lab Hall A published results of SSA measurements on a transversely polarized neutron (^{3}He) target [31].

In the recent Transversity-2011 Workshop, the COMPASS Collaboration presented their new preliminary data of high statistic SSA results of 2010-run on a transversely polarized proton target [19], as shown in Fig. 1.11. The Collins SSA of proton for COMPASS and HERMES agree reasonably well in the overlapping kinematic region, and show clear non-zero SSA for both positively and negatively charged hadrons with opposite signs of
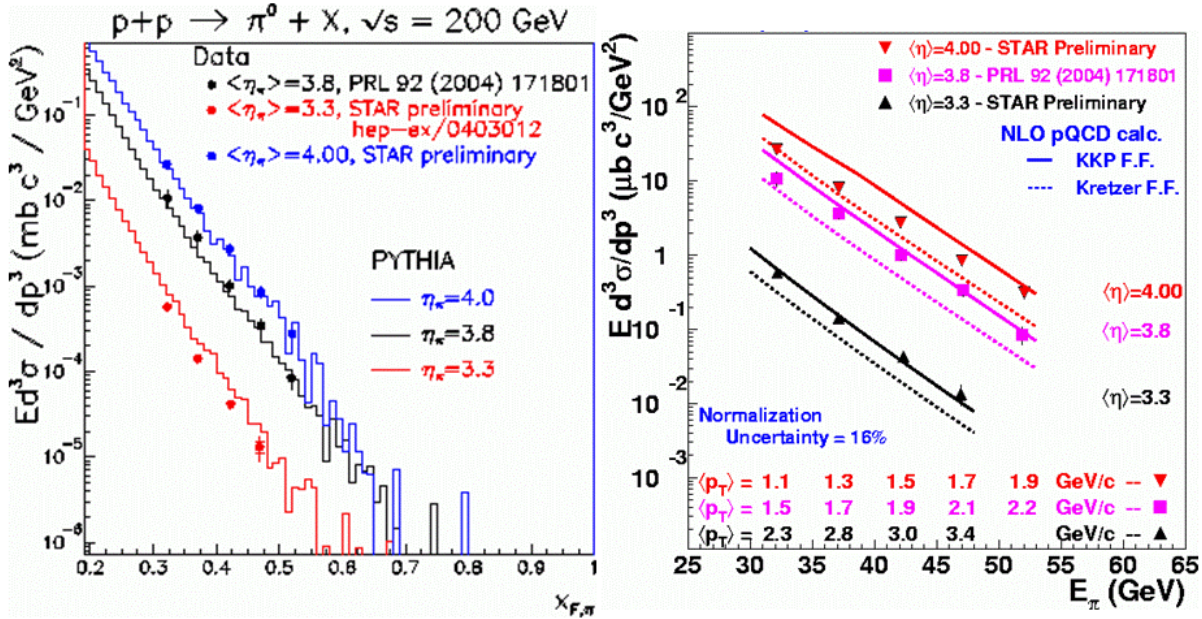
Figure 1.10: Forward inclusive π^0 cross sections measured at the STAR experiment from transversely polarized $p + p$ collisions at $\sqrt{s} = 200$ GeV [2]; the average pseudorapidity is $\langle \eta \rangle = 3.8$. In the left panel, these results are compared to predictions using PYTHIA [33] as a function of Feynman x; in the right panel they are compared to NLO pQCD [?] calculations as a function of the pion energy.

asymmetries.

The observed non-zero Collins asymmetry in SIDIS, which is related to the convolution products of the chiral-odd quark transversity distribution [32] with another chiral-odd object the "Collins Fragmentation Function" (F.F.), strongly indicated that both the quark transversity as well as the quark to hadron Collins F.F. are non-vanishing. The similar amplitudes and the opposite signs of positive-hadron SSA relative to that of the negative hadron indicated that the the up-quark transversity is opposite to that of down-quark, but similar in amplitudes, and the "unfavored" Collins F.F. is opposite in sign to that of the "favored" one, perhaps with an even larger amplitude. Independently, effects of non-zero Collins F.F. have been observed by the BELLE Collaboration [?] in e^+e^- annihilation and the quark to hadron Collins F.F. have been first extracted from these data [13].
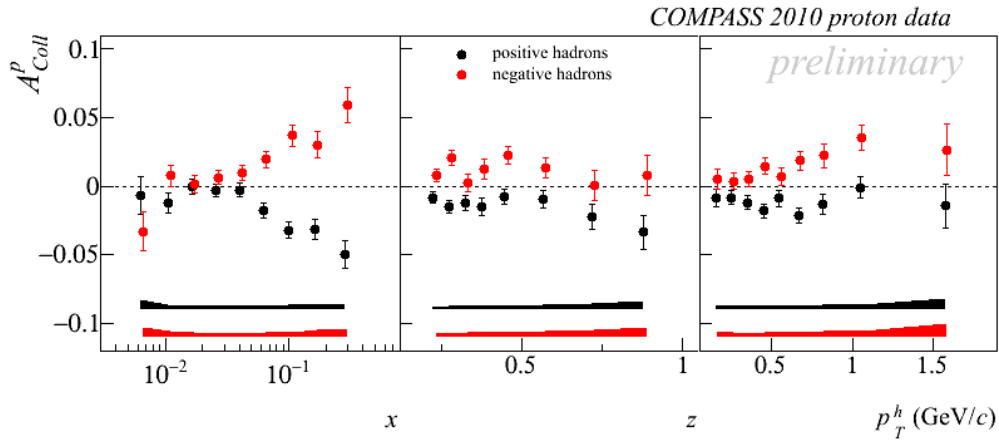
Figure 1.11: The COMPASS Collaboration's preliminary Collins single spin asymmetry results in semi-inclusive deep-inelastic scattering on a transversely polarized proton target [19].

The existence of non-zero Collins F.F. allows the extraction of the quark transversity distributions inside the nucleon. Transversity or $\delta q_f(x)$, is one of the three leading order quark distributions which survive the integration of quark transverse momentum. They are: quark momentum distribution $f_q(x)$, helicity distribution $\Delta f_q(x)$ and transversity distribution $\delta q_f(x)$. Quark transversity is a measure of the quark's spin-alignment along the nucleon's transverse spin direction, and it is different from that of helicity distribution since operations of rotations and boosts do not commute. The 0th-moment of transversity, $\sum_f \int_0^1 \delta q_f(x)dx$, yields nucleon's tensor-charge as one of the fundamental properties of the nucleon just like its charge and magnetic moment. Transversity requires a helicity change of 1-unit between the initial and the final state of the parton such that gluons, which have spin-1, are not allowed to have transversity. Therefore, quark transversity distribution is sensitive only to the valence quark spin structure, and its Q^2 evolution follows that of non-singlet densities which do not couple with any gluon related quantities, a completely different behavior compared to that of the longitudinal spin structure. These attributes provide an important test of our understanding of the anti-quark and gluon longitudinal spin structure functions, especially with regard to relativistic effects. Quark transversity distributions and quark spin-dependent Collins F.F. have been extracted from a QCD global fit [13] of published HERMES proton and COMPASS deuteron SIDIS Collins asymmetries in conjunction with the BELLE e^+e^- data. The results are shown in Fig. 1.12.

The "Sivers effect", and the quark Sivers distributions as a completely different mechanism, was thought to be forbidden since early 1990s due to its odd nature under the "naive" time-reversal operation. It was only in 2002 when Brodsky *et al.* [20] demonstrated that when quark's transverse motion is considered a left-right biased quark Sivers distribution is not only allowed, it could also be large enough to account for the large observed inclusive hadron SSAs in $p + p$ collisions. Subsequent SIDIS measurements have shown the existence of such non-zero Sivers SSAs, as summarized in Fig.1.13 for a comparison of proton Sivers
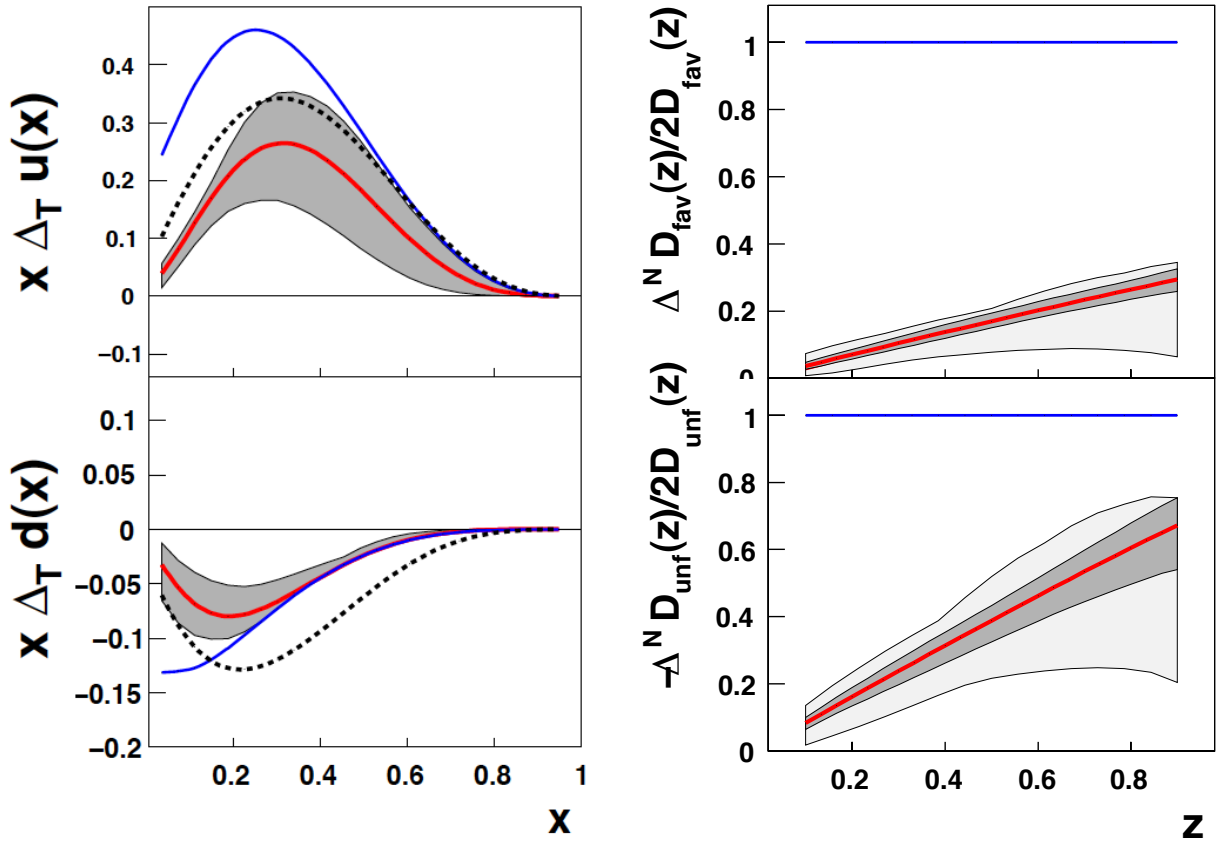
Figure 1.12: The quark transversity (left) distributions, and the Collins fragmentation functions (right) as extracted from SIDIS and e^+e^- data. In both cases the solid red curve indicates the distributions as determined by the global best fit to the data. The gray bands are an indication of the uncertainty in the extraction. In the left panel, the extracted transversity (solid line) is compared with the helicity distribution (dashed line) at $Q^2 = 2.4\,\text{GeV}^2$ and the Soffer positivity bound (blue solid line). In the right panel, the favored and the unfavored Collins fragmentation functions, at $Q^2 = 2.4\,\text{GeV}^2$; are compared with the positivity bound and the (wider) uncertainty bands obtained in an earlier fit.

SSA of preliminary COMPASS run-2010 data and the published HERMES data. Clear non-zero Sivers SSA are observed in the positive hadron (π^+ in HERMES) production, while the negative hadron (π^- in HERMES) SSA are consistent with zero, along with the COMPASS deuteron [10] π^+ and π^- Sivers SSA, indicating that up-quark and down-quark Sivers distributions are opposite in sign. Such pronounced flavor dependence of the quark Sivers functions were also indicated by a phenomenological fit [?] of the published proton and deuteron Sivers SSA data.

Since Sivers SSA is related to the convolution products of the quark Sivers distributions $f_{1T}^\perp$ and the "regular-type" spin-independent quark to hadron F.F., which are reasonably well-known through e^+e^- annihilation and SIDIS hadron production data, quark Sivers
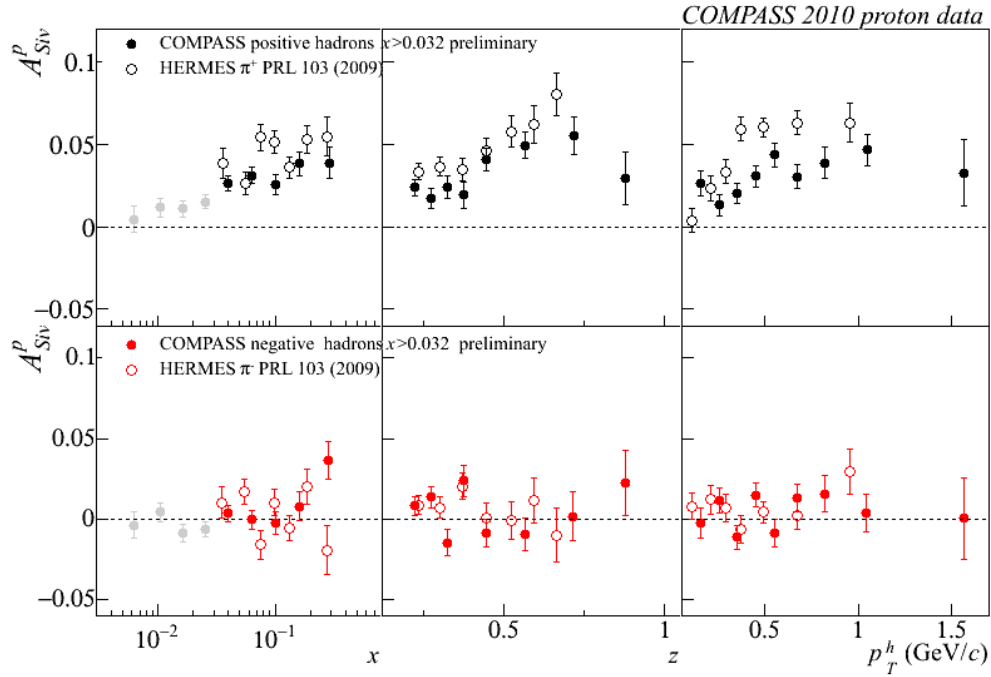
Figure 1.13: The COMPASS Collaboration's preliminary Sivers single spin asymmetry results in semi-inclusive deep-inelastic scattering on a transversely polarized proton target [19] compared with that of published HERMES data [7].

distributions have been extracted through global QCD fits [?] of existing SIDIS data, as shown in Fig. 1.14. Sivers function $f_{1T}^{\perp}$ represents a correlation between the nucleon spin and the quark transverse momentum, and it corresponds to the imaginary part of the interference between light-cone wave function components differing by one unit of orbital angular momentum [20]. A nonzero $f_{1T}^{\perp}$ arises due to initial (ISI) and/or final-state interactions (FSI) between the struck parton and the remnant of the polarized nucleon [20]. It was further demonstrated through gauge invariance that the same Sivers function, originates from a gauge link, would lead to SSAs in SIDIS from FSI and in Drell-Yan from ISI but with an opposite sign [?, ?]. This "modified universality" of quark Sivers distribution is an important test of the QCD gauge-link formalism, and the underline assumption of QCD factorization used to calculate these initial/final state colored interactions. A direct test of such a fundamental QCD prediction of Sivers function sign change between SIDIS and Drell-Yan has become a major challenge to spin physics, and it has been designated an DOE/NSAC milestone. Polarized Drell-Yan experiments are currently under preparation at COMPASS and at RHIC IP2, and in the planning stage for both STAR and PHENIX upgrades at RHIC and possibly for a fixed target Drell-Yan experiment at Fermilab. The existence of non-zero quark Sivers distributions is now generally accepted and well defined. Quark Sivers distribution provides an interesting window into the transverse structure of the nucleon, and provides constraints to quark's orbital angular momentum, although currently only in a model-dependent fashion. Recently, using a lattice-QCD

"inspired" assumption that links quark Sivers distribution with quark Generalized Parton Distributions E, quark total angular momentum (J^q) has been quantified [18] for the first time as: $J^u = 0.266 \pm 0.002^{+0.009}_{-0.014}$ and $J^d = -0.012 \pm 0.003^{+0.024}_{-0.006}$.
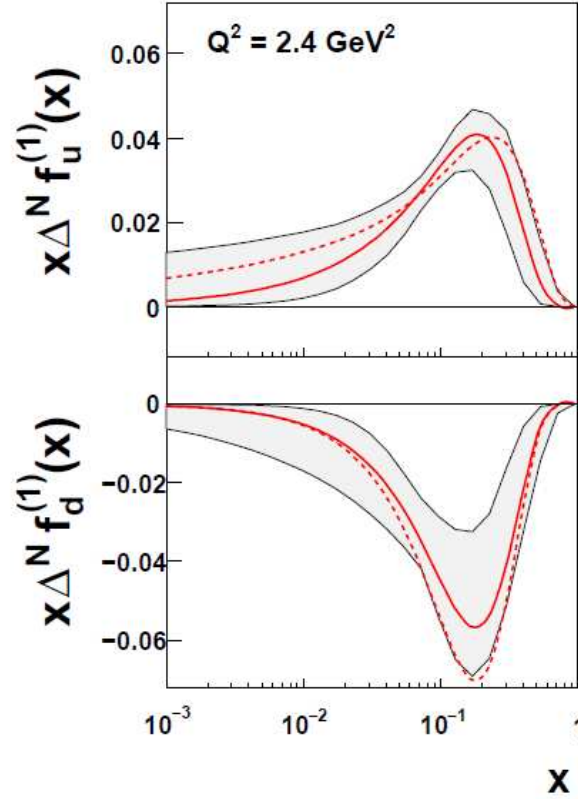

Figure 1.14: The quark Sivers distributions, as extracted from published SIDIS data. The gray bands are an indication of the uncertainty in the extraction.

Linking the Sivers effect with the twist-3 colinear factorization approach, the twist-3 transverse-spin-dependent quark-gluon correlation function $T_{q,F}(x,x)$ extracted from $p + p$ inclusive SSA data was shown to be directly related to the moments of Sivers functions, thus provide an independent check of our understanding of SSA phenomena in SIDIS and in $p + p$. However, very recent studies by Kang et al. showed that **the quark Sivers function moments extracted by these two methods are similar in size, but opposite in sign** [?], as shown in Fig. **??** for the up-quark (left) and the down-quark (right). The solid lines represent twist-3 approach "direct extraction" from $p + p$ inclusive SSA data, while the dashed and dotted lines represent Sivers functions extracted from published SIDIS data assuming two different functional forms. This controversy of Sivers function sign "mismatch" indicates either a serious flaw in our understanding of transverse spin phenomena, or alternatively drastic behaviors [22] of quark Sivers function in high momentum fraction (x) or in high transverse momentum (k_t). Given the facts that the existing SIDIS measurements are limited to $x \leq 0.35$, high precision $p + p$ SSA measurements at very forward rapidity are urgently needed to provide constraints in the high-x region.
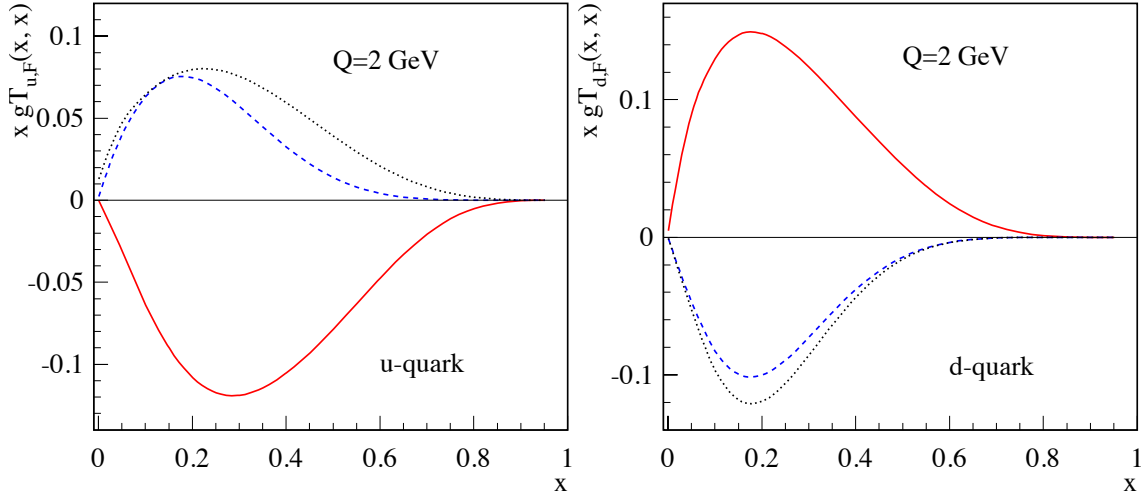
Figure 1.15: The quark-gluon correlation function $gT_{q,F}(x,x)$ as a function of momentum fraction x for u-quarks (left) and d-quarks (right). The solid lines represent "direct extraction" from $p+p$ inclusive SSA data in the twist-3 approach, while the dashed and dotted lines represent Sivers functions extracted from SIDIS data assuming two different functional forms.

Unlike polarized SIDIS reactions, SSA effects in forward hadron production in transversely polarized $p+p$ collisions are somewhat more complicated to interpret since both the Final State Interactions and the Initial State Interactions exist. From past observations, the single-spin effects in $p+p$ are typically larger than those of SIDIS, thus are much easier for experiments to measure. However, it has recently become clear that the theoretical interpretation of these measurements are hampered by issues related to universality and factorization [?]. The main goal of these types of $p+p$ measurements must be to clearly isolate individual effects in SSAs in order to gain a deeper understanding of the fundamental physics. The MPC-EX, along with the Muon Piston Calorimeter(MPC) and the standard PHENIX central and muon-arm detectors, will allow a series of transverse spin measurements to be carried out at PHENIX. Especially, with the capability to reconstruct "jet-like" structures in the forward rapidity, two kinds of SSA observables are of special interests to MPC-EX:

1. **Hadron azimuthal distribution asymmetry inside a jet ($A_N^{h\ in-jet}$) is purely originated from the Collins effect.**
   It is the quark's transverse spin (transversity) that generates such a left-right bias inside the jet. A measurement of $A_N^{h\ in-jet}$ will provide constraints on the product of quark transversity distributions and the Collins F.F. Specifically for MPC-EX, the left-right asymmetry of π^0 inside a jet ($A_N^{\pi^0\ in-jet}$) is a pure Collins effect. The experimental observable in MPC-EX would be the azimuthal distribution of π^0 yields around the jet axis reconstructed with the MPC-EX, and the azimuthal angle ϕ_S is between the proton spin direction $\vec{S}_p$ and the transverse momentum $\vec{k}_T$ of the

pion with respect to the jet axis, $\vec{p}_{jet}$ One advantage that such a measurement would have over existing SIDIS measurements would be that the x range measured for the transversity distribution would be substantially higher than that reached in SIDIS, see Fig. 1.17. While the next generation SIDIS experiments at JLab-12GeV will extend to high-x region starting in FY-2015, the current SIDIS data do not exceed beyond $x_{Bj} = 0.35$,

2. **The azimuthal asymmetry of inclusive jet (A_N^{jet}) is purely originated from the Sivers effect.**
   Collins effects do not contribute to A_N^{jet} as they wash out in the integration over the azimuthal angle of hadrons inside the jet. A measurement of A_N^{jet} will provide information on the product of quark Sivers distributions and the well-known spin-independent fragmentation functions. Predictions of A_N^{jet} in the MPC-EX acceptance are at a few % level with a large range of variations refelcting our lack of knowledge on quark Sivers functions at high-x, as shown in Fig. 1.16 The measurement of A_N^{jet} can be carried out with the MPC-EX by recording the jet yields for the different transverse proton spin orientations and constructing the relative luminosity corrected asymmetries between the yields for the up versus down proton spin orientations.

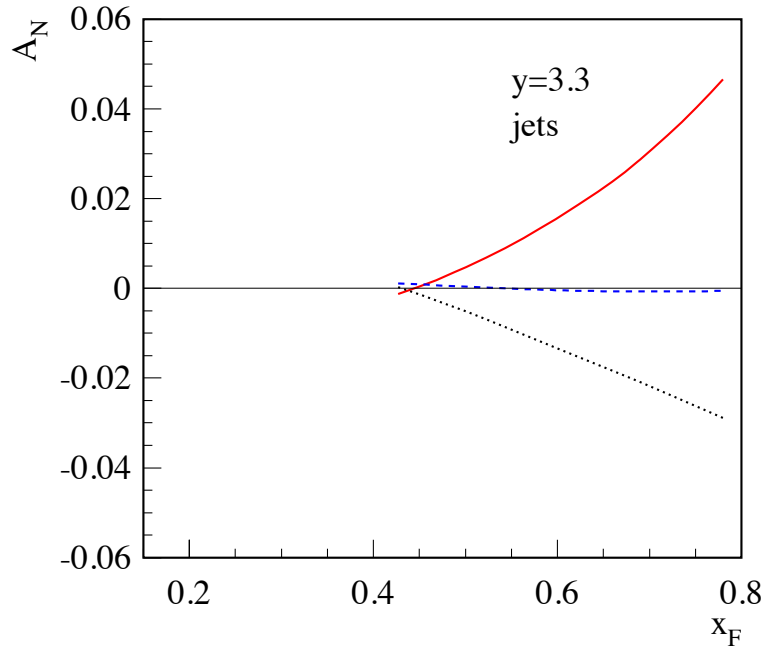**Figure 1.16:** The SSAs for inclusive jet production A_N^{jet} in $p^\uparrow p$ collisions [?] at $\sqrt{S} = 200$ GeV, as functions of x_F for rapidity $y = 3.3$. The solid lines represent "direct extraction" from $p + p$ inclusive SSA data in the twist-3 approach, while the dashed and dotted lines represent Sivers functions extracted from SIDIS data assuming two different functional forms.

(A plot to show x_1, x_2 here)
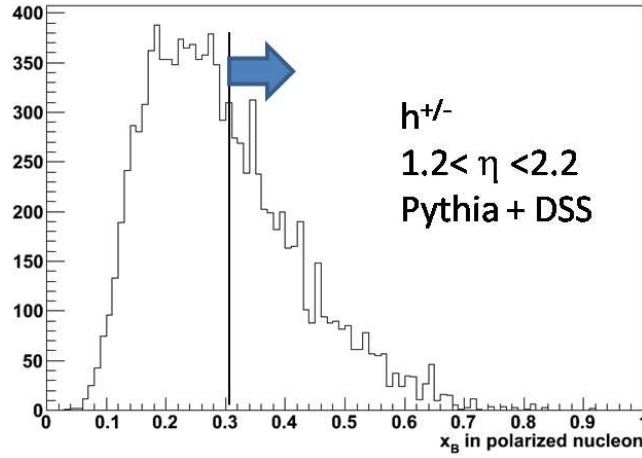
Figure 1.17: Dummy. Bjorken-x distribution in polarized proton for PYTHIA events with a hadron scattered into $1.2 < eta < 2.2$ for $x_F > 0$. A substantial fraction of the data is at $x_B > 0.3$, where the DIS data ends.

The most critical experimental performance parameters for these type of MPC-EX measurements would include the angular resolution for the direction of the jet axis and the resolution in the hadron momentum fraction z. Uncertainties in knowing the jet axis will dilute the amplitude of the azimuthal Collins asymmetry and uncertainties in measuring hadron's energy fraction ($z = E_h/E_{jet}$) will smear the spin analyzing power of the Collins F.F. in the stage of data interpretation. The latter of these two is critical, given that the Collins F.F. has a strong z-dependence, see Fig. 1.12.

1.2.2   Other possible SSA measurements with MPC-EX

In addition, not elaborating on the details, we list here other possible SSA measurements with MPC-EX:

1. Direct photon SSA (A_N^γ), which is purely originated from Sivers effect.

2. SSA of back-to-back di-hadrons and back-to-back di-jets.

3. SSA of back-to-back γ-jet [17] and back-to-back photon-pairs.
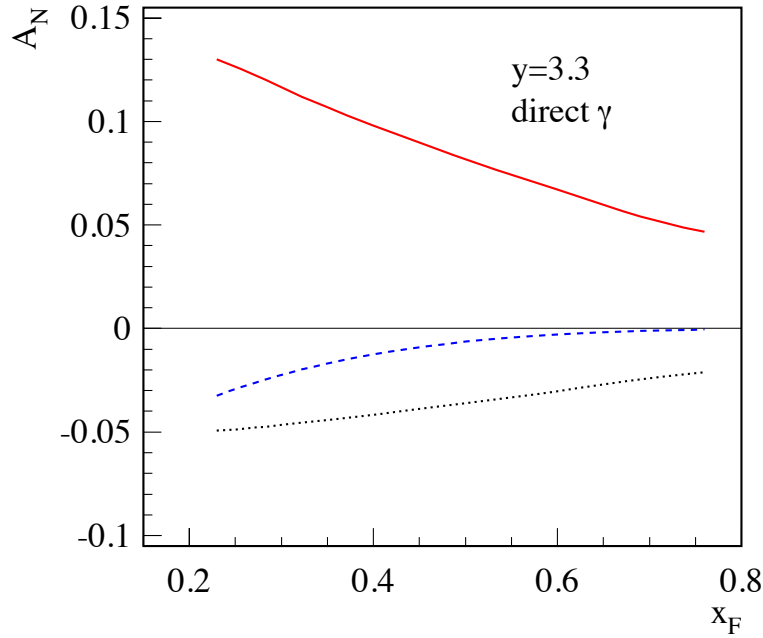
4. SSA of very forward J/ψ productions.

Figure 1.18: The SSAs for direct photon production A_N^γ in $p^\uparrow p$ collisions [?] at $\sqrt{S} = 200$ GeV, as functions of x_F for rapidity $y = 3.3$. Curves are the same as in Fig. 1.16.

1.2.3   Summary: MPC-EX and the Study of Nucleon's Transverse Spin Structure

The goal of nucleon spin structure studies is to answer the question: how the nucleon spin is composed of the spin and orbital angular momenta of the quarks and gluons inside the nucleon ? With MPC-EX we will address the following fundamental questions regarding the nucleon's intrinsic spin structure and the color-interactions that hold together the nucleon's building blocks:

1. How much is quark's spin aligned with nucleon spin in the transverse direction ?

2. What is the role of quark's transverse spin (transversity) in during fragmentation ?

3. What is the role of parton's transverse motion and its correlation with nucleon spin ?

4. What is the role of the color-interactions between a hard-scattering parton and the remnant of the nucleon ?

Specifically, with the new experimental capabilities provided by the MPC-EX, we will make precision measurements that provide clear answers to the following questions:

When a transversely polarized proton produces a very forward jet in a high energy $p + p$ collision, relative to the direction of proton's spin,

- **would a π^0 particle favor the left side or the right side within the jet ?**

- **would the jet itself favor the left side or the right side of the collision ?**

Chapter 2

The MPC-EX Preshower Detector

2.1   The MPC-EX Detector

The MPC-EX detector system includes existing Muon Piston Calorimeters and proposed Extensions which are two nearly identical W-Si preshower segments, located upstream of the north and south muon piston calorimeters respectively. The pair preshower-MPC shares the real estate inside Muon Pistone pit, their functionality is largely complementary. The preshower will

- improve quality of measurements of electromagnetic showers in the MPC aperture by reducing longitudinal leakage of energy;

- improve discrimination between electromagnetic and hadronic showers;

- reconstruct π^0's via effective mass measurements and shower shape analysis to the p_T extent allowed by the calorimeter acceptance and RHIC luminosity;

- measure shower impact vectors with resolution sufficient for efficient matching to charged tracks reconstructed by the FVTX;

- measure jet 3-vectors with precision sufficient to reconstruct kinematics of inverse Compton scattering resulting in γ-jet events with jets or direct photons in the forward direction;

- assist in measuring energies inside jet cone around high-p_T lepton candidates for isolation testing.

MPC's were installed in 2006 and already produced a wealth of physics results. It is to further extend the physics reach of the PHENIX forward spectrometers that we designed extensions (preshower) to existing MPC's which are by itself are highly segmented total

absorption detectors of $\sim 18X_0$ depth. The preshower converts photons, track and measure energies deposited in Si layers by photons and charged particles, count and classify (electromagnetic/hadronic) hits, measure hit-to-hit separations and reconstract hit pair effective masses further used to extract π^0 yields. It allows for direct photon extraction be done in a self-consistent way without using extrapolated data with often unknown systematics for background subtraction.

The MPC-EX's are located ~ 210 *cm* from the nominal collision point north and south of the PHENIX central magnet. The MPC alone is capable of resolving close hits with similar energies down to the separation of the order of 3 cm effectively limiting π^0 reconstruction range to momenta below 15 GeV/c. To extend that range towards π^0 luminosity limit in the forward direction ($\sim 100 GeV$) the preshower is designed as a sampling structure of tungsten and active pixilated silicon layers with readout integrated with silicon in the form of micromodules. Silicon provides for versatility of segmentation; tungsten has a small Moliere radius (9.3 mm) so the showers in the preshower are very compact. Tungsten also has an excellent ratio of radiation and absorption lengths ratio well matching that of PbWO4 (MPC crystals) which is important for electromagnetic energy measurements in the presence of heavy hadronic background. The preshower is built of eight sampling layers each consisting of 2mm thick W plate and 3 mm deep readout. The total depth of preshower ($\sim 4X_0$) is chosen to allow both photons from π^0 to convert and be reliably measured in at least two X and two Y sampling layers.

The granularity of the preshower is chosen to match the expected two photon separation in π^0 decays. The 100 GeV/c π^0 produced at a nominal collision point will generate two hits in preshower separated by 1 cm (compare to Moliere radius of the detector equal to $\sim 2cm$). To match both towers in MPC and minimal two photon separation pixels on the silicon have rectangular shape and a size of $1.8 \times 15 mm^2$. Each pixel signal is split with a ratio of 1:30 with individual copies sent to two independent SVX4 chips.

The ideal location for preshower would be flash with the front face of crystals in MPC. It is precluded by earlier decision to locate MPC readout (APD's and signal drivers) upstream of crystals. The actual preshower location on the beam line is also constrained by concerns about background to muon tracking station 1 from inside of the pit and will be decided upon completion of integration study of utilities and cable routing which is currently being pursued for the MPC-EX upgrade.

Figure 2.1 shows a three dimensional model of the MPC-EX system installed into the pit on the muon piston. Both components of the system do calorimetry style measurements of the energy deposited by charged and neutral particles inside its active volume (crystals in case of MPC and Si in case of preshower) so the total sampling depth of the two detectors (4 X_0 in MPC-EX and 18 X_0 in MPC) will now contribute to energy measurements.

The pit has radius of $20cm$ and depth of $\sim 30cm$. Its opening upfront of MPC is heavily used by sparsely installed MPC signal and power cables (see Fig. **??**), cooling lines for MPC and fixtures supporting beam pipe. There is a conflict between preshower and MPC monitoring system (distribution boxes). The conflict will be resolved redesigning MPC
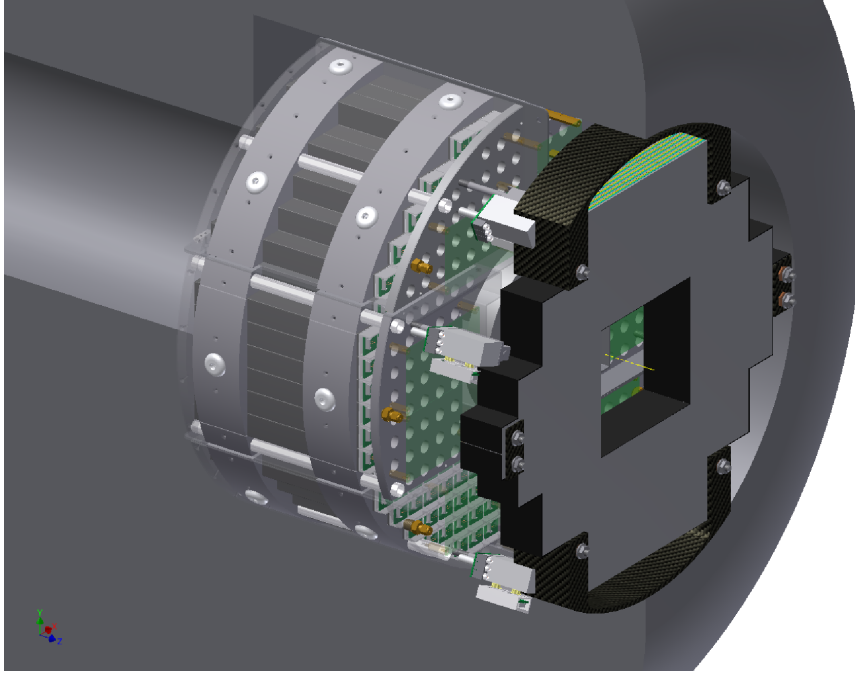
Figure 2.1: 3D rendering of Muon Piston Pit with MPC-EX fully installed.

distribution boxes to illuminate fibers with back-scattered light.

Details of the MPC design could be found in [**?**] Mechanical design of preshower and its readout are described below.

2.2   Mechanical Design

The decision which strongly affected the design of preshower was to replace complemetary ganged pad readout (pad size approximately matching crystals of MPC) originally planned for tower-kind energy measurements by towers "configured on the go": digital sums of the energies measured in the pixels contributing to region of interest around vector pointing from collision point to the shower found and measured in MPC. The $1.8 \times 15 \; mm^2$ pixels in preshower add into $15 \times 15 \; mm^2$ towers with X and Y pixels allowed to combine into correlated (partially overlapping) geometrically pointing (separately in X/Y planes) sets of towers. Thus defined towers are MPC shower position dependent and so could be different for different even closely spaced showers. Their size can be varied depending on shower width greatly improving the quality of energy sharing between individual objects. Configured towers are pointing and have energies, positions, hit counts and object width measured in every sampling layer so both particle identification and particle tracking are simplified and improved. The 15 mm length of the pixel makes its energy measurements robust against adverse effects of the occupancy (each layer has ~ 2500 pixels compared to ~ 200 crystals in MPC) so we expect decay asymmetries measurements further improved compared to original FOCAL proposal. The advantages of this "configure on the go" approach will be especially important for the forward jet measurements which in case of MPC-EX system will use both jet definitions based on hit counting in preshower and total electromagnetic energy measurements associated with those hits in a hybrid MPC-EX/MPC calorimeter.

The radial dimensions and geometry of preshower were chosen to fit within the envelope defined by the muon piston front face (see Fig. **??**) and reorganized signal cables of MPC (last feet of cable length is unjacketed, cables restrained on the pit wall close to diver boards) and to provide the best match to MPC acceptance resulting in a configuration approximating the circle (actual shape of W absorbers is defined by 62x62 mm^2 footprint of individual Si micromodule) with a central opening of 124x150 mm2 to accomodate beam pipe flanges and beam pipe support.

The preshower is built of 2mm W plates interleaved with readout layers (to allow for micromodule installation the readout layer depth is set to 3.0 mm). 0.5 mm thick G10 carrier boards are glued to W plates by conductive tape creating nearly perfect Faraday cage for silicon sensors embedded into micromodules pluggable into carrier board. In designing micromodules we decided on a very unconventional untested decision. Sensors are laminated in between 0.4 mm ceramic tile and 0.4 mm thick sensor readout card (SRC) carrying dual RC network used to split the signals and AC decouple silicon diods from SVX4 input circuitry. SRC carries two SVX4 chips which combine both analog amplifiers and storage and digitizers and carry two separate grounds (analog and digital). The unconventional part of this design is a presence of digital signals on the traces immediately above the silicon sensors so we went to the extreme to minimize the pickup of digital activity signals on Si. Fortunately calorimetry is forgiving of the additional material in readout layers and a good ground layer between sensor and first layer with traces was
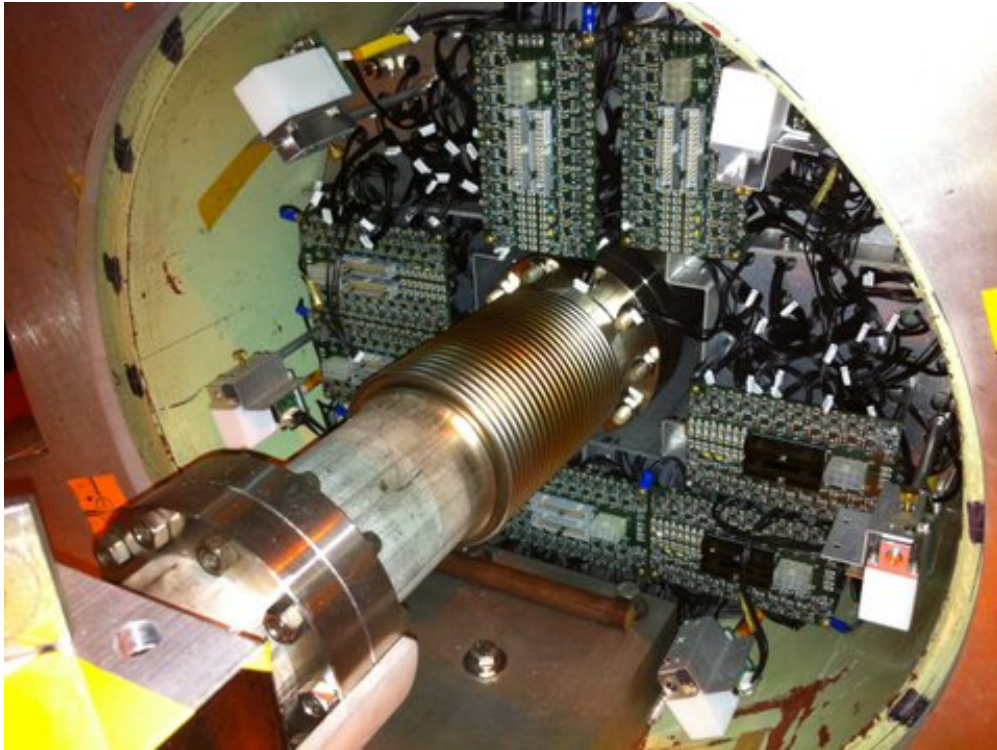
Figure 2.2: A beam view of the North Muon Piston with MPC installed. Signal cables removed.

sufficient to keep noise level related to digital activity on the board well within SVX4 pedestal width.

We have chosen FNAL developed SVX4 128 channels pipelined cheaps as a base for readout system.

A number of ongoing R&D projects aimed at building similar calorimeters for experiments at a future electron-positron linear collider are considering the option to digitize signals from every pixel in all sampling layers. The proposed solutions are all in their preliminary stages, have number of constrains (range, power etc) and expensive. We believe that we found a unique if not perfect solution to this problem based upon einexpensive and commersially available components which is equally applicable to calorimetry in all kinds of collider experiments. The MPC-EX preshower is the first ever built calorimetry detector with plaggable silicon micromodules and full on detector digital conversion of the analog signals generated by particles passing layers of silicon detectors, .

Main design parameters of the MPC-EX preshower are in the table **??** below. Details of the readout in the Section to follow.

Table 2.1: MPC-EX Preshower design features. All counts are for a single unit.

Parameter	Value	Comment
Distance from collision vertex	220 cm	
Radial coverage	$\sim 18cm$	
Geometrical depth	~ 5 cm	
Absorber	W (2mm plates)	0.5 X_0 or 2% L_{abs}
Readout	Si pixels (1.8x15 mm^2)	
Sensors	$62 \times 62 mm^2$	192 ($1.8 \times 15 mm^2$ minipixels)
Pixel count	24576	
SVX4's	384	

2.3   Electronics and Readout

The MPC-EX detector system is composed of eight identical readout planes arranged around the beam pipe in front of the MPC detector. The enclosure diameter is 44 cm. Each plane consist of two identical carrier boards, attached to the tungsten absorber plates. Each carrier board contains 12 plug-in modules with silicon sensors and readout ASICs. The technology for the sensors will be p-on-n detectors with narrow mini-pads 15.0 x1.8mm. The sensors will be orhthogonally oriented in alternate layers. The maximum occupancy at the mini-pads is ?? in Au+Au events. To provide high dynamic range, the signal from each mini-pad is split with ratio 30:1 using capacitive divider and it is send to different ASICs.

Unit Counts per arm:

number of readout planes	8
number of minipad modules	192
number of minipads	24576
number of readout chips	384
number of carrier boards	16
number of FEMs	8
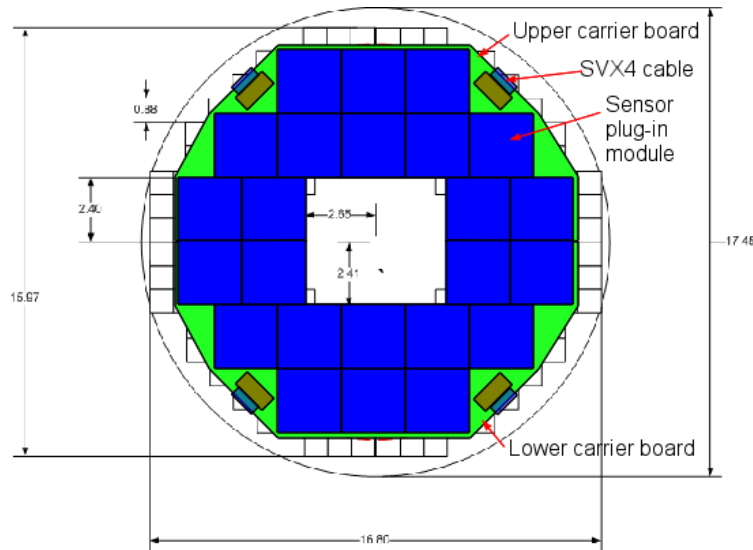
Figure 2.3: Location of the MPC-EX readout electronics in front of the MPC (Dimensions in inches).

The data from the readout ASICs will go to PHENIX DCMs through FEM boards as indicated on Fig. 2.4. The FEM will reside on the outer shell of the muon piston magnet and it will perform the functions of: converting the continuous stream of commands from the control optical fiber into the SVX4 control signals, collecting the data of several SVX4 chains, serializing it and sending it out on data optical fiber to the PHENIX DCMs.

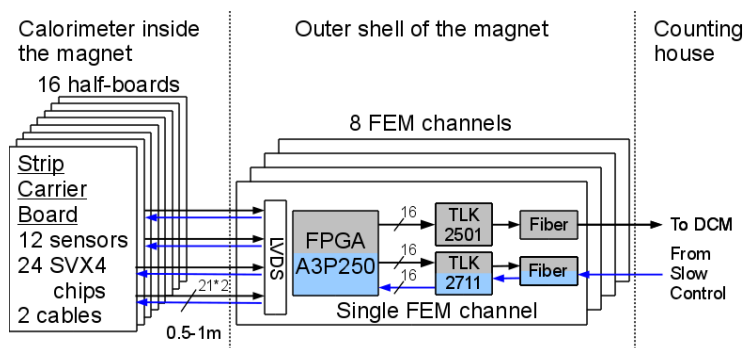**Figure 2.4:** Block diagram of the MPC-EX readout electronic s components. The blue area - front-end clock domain, the grey area - back-end clock domain.

2.3.1   Strip Readout Module

The design goal of the readout plane is to keep it is as thin as possible to minimize the transversal expansion of the particle shower in the absorber-free areas. The sensor plane consist of two carrier boards (upper and lower) which are conductively attached to the tungsten absorber plates. The carrier board is thin PCB, which has low-profile (0.9mm thick) connectors where the minipad modules will be plugged in.

The readout card is mounted on top (p+ side) of the sensor, it is wire bonded to to the sensor pads at the edge of the sensor using 25u Al wires. The positive bias voltage is applied to the backside (n- side) of the sensor using flexible leaf of gold-plated fabric. A thin (0.4mm) ceramic cover is attached to the backside of the sensor, it provides mechanical rigidity to the assembly.

Figure 2.5: Stack-up of the minipad module.
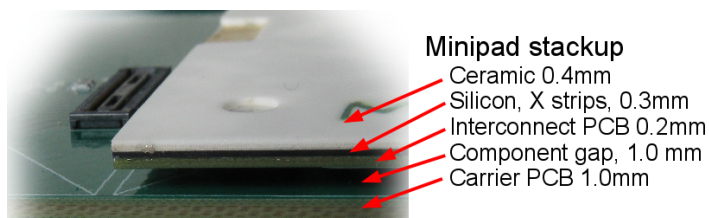
The signals from each of the minipads are routed to two SVX4 ASICs through different decoupling capacitors. The high-gain leg SVX4 will be optimized for measuring MIP signals, the low-gain leg SVX4 - for large signals. The ratio between two legs is 30:1, it is chosen so to ensure that the maximal signal in the high-gain leg will, at the same time, be detectable in the low-gain leg.
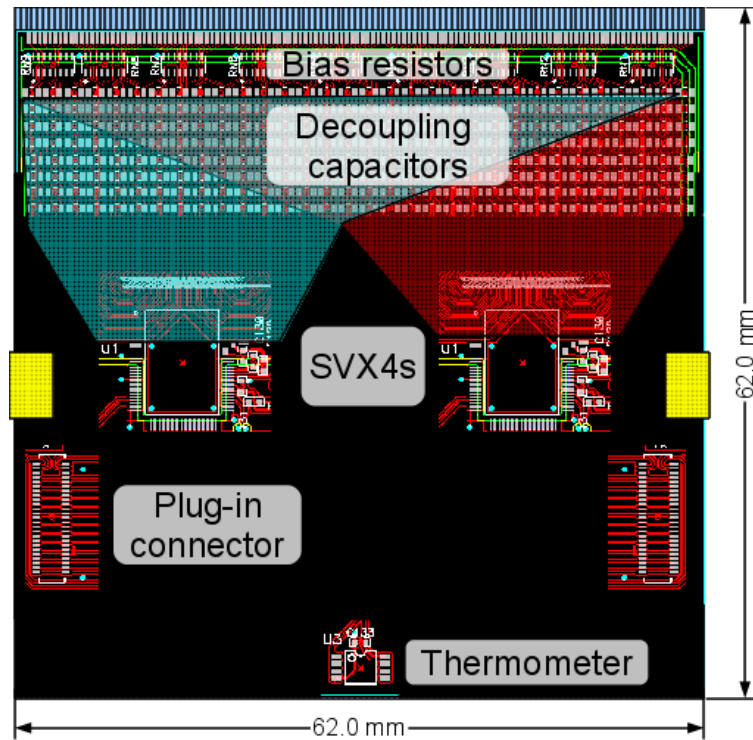
Figure 2.6: Placement of components of the readout card.

Each carrier board provides two readout chains with 6 modules per chain. Each chain is connected to FEM using off-the-shelf low profile flex cable assemblies (JF04 from JAE). All signals in the cable are LVDS, the carrier board have receivers to convert SVX4 control signals from LVDS to LVCMOS levels. The total thickness of the readout gap is 3.0 mm. The technological gap between sensors is 0.5mm. The prototype of the carrier board (Fig. 2.7) has been designed and tested succesfully.

Figure 2.7: Prototype of the carrier board with 4 installed minipad modules.

2.3.2   Dual SVX4 Readout

The dual SVX4 readout have been simulated using LTSpice, the schematics is shown on the figure below.

Figure 2.8: SPICE model of the strip readout channel.

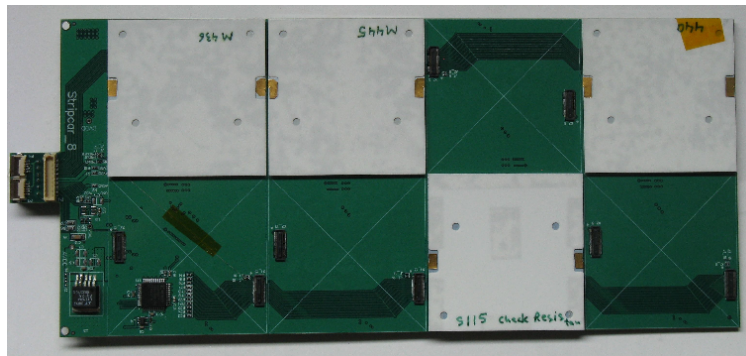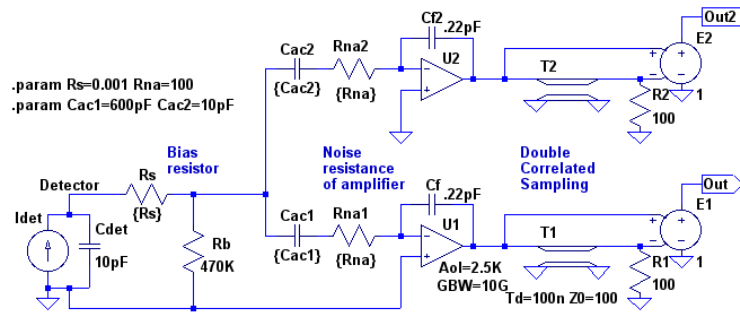The sensor strip is presented as a current source with realistic strip capacitance of 10 pF, the bias resistance is the highest available in small package. The open gain loop (Aol) of the amplifier is from the specs of the SVX4. The unity gain bandwidth (GBW) was selected to match the published rise time of the SVX4 with fastest setting. The effective series resistance (Rna) was estimated by matching its contribution to the published ENC vs. Cdet dependence. The shaping in the SVX4 is done using double correlating sampling technique, this is simulated using ideal transmission line and a subtractor.

If we assume the infinite open loop gain (Aol) of the operational amplifiers, then the gain of legs Out and Out2 are

*G1 = 1/Cf * Cac1/(Cdet+Cac1+Cac2), G2 = 1/Cf * Cac2/(Cdet+Cac1+Cac2).*

It can be shown that the S/N at Out is proportional to 1/Cdet and it does not depend on its decoupling capacitor Cac1.

SN1 ∼ 1/(Cdet+Cac2), similarly, SN2 ∼ 1/(Cdet+Cac1).

To have the SN1 small, we need to choose the Cac2 as small as possible, but controllable, the reasonable choice is 10 pF. If we select the gain of the low leg G2 = 1/30 of G1 then the Cac1 should be 300 pF. The SN1 will be 1/2 of the SN0 (S/N of the isolated channel), SN2 = 1/30*SN0.

The simulation, which includes the finite Aol and GBW shows that the G1/G2 = 30 is achieved when Cac2 = 10pF and Cac1 = 600pF. The results of the simulation are shown on Fig. 2.9 and 2.10.
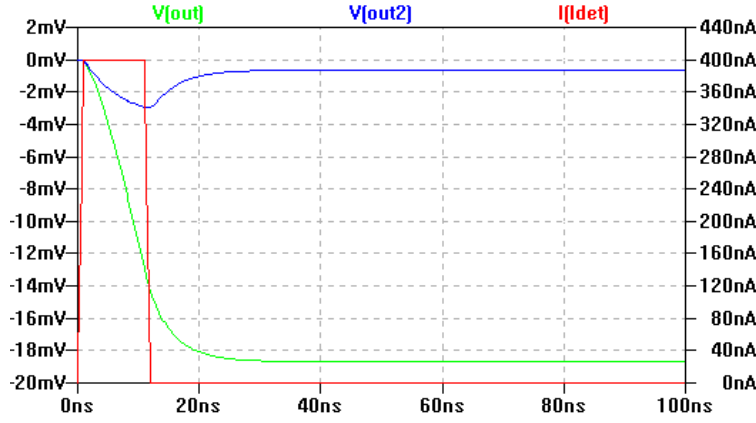
Figure 2.9: Response to 1 MIP (4.4 fC) charge injection.
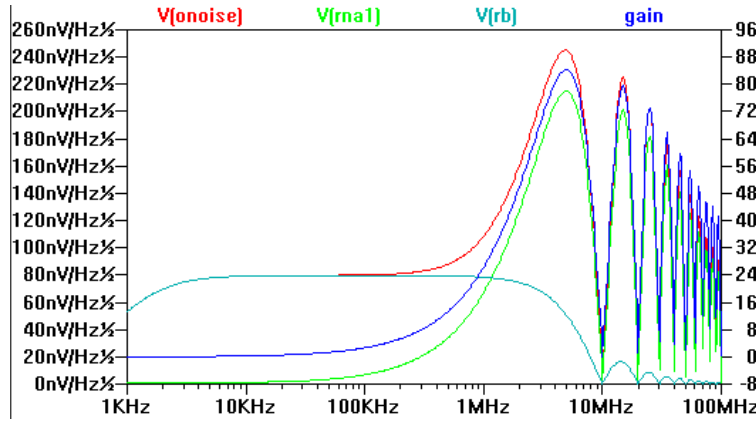
Figure 2.10: Noise analysis.

The signal amplitude of the high-gain leg is 18.68 mV, of the low-gain leg it is 0.64 mV. The main noise contribution above 1 MHz comes from the preamplifier, below 1 MHz - from the bias resistor.

For high-gain leg the total RMS noise at Out is 1.17 mV, this corresponds to ENC of 0.28 fC or 1730 electrons. The contribution from Rna1 is 1.04 mV, from Rb is 0.17 mV. If serial resistance of input traces (Rs) is 40 Ohm, then the total RMS noise is 1.21 mV. **We can conclude that the noise contributions from the bias resistor and from the input traces are not significant.**

For low-gain leg the total RMS noise at Out2 is 0.76 mV, ENC = 5.2 fC or 32600 e, this is slightly larger than 1 MIP but still less than one ADC count.

The saturation level of the pipeline cell of the SVX4 is $\sim$ 100 fC, the saturation level of its preamp is at $\sim$ 200 fC.

With charge division of 1/30 between two legs we can achieve: in high-gain leg: S/N = 16 for 1 MIP and saturation at 22 MIP or 1.8 MeV deposited energy. in low-gain leg: saturation at 660 MIP or 32 MeV of deposited energy.

Important feature of this design is that the gains of both legs depends very weakly on the varying detector capacitance.

2.3.3   FEM

The FEM drives up to eight SVX4 chains and serializes them through one fiber link to the PHENIX DCM. The data from SVX4 arrive non zero-suppressed, although the on-chip real-time-pedestal subtraction could be switched on. For each trigger every SVX4 generates 129 of 2-byte words. The FPGA in the FEM strips off the channel number byte, selects for output either low-gain or high-gain value from two SVX4 and streams the result to the serializer. The input stream of 8 of 16-bit data words @40 MHz is reduced by factor of 4 and the resulting stream is serialized with nominal DCM data rate of 1600 Mbps. The leg bits, representing which of the legs was selected for output, are embedded into the output sreams (2 bytes of leg bits after 16 ADC bytes).

There are two clock domains in the system as shown on Fig. 2.11: front-end clock and back-end clock. The front-end clock, synchronous with the beam crossing, is provided by PHENIX GTM and it is trasferred to FEM through the optical link from the Serial Control module. The back-end clock is local to FEM it synchronizes the data transfer to DCM.

The readout is dead-time free and fully pipelined, the SVX4 can store up to four samples in its input FIFO. The data are ready to be send to DCM in 5.0 microseconds (digitization time) after the trigger.

Readout of one SVX4 with 40 MHz readout clock will take approximately 3.4 us. The chain of 12 SVX4s can be transferred to the FEM in 45 microseconds.
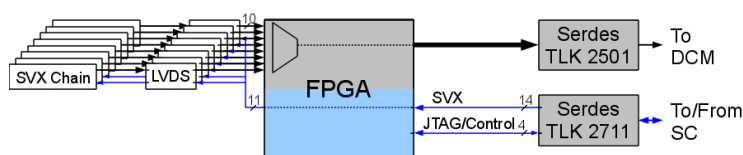
Figure 2.11: Block diagram of FEM board.

The FEM has very transparent architecture, divided in two, practicaly independent partitions, corresponding to the clock domains - front-end (blue) and back-end (grey). The back-end partition streams out to the data fiber link whatewer it receives from the SVX4 chains. The front-end partition simply transfers the SVX4 signals from the Serial Control fiber link to SVX4 chains.

FEM de-serilizes the 16-bit commands coming with the rate of 80 MHz from that link,

Table 2.2: Serial Control bit assignment.

Bit	In	Out
1	In[0]	ADDR_CS[0]
2	In[1]	ADDR_CS[1]
3	In[2]	ADDR_CS[2]
4	In[3]	ADDR_CS[3]
5	In[4]	CTRL_Cmd[0]
6	In[5]	CTRL_Cmd[1]
7	In[6]	CTRL_Cmd[2]
8	In[7]	SVX_FEClk
9	In[8]	SVX_Trig[0]
10	In[9]	SVX_Trig[1]
11	In[10]	SVX_Mode[0]
12	In[11]	SVX_Mode[1]
13	In[12]	SVX_Readout
14	In[13]	JTAG_TMS
15	In[14]	JTAG_TCK
16	JTAG_TDO	JTAG_TDI

Table 2.3: Trigger[1:0] encoding

Code	Action	SVX signals
0	no action	
1	Trigger	L1A
2	Abort gap	PARst,PRD2
3	Calibration	CalSR

synchronously with the beam clock. The allocation of parellel bits is shown on table 2.2.

Four bits of the command word (ADDR*) are used to address the FEMs. Three bits (CTRL*) are reserved for FPGA control: initialisation and reset of the beam clock counters are encoded here. Six bits of the command word (SVX*) are translated directly into the signals on SVX chain according to tables 2.3 and 2.4.

Three bits of the command word and one bit from the serdes receiver (JTAG*) constitute the JTAG interface. The main purpose of the JTAG interface is the programmatic control of the FPGA in real time, this is implemented using UJTAG macro in the FPGA. The JTAG is also used to re-configure the FPGA firmware. The serdes for Serial Control connection is small-footprint TLK2711 working at 1.6 Gbps, the serdes for DCM connection is TLK2501.

The power consumption required for one arm is approximately 110 Watts for 16 carrier boards and 20 Watts for 4 FEMs. The details are shown below.

Table 2.4: Mode[1:0] encoding

Code	Action	SVX signals
0	Configuration	FEMode=0
1	Reserved	
2	Acquire	FEMode=1, BEMode=0
3	Acquire&Digitization	FEMode=1, BEMode=1

Board	Line	Voltage	Current	Wattage
Carrier Board	AVDD SVX4	2.5V	2.0A	5W
	DVDD SVX4	2.5V	0.5A	1.3W
	DVDD LVDS	2.5V	0.2A	0.5W
Total				6.75W
FEM	DVDD LVDS	2.5V	1.0A	3.8W
	FPGA Core	1.5V	0.6A	0.9W
	FPGA IO	2.5V	0.2A	0.4W
Total				5.1W

The JF04 cable assembly between the FEM and the carrier board carries 21 LVDS pairs and it has ground plane and 9 extra lines, which can be used to provide power to the carrier board. The powering of the carrier boards from the FEMs through the signal cable simplifies the cable routing in the tight area of the muon piston magnet but it may have impact on the noise figure of the system and should be tested before the final installation in place.

The current FEM channel design, serving 4 of SVX4 chains has been succesfully implemented on a Virtex-II XILINX FPGA. The full design for 8 chains will be implemented using more radiation hard A3P1000 ACTEL FPGA.

2.3.4 Serial Control

The Serial Control module:

distributes the front-end clock from PHENIX GTM to FEMs,
generates trigger and SVX4 control signals from mode bits of the PHENIX GTM,
provides run control of the FEMs,
provides configuration of the SVX4 chains,
provides configuration for FPGA in FEMs,
monitors the status of the FEMs

All this information is sent to and from FEMs through the optical fibers. The Serial Control FPGA contains several serial transceivers, one transceiver is used to emulate fixed-latency GLINK protocol of the GTM, the rest are used to connect to FEMs. Communication with external world over ethernet is provided by micro-processor unit Digi ConnectMe 9210

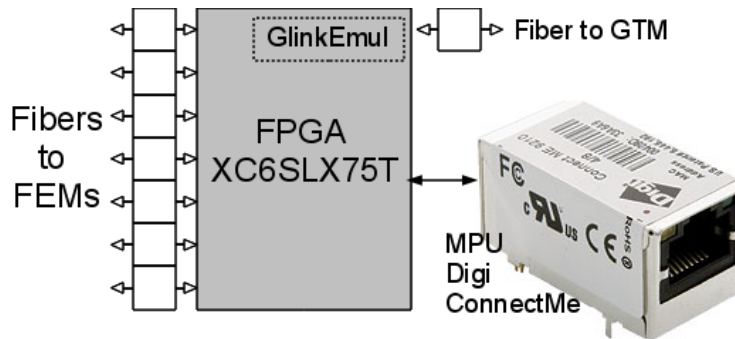from Digi International, which is embedded into the modular ethernet jack.

Figure 2.12: Block diagram of the Serial Control module.

The communication protocol between MPU and FPGA as well as graphical user interface to the Serial Control have been developed and tested on the FEM prototype.

2.3.5 Radiation Environment and Component Selection

The evaluation of the FPGA technology available for use on the MPC-EX FEM primaly consider the effects of the radiation on the performance of the overall system. Additional consideration include I/O configuration, serial communication capabilities and reconfiguratio of the device within the system. The choice of technology is primarily the choise of configuration memory technology as logic implementation and density do not really impact our application. The different configuration technologies and their suppliers under consideration are as follows:

SRAM	Altera, Xilinx
FLASH	Actel ProASIC3
Anti-fuse	Actel Axcelerator

The primary concern for MPC-EX about FPGAs is the ability to operate in a radiation environment. Considerable effort and investigation has gone into this question by such organizations as NASA, DOD and CERN. The concern here is to determine the radiation environment and its effects on FPGA performance for the MPC-EX system. The radiation environment for the MPC-EX is the environment of the PHENIX interaction area with either RHIC I or RHIC II luminosities. The master's thesis *"A scalable analytic model for single event upsets in radiation-hardened field programmable gate arrays in the PHENIX interaction region"* by Steven Skutnik provided invaluable information on defining these environments. The total integrated dose that the MPC-EX detector is expected to see is on the scale of 20?? kRad/yr over 10 years, though the absolute value depends on the radial position of the components.

Based on the above, the upset rates in the PHENIX radiation environment at 10 and 40 cm are as follows:

RHIC I AuAu

 10??cm   1.6x10-6?? /bit/hr
 40??cm   1.0x10-7?? /bit/hr

RHIC II AuAu

 10??cm   1.6x10-5?? /bit/hr
 40??cm   1.0x10-6?? /bit/hr

RHIC II p+p

 10??cm   1.28x10-4?? /bit/hr
 40??cm   8.0x10-5?? /bit/hr

The primary elements of the FPGA that are affected by the radiation are the SRAM memory elements, clocks and sequential logic. The primary concern with Altera and Xilinx FPGAs is that the configuration or functionality of the device is contained in SRAM and upsets in this memory affect the function of the device and will cause it to no longer perform the function as it was initially programmed. Both Xilinx and Altera offer configuration 'scrubbing' solutions that check the configuration but they require a reload of the configuration if an error is detected, which takes time. The configuration SRAM size dominates the FPGA SEU rates as it is 3 to 10 times the size of the data SRAM available. The configuration and data memory sizes for a mid- range Statix II GX part and a high-end Cyclone II part are shown below:

 Altera EP2SGX60   Configuration SRAM = 16,951,824   Data SRAM = 6,747,840
 Altera EP2C70   Configuration SRAM = 14,319,216   Data SRAM = 1,152,000

The SEU rates for the SRAM based FPGAs must include both configuration and data memories. The Altera and Xilinx devices are extremely similar in regards to their radiation susceptibility so we use just the Altera device as an example here. In consideration of the application in the FPGA for MPC-EX, data memory upsets are ignored and triple redundancy methods would be used on sequential logic to reduce upsets to negligible levels. Therefore, considering only configuration SRAM upsets, the upset rate for the Altera chips are as follows:

 EP2SGX60   27.12 upsets/hr   RHIC I AuAu   10cm
 EP2C70   22.91 upsets/hr   RHIC I AuAu   10cm
 EP2SGX60   271.2 upsets/hr   RHIC II AuAu   10cm
 EP2C70   229.1 upsets/hr   RHIC II AuAu   10cm
 EP2SGX60   2170 upsets/hr   RHIC II p+p   10cm
 EP2C70   1833 upsets/hr   RHIC II p+p   10cm

These upset rates are per device so the system upset rate is determined by multiplying these rates by the number of devices in the system. Even with configuration scrubbing the SRAM FPGAs have an unacceptable down time because the configuration reload time is

between 1 and 2 seconds. The Actel FPGAs do not have SRAM configuration memory so they are immune to this form of upset. FLASH memories exhibit dissipation of the charge on the floating gate after 20kRad of integrated dose. The dissipation is not permanent damage and is remediated by reprogramming the device. Flash memories also displayed SEE problems during programming during radiation exposure that included gate punch-through, a destructive effect. These types of SEEs are avoided by not programming the FLASH under radiation exposure conditions, namely during machine operation. The Actel FPGAs have a decided advantage over the SRAM based FPGAs since they do not have configuration upsets. The additional factors to consider for the selection of the FPGA are I/O configurations, serial communication capabilities and reconfigurability in the system.

Chapter 3

Simulations and Physics Observables

This is where the simulations results will go.

3.1   Reconstruction of electromagnetic showers.

3.1.1   Overview of Section

The method used for reconstructing electromagnetic showers in the MPC-EX is detailed in this section. The detector, as described previously, uses eight layers of silicon strips to determine a track vector and it's energy from localized clusters of hits. The overall aim of this section is to describe how the clusters are formed, how the energy of the preshower is determined. Also, we discuss how the preshower is connected to the existing MPC clusters and how the found track vector from the silicon can be used to find sub-tracks related to two very closely showering tracks (like those expected in π^0 decays). This does not detail the cluster-finding algorithms employed in the MPC itself, only for the preshower.

3.1.2   Preshower Cluster Reconstruction

The methodology used for the cluster-finding in the preshower is quite simple. First, the energy of each layer for a certain tower is summed to form the total energy deposited in towers of minipads. Next, a search for all possible peaks of energy is performed using the energy in the minipad towers, see Fig. 3.1 for a cartoon of this. The whole detector is scanned (successively for the whole detector) to find an energy peak in a localized region. of eight minipads. The tower with the peak energy within that region is considered a preshower track candidate. Only one peak is allowed at this stage. This peak is added to the list of preshower track candidates.

For each preshower track candidate, the track energy and energy-weighted track-vector is calculated as the sum of energy deposited in a 16 strips wide region. This yields an average position over many minipads, rather than the position of the highest-energy hit. A new energy (summed over the central and surrounding towers) and an improved energy-weighted track-vector is recalculated for added precision.

Once the preshower tracks are determined, their directional properties are converted into "Hough" parameters for ease of matching. In Hough tracking, the coordinates of the track are converted into "Hough" parameters. For the case of neutral particles, or those which do not deviate from a straight line trajectory, the Hough parameters are the slope (x/z or y/z) and intercept. This is far more conventient to use as these parameters are the same for each layer of silicon in the preshower *and* the same for the MPC itself. By contrast, tracking or track matching with cartesian coordinates would be more difficult as the x and y positions change with the z position of the layer. When many points of reference are available, localized slopes and intercepts between each pair can be created allowing both the slope and intercept to be used for matching. In our case, the number of layers is small, so the Hough parameters are formed using the intercept (vertex position) and each point. Thus, only the slope parameter is used in the track finding/track matching.
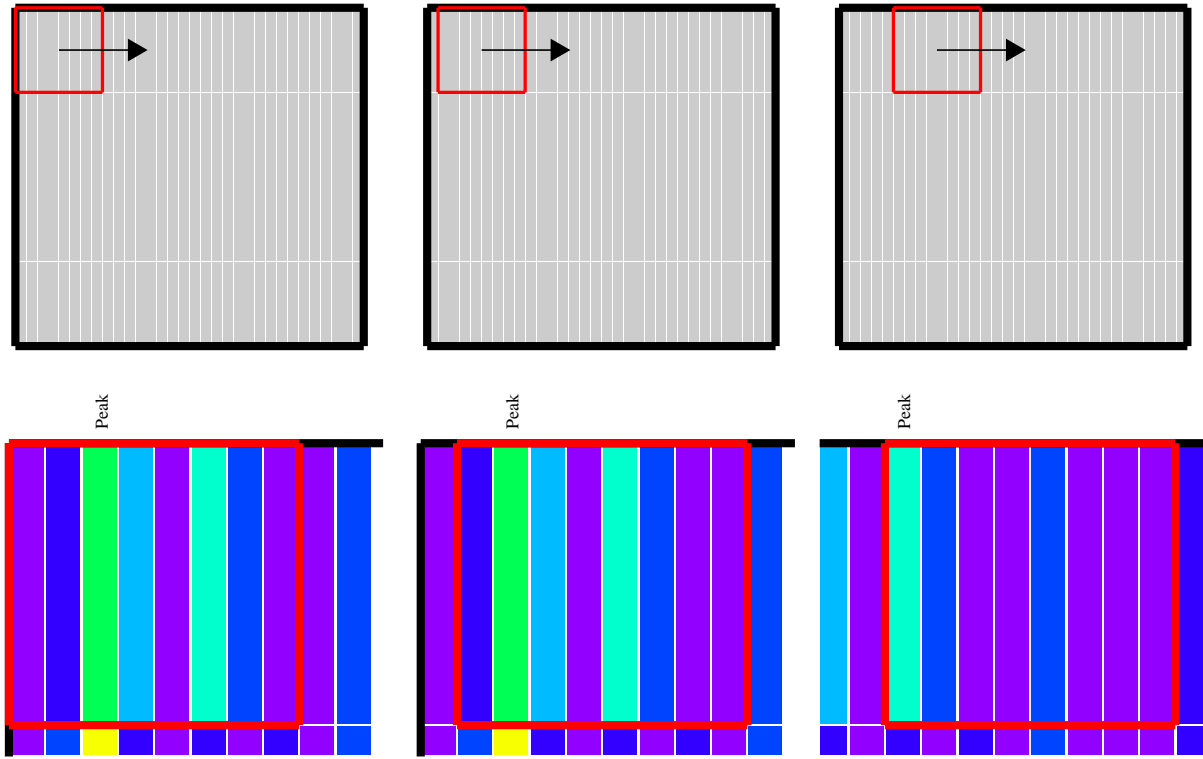
Figure 3.1: Cartoon showing the reconstruction procedure. The upper panels depict the full sensor, the lower are zoomed in on the region in question for that particular step. The colors in the lower panel show the energy recorded in a particular minipad. The leftmost column shows the starting point of the reconstruction, the center shows the next step, i.e. moved over one minipad. The rightmost column shows a few steps later. The red outline shows the current search window. A single peak is found in each window corresponding to the highest energy deposited in a single minipad.

3.1.3   MPC Cluster Pointing Resolution

The MPC has an intrinsic limitation in it's pointing resolution. Figure 3.3 shows the η (left panel) and ϕ (right) resolution for MPC Clusters, versus the input energy of the particle. A resolution of $\Delta\phi(\eta)<0.04$ is observed for high momentum track (i.e. $E_{Input}>30\,\text{GeV}$). Tracks at lower momenta have a worse resolution owing to the diminished energy available for showering and (for π^0s) the deflection of daughter γs from the original direction.

In terms of the resolution in Hough space, Fig. 3.4 shows different prospective Hough slope differences between the MPC and the pre-shower (representing a possible quality control cut (see below)). The resolution of the MPC is high enough such that a very tight cut on this parameter can be used, reducing possible contamination from additional particles.
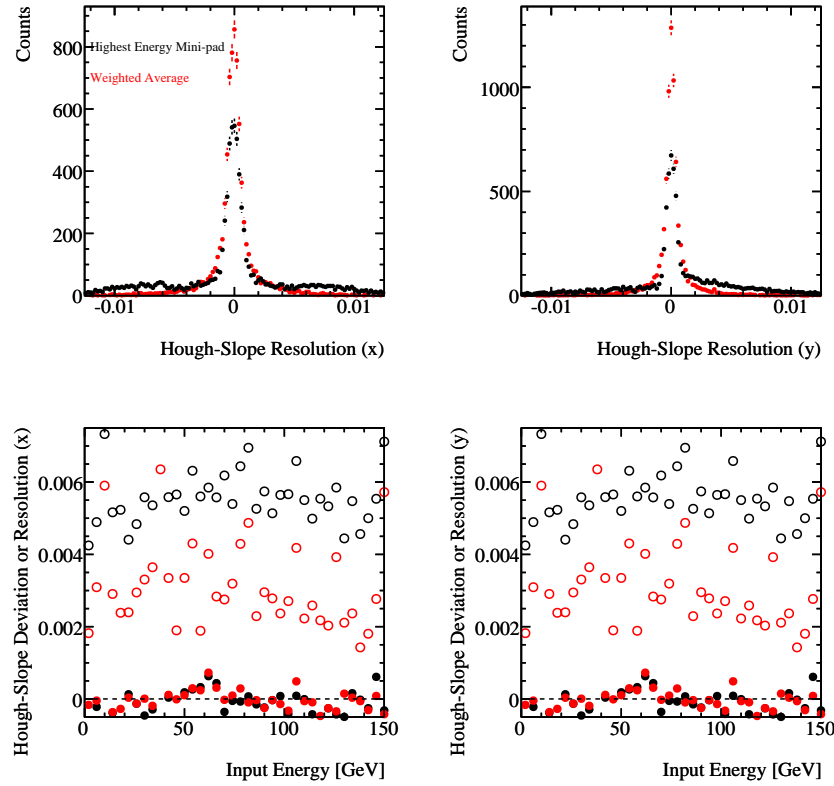
Figure 3.2: Comparison between the resolution determined from the highest energy minipad (trial peak position - black symbols) and that from the energy-weighted average (red) for single input γs. The top panels show the the difference between the reconstructed and input Hough slope for the x- and y-directions, left and right figures respectively. The lower panels show the mean deviation (solid symbols) and resolution (open) as a function of input energy.

3.1.4 Track Matching

The cluster-finding procedure of the MPC is completely independent of the preshower. To join the two systems, the track-vector found for each preshower track candidate is compared to each cluster found in the MPC. In Hough space, the closest matched MPC cluster is assigned to a preshower candidate. As this allows for the possibility for multiple preshower candidates to be associated to a single MPC cluster, a scan through all candidates with the same MPC cluster is made to determine which is closest. One reason for these multiple tracks is just fluctuations in the showering process which can form a spur of hits in multiple layers that happen to line-up in Hough-space. Multiple tracks can also be formed from the decay of particles, for example $\pi^0 \rightarrow \gamma\gamma$, these are treated in a second peak-finding algorithm.
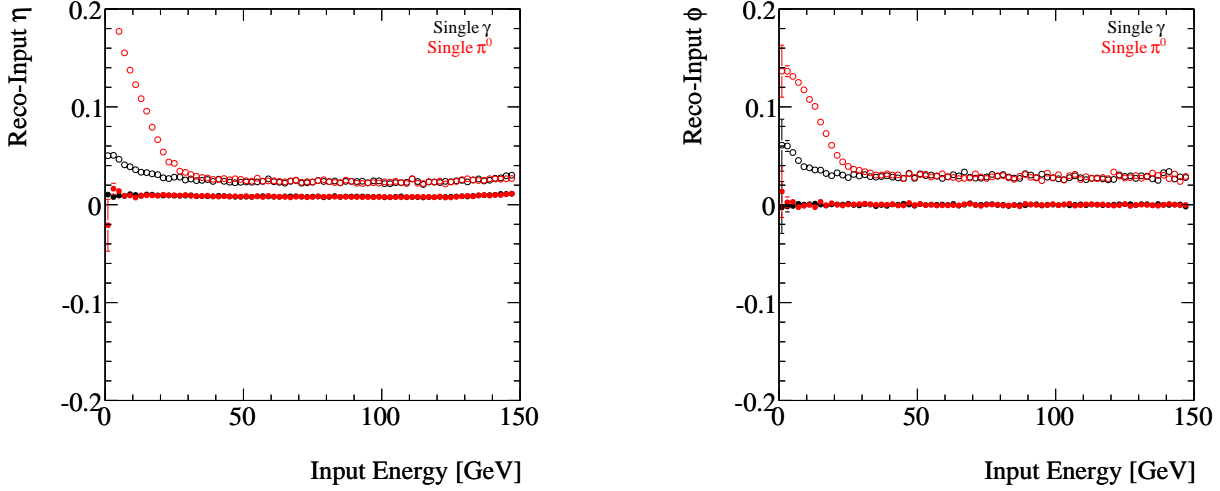
Figure 3.3: Pointing resolution of the MPC for single-γ (black) and single-π^0s versus the input energy of the particle. The left (right) panel shows the η (ϕ) resolution (open symbols) and offset (closed). The deviation between π^0s and γs observed at low energies is due to two distinct MPC clusters being found.

3.1.5   Single-track invariant mass calculation

Once an electromagnetic track candidate is found, it is tested to determine whether it is consistent with a single-electromagnetic shower or two close showers, similar to that expected from $\pi^0 \rightarrow \gamma\gamma$ decays. Only high energy tracks (E>20 GeV) and the closest track to a single MPC cluster are considered. First, all tracks outside a YYY region of interest are removed from the invariant mass analysis. The remaining hits are then divided into two halves (performed independently for x- and y-minipads). In a first test, the dividing line is the center of gravity. This is subsequently changed in an iterative fashion until a small change in the split-point results in no change in the energy assigned to each track, i.e. a stable point is found. Typically, the stable point is found at the first or second iteration.

It is important to note that the calculation of the invariant mass serves as a method to exclude π^0s from the analysis. If no invariant mass is found, then this is more likely to be a γ candidate, rather than a π^0. However, a two-track decay does not necessarily produce two discernable tracks. This will be discussed further in the next section.

Points of Failure

The reconstruction of the invariant mass is quite aggressive at rejecting all candidates which do not appear as π^0s. This helps to reconstructing π^0s, and forces all "failed" invariant mass reconstruction into one of two categories.
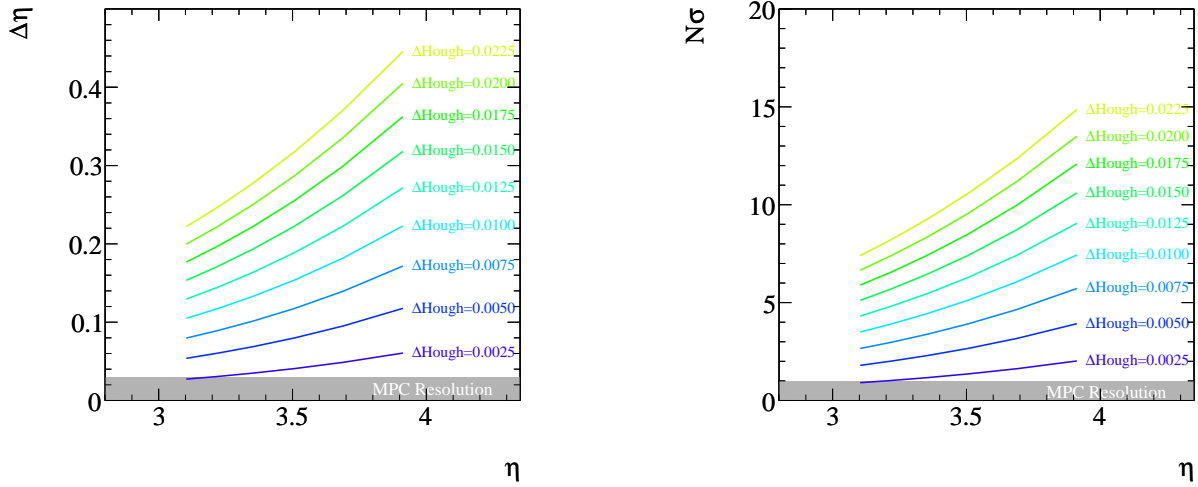
Figure 3.4: Hough slope difference cut compared to the pointing resolution of the MPC. The left panel shows the absolute $\Delta\eta$ for a prospective difference in Hough slope between the MPC and the pre-shower. The right panel shows the same data, but divided by the approximate resolution of the MPC (0.03). Colored lines represent the limit of difference between the MPC and the pre-shower. The grey box shows the approximate MPC resolution.
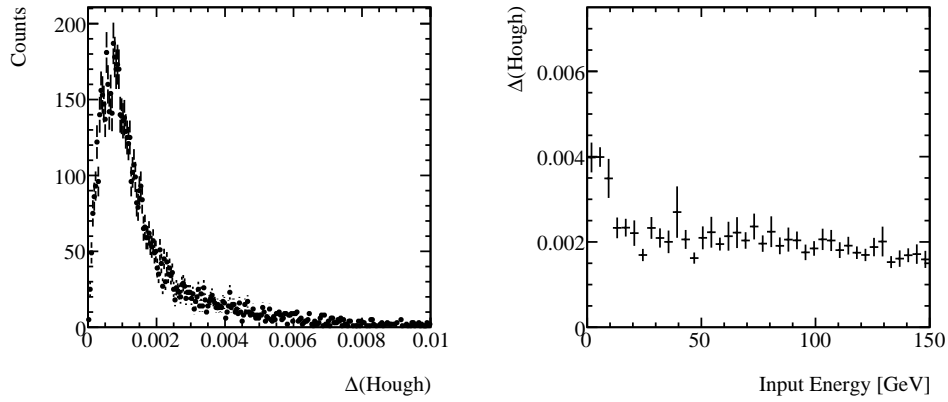
Figure 3.5: The left panel shows the $\Delta(Hough)$ distribution in a single-γ simulation; the right panel shows the dependence on the input energy.

The first category deals with candidates which have too few minipad hits associated with the track. In this case an invariant mass of "-2" is assigned. It is found that many of these (some 20-25% of all candidates) fail due to a failure of the track matching rather than of no hits in the detector. Specifically, in the current implementation, the resolution of the MPC is too low to reliably select the "correct" track as the smallest difference in Hough space.

Figure 3.6: Number of minipad-tracks per MPC cluster. The left panel shows a simulation of single-γs, the right shows single-π^0s. The color scale is logarithmic.

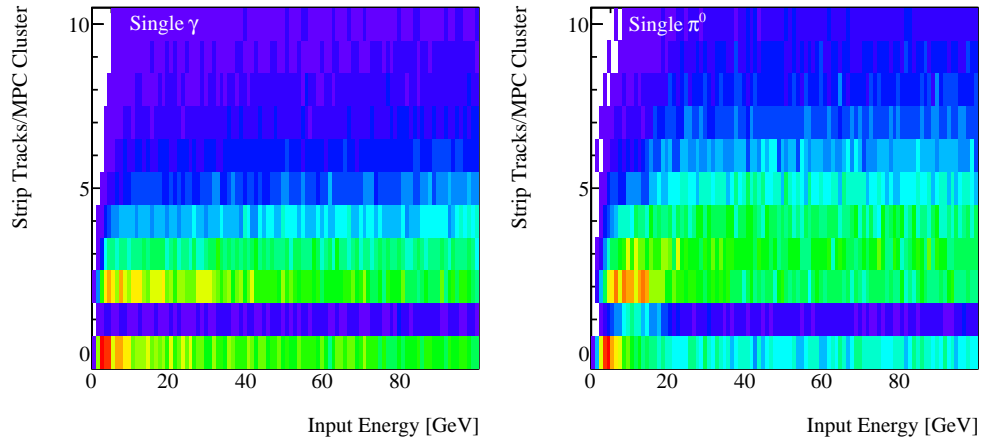The second point of failure occurs when the algorithm cannot divide the energy up enough to separate two distinct peaks in the x- or y-directions. The reason for this could be a real single-γ (for example a signal photon), an asymmetrically decayed π^0, a track-matching failure whereby only one track (from a π^0 decay) falls in the acceptance.

As the first point of failure is due to an error (did not associate the correct track to an MPC cluster), it is likely that π^0 and γ will contribute equally. It was found that the relative amount of single-track π^0 and γ was the same for this category. Thus, by dividing the points of failure into multiple categories, it becomes possible to sort the real photon-candidates from the fake ones, with less dilution.

figure: need something to back up these wild accusations..

3.1.6   Energy Recalibration

The reconstructed energy is formed independently from the silicon preshower and the MPC crystals. Figure 3.7 (left panel) shows the amount of energy typically deposited in each section as a function of the input energy. Less than 20% of the total input energy is reconstructed in the preshower. To estimate the total energy, one needs to recalibrate the energy reconstructed in the MPC. The current MPC cluster finding calibrations assumes that there is no impedance due to a silicon-tungsten preshower to the photon prior to it's entry into the detector. As approximately four radiation lengths of additional material is now traversed by an impinging photon, the MPC energy is mis-calculated. Here, we simply apply a calibration to the expected energy in the MPC.

The calibration itself is a complicated function (see Eq. 3.1). The relevant scaling variable found for this procedure is the ratio of the preshower to the MPC energy, $fRat$. The
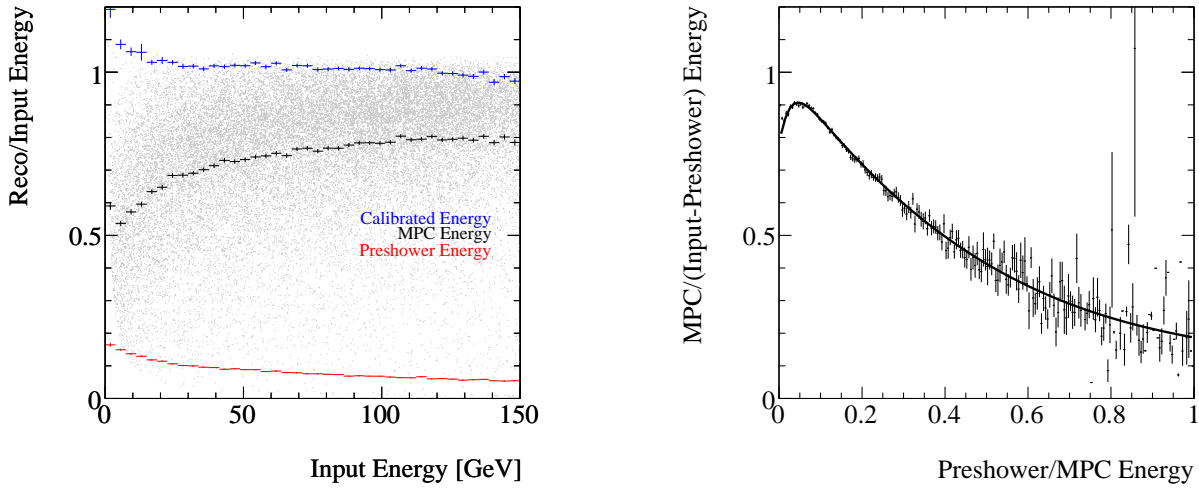
Figure 3.7: The left panel shows the energy deposition in the preshower (red) and MPC (black profile, grey symbols). The blue histogram represents the calibrated data. Most energy is deposited in the MPC, with a diminishing amount in the preshower for larger input energies. The right panel shows the calibration method used, see text for details.

calibration is made from a sample of single γs at various energies. The measured MPC energy is divided by the known input energy of the γ minus the measured energy from the preshower. This difference then represents the amount of energy which needs to be reconstructed in the MPC. Figure 3.7 (right panel) shows this ratio as a function of $fRat$.

To best fit the distribution, a third order polynomial is first fit in the region $0.1 < fRat < 1$. Next, the distribution is reformed and scaled by this polynomial function. A second fit, using an exponential form, is then made to represent the sharp inversion at low $fRat$.

$$Polynomial * Exponential$$
$$([0] + [1] * fRat + [2] * fRat^2 + [3] * fRat^3) * ([4]/([5] + exp([6] * fRat))) \qquad (3.1)$$

The parameters of the fit can be found in Table 3.2. For cases when the preshower energy exceeds that of the MPC, the energy calibration is fixed to a constant value of 0.234, due to statistical limitations. The final calibration can be seen in the left panel of Fig. 3.7 (blue symbols). The data in the energy region of interest ($>20\,\text{GeV}$) is in good agreement with the input energy.

Table 3.1: Parameters for energy calibration.

Function	Parameter Number	Value
Polynomial	0	1.021955
	1	-1.773316
	2	1.273648
	3	-0.3360244
Exponential	4	3.20540
	5	3.19592
	6	-43.3335

3.2   EM Shower Reconstruction Performance: γ and π^0.

3.2.1   Overview of Section

In this section, the reconstruction performance is evaluated and discussed in the context of single γ and π^0 simulations. This is followed by a brief discussion of the performance in a minimum bias simulation of pp events using PYTHIA.

3.2.2   Basic cuts used in the reconstruction

In this analysis, a series of "basic cuts" are applied to all data to clean-up the event sample prior to more detailed analysis. The first cut is to select only tracks with a reconstructed energy of at least 20 GeV. Below this limit the number of π^0s which form two distinct MPC clusters increases, thus most tracks below this limit are single-γ's. The tracks below this limit can be used to reconstruct π^0s using a two-track method as used in current MPC-only analyses.
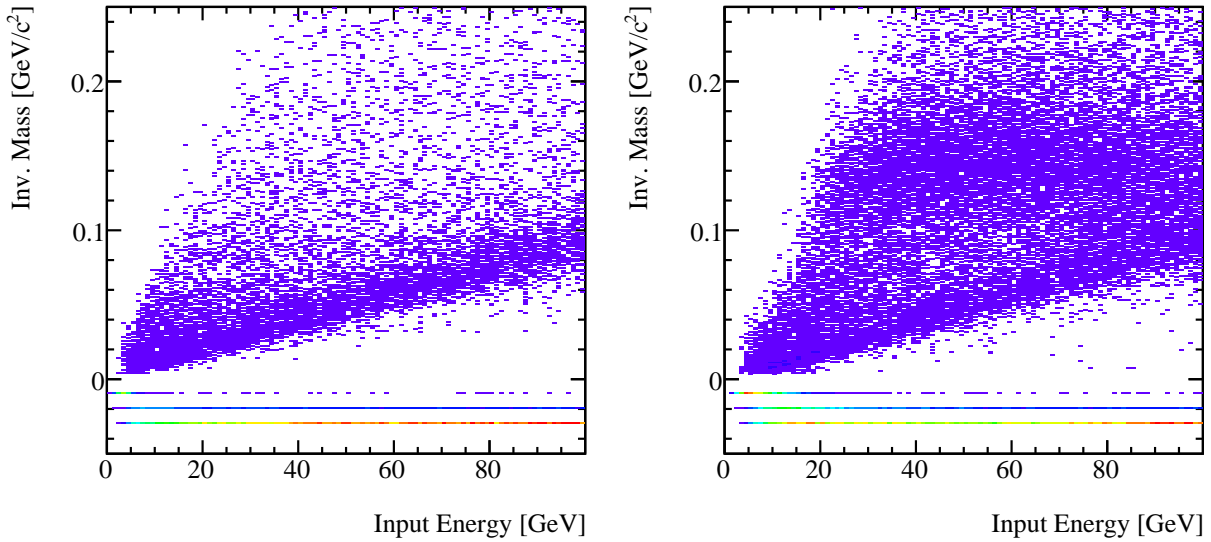
Figure 3.8: Single-track invariant mass reconstruction for the full reconstructed energy range. Below $E_{\text{Rec}} = 20$ GeV the reconstruction of two γs associated to a single MPC clusters drops significantly. The "negative" invariant mass is a code for the step at which the reconstruction bailed and did not produce an invariant mass.

Next only the preshower track tagged as "closest" to an MPC cluster is considered in the analysis. An additional requirement that the preshower track vector and the direction vector formed from the MPC clusters of $\Delta(\text{Hough}) < 0.0025$ (in Hough space) are accepted, see Fig. 3.5.

Finally, a fiducial cut in η-space is made such that tracks reconstructed around the edge of the preshower are rejected. These are typically malformed and may have missing or distorted energy signals for example. Figure 3.9 shows the pseudoreapidity dependence of reconstructed tracks in a single-particle simulation of γs. The input η was left open (black histogram), and the full reconstruction was run. By selecting tracks with both an MPC and preshower component, with the latter being "closest", the pseudorapidity coverage was found to be $\sim 3.1 < \eta < \sim 4.2$ (red). The requirement of a minimum energy serves only to reduce statistics, as expected (blue).
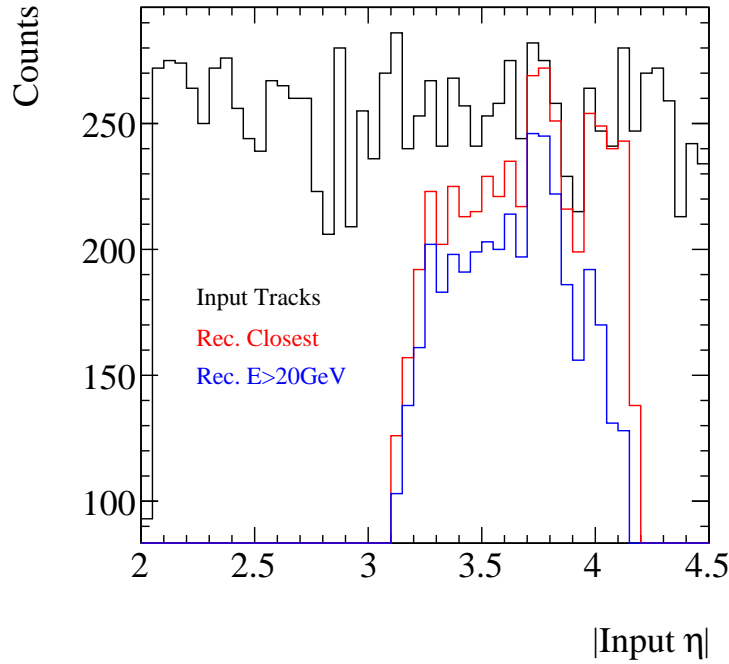
Figure 3.9: η distribution of single-γs from a simulation where the input distibution is wider than the acceptance of the detector (black). The reconstructed closest tracks (red) and those with a reconstructed energy greater than 20 GeV (blue) are shown.

Figure 3.10 shows the reconstructed energy (left panels) and η (right panels) relative to the input value. The upper panel depict this versus the input η for each event, and the lower show this versus the input energy. The black (red) histogram shows the distribution for γs (π^0s). The accuracy of the reconstructed η is found to degrade for low η (worse for π^0s), whilst the energy reconstruction degrades only as a function of energy.

Figure 3.10: Reconstructed energy (left figures) and reconstructed η (right) as a function of η (top) and energy (bottom).

3.2.3   Reconstruction Performance

Position Resolution
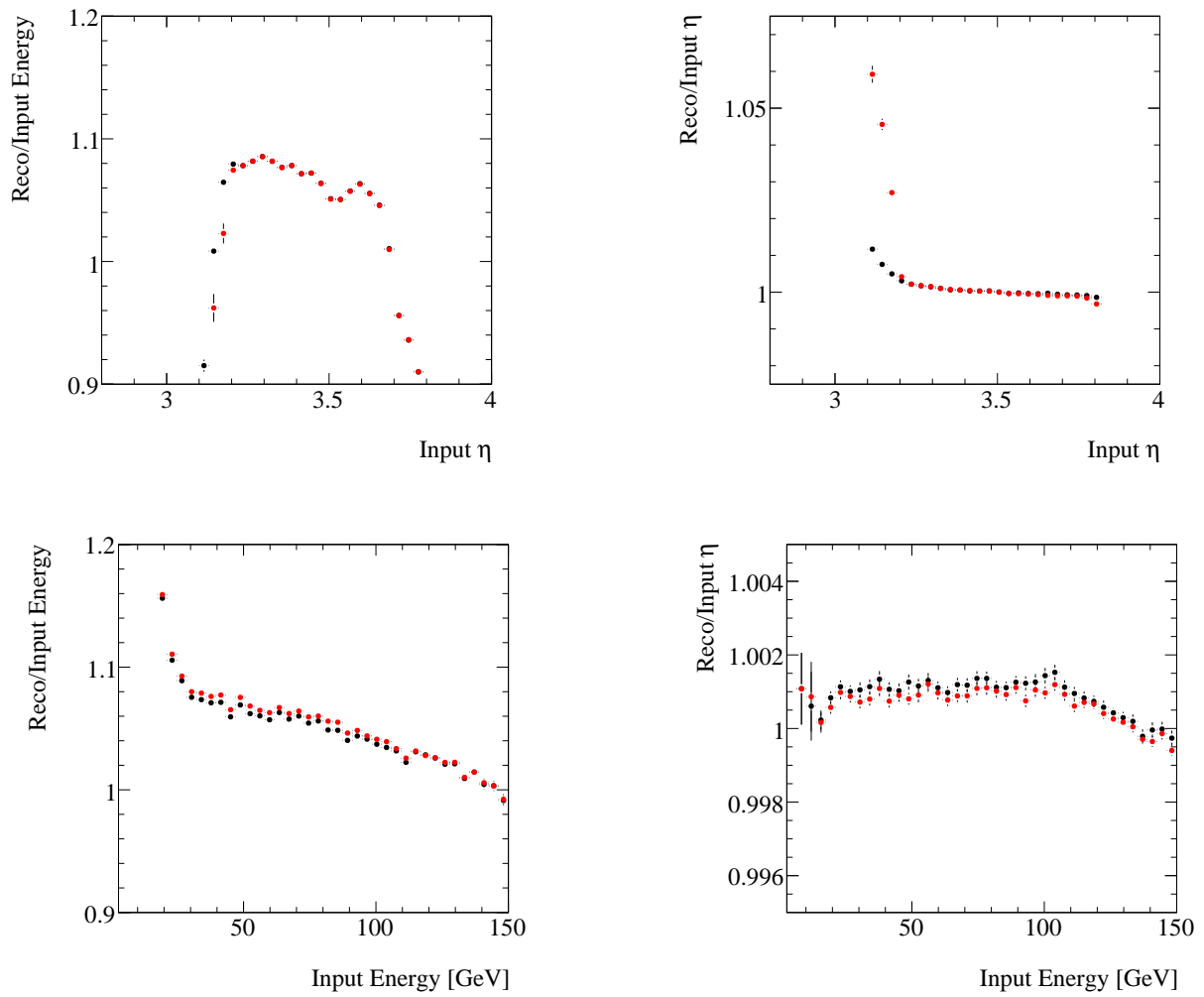
The resolution and offset to the reconstructed track vector, relative to the input vector of the particle, for a single-γ and single-π^0 simulations is shown in Fig. 3.11. The left panel shows the η resolution (open symbols) and offset (closed) for single-γ and single-π^0 simulations.
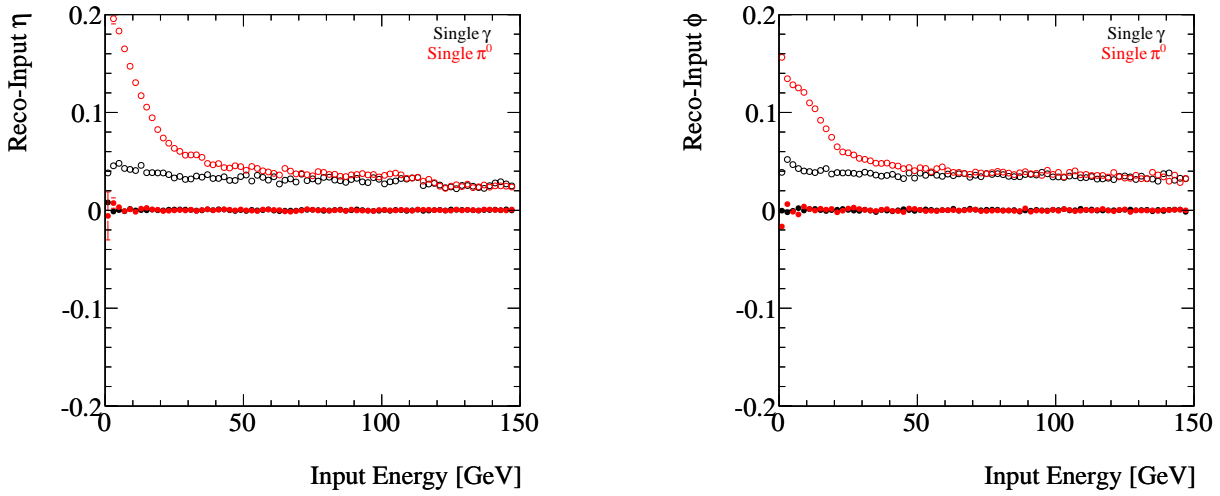
Figure 3.11: η (left panel) and ϕ (right) resolution (open symbols) and offset (closed) for single-γ (black) and single-π^0s. The deviation between π^0s and γs observed at low energies is due to two distinct MPC clusters being found.

Energy Resolution

The resolution and offset to the reconstructed energy for a single-γ and single-π^0 simulations is shown in Fig. 3.11. The left panel shows the η resolution (open symbols) and offset (closed) for single-γ and single-π^0 directed into the MPCEX acceptance. The right panel shows the ϕ resolution.

Invariant Mass Reconstruction

Using the silicon strips, an invariant mass can be reconstructed for showers in their infancy, which are too close to distinguish as separate tracks in the MPC. This invariant mass, reconstructed for "single-tracks" (i.e. using single MPC clusters) is optimized to find π^0s. The algorithm tests whether the two infant tracks are sufficiently separated into two
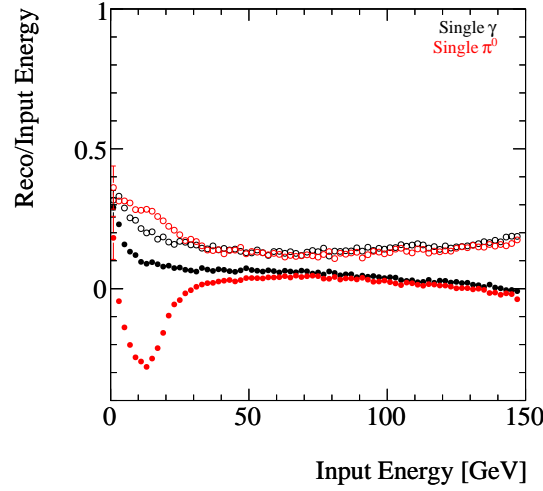
53

Figure 3.12: Energy resolution (open symbols) and offset (closed) for single-γ (black) and single-π^0s. The deviation between π^0s and γs observed at low energies is due to two distinct MPC clusters being found.

distinct bands in the preshower. If this is not the case, the an invariant mass is not recorded. This means that most of the signal γs will not form an invariant mass, but instead will be encoded to be at the stage at which the reconstruction failed. On the other hand, the reconstruction of the π^0s, when successful, reproduces a clear peak at the correct mass.

Figure 3.13 shows the reconstructed invariant mass versus the reconstructed energy for single input γs (left) and π^0s (right). A cut in the reconstruction at $E = 20\,\text{GeV}$ is applied as below this, two distinct tracks are typically found in the detector, see Fig. 3.8. A more detailed view of this can be found in Figs. 3.14 to 3.20, where slices in reconstructed energy are made in $\Delta E = 5\,\text{GeV}$ bins. Figure 3.14 (left) shows the $20 < E_{\text{Rec}} < 25\,\text{GeV}$ bin. The red histogram shows single-π^0s, where a small correct-mass peak is observed, black shows single-γs reconstructed at the same energy. A significant low-mass tail is observed for single-π^0s which is due to the reconstruction algorithm picking up a fluctuation in energy from a single shower and thus reconstructing a mass based from one γ. The normalization of the two histograms was made to fix the maximum height to be the same. Figure 3.14 (right) shows the $25 < E_{\text{Rec}} < 30\,\text{GeV}$ bin. A more prominent correct-mass peak is observed. At higher reconstructed energies, the correct-mass peak becomes dominant and the low-mass peak shrinks (relatively). The overall low mass peak distribution, however, still retains the same shape as that from single-γs.
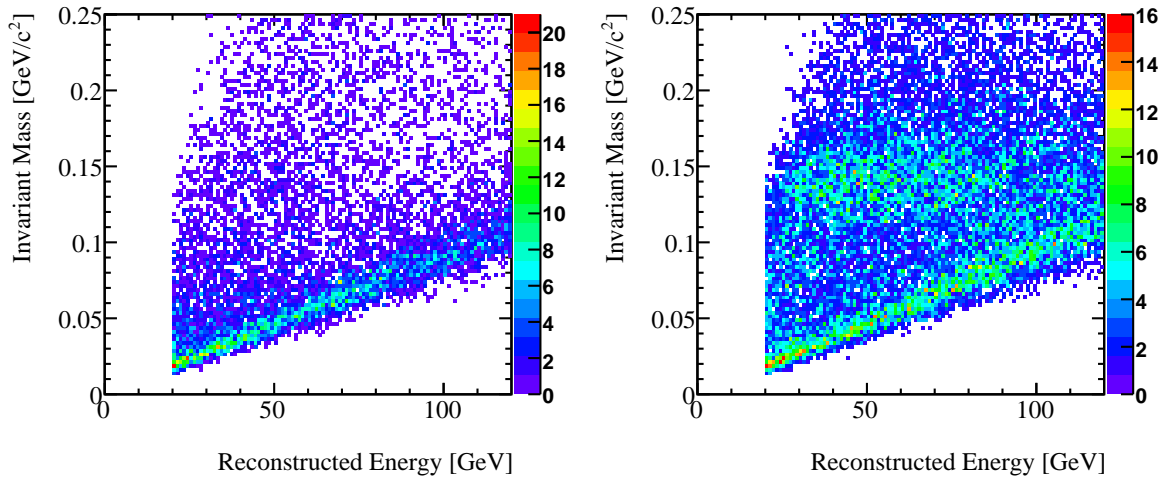
Figure 3.13: The left (right) panel shows the reconstructed invariant mass versus reconstructed energy for γs (π^0s).
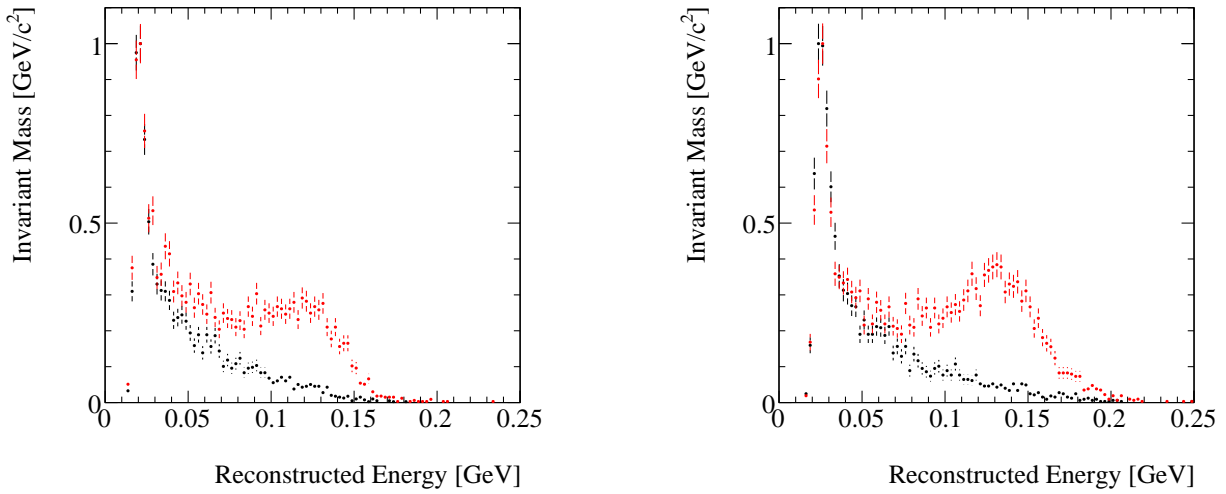
Figure 3.14: Comparison of the invariant mass distribution for γs (black) and π^0s (red) for the 20<E<25 GeV (25<E<30 GeV) energy range.
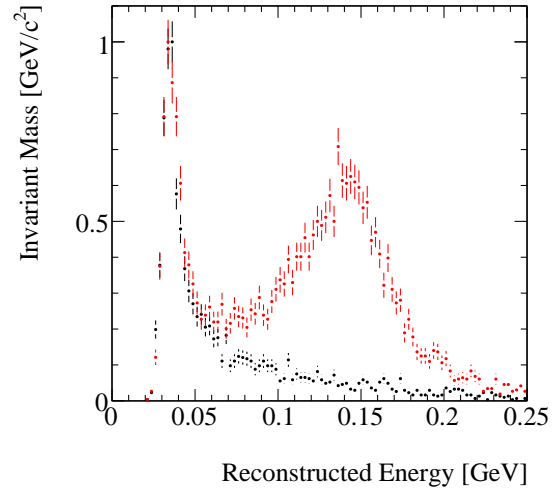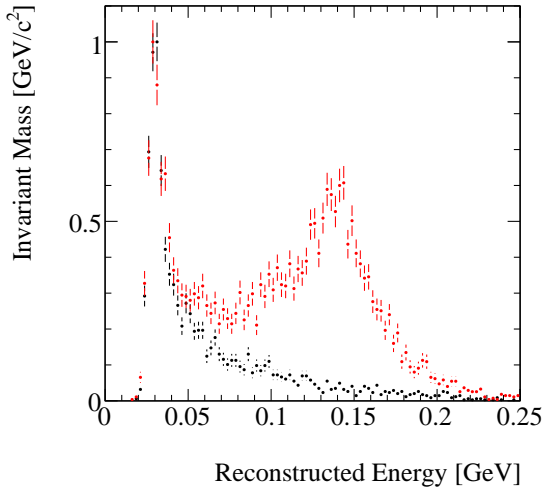
Figure 3.15: Comparison of the invariant mass distribution for γs (black) and π^0s (red) for the 30<E<35 GeV (35<E<40 GeV) energy range.
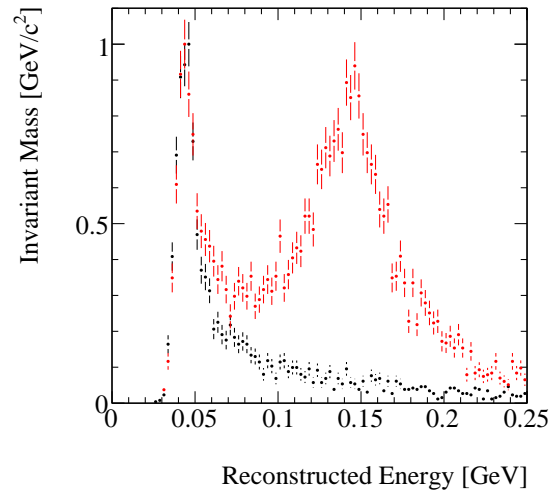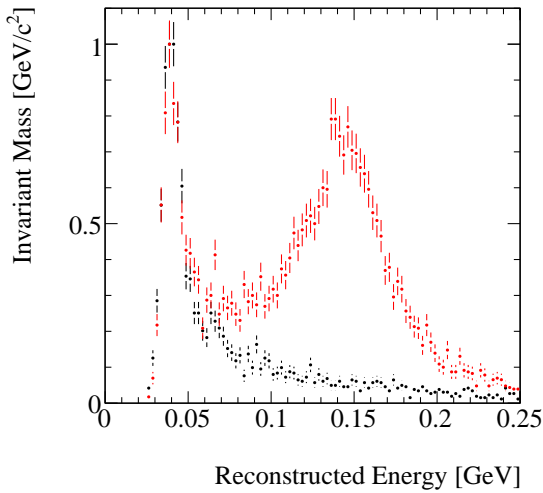
Figure 3.16: Comparison of the invariant mass distribution for γs (black) and π^0s (red) for the 40<E<45 GeV (45<E<50 GeV) energy range.
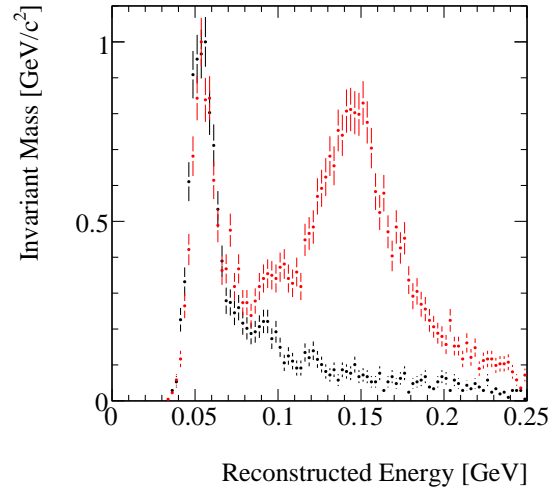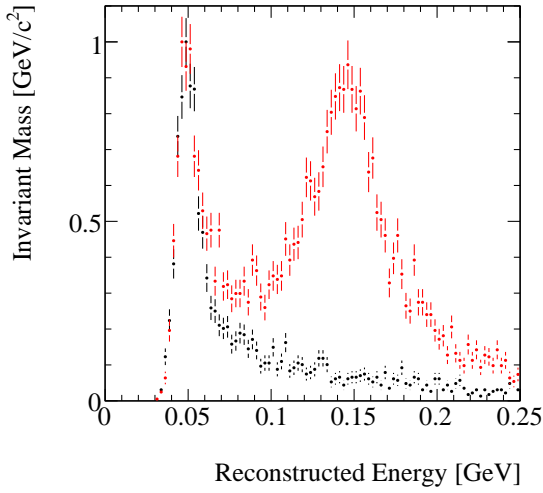
Figure 3.17: Comparison of the invariant mass distribution for γs (black) and π^0s (red) for the $50{<}E{<}55\,\mathrm{GeV}$ ($55{<}E{<}60\,\mathrm{GeV}$) energy range.
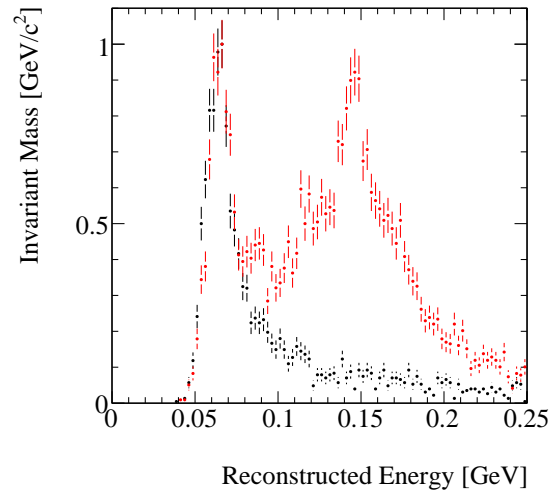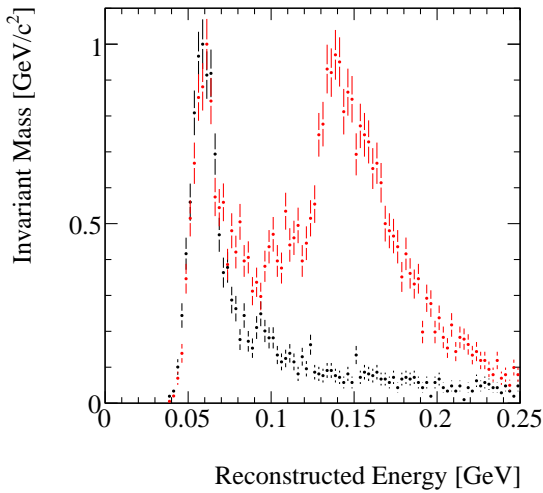
Figure 3.18: Comparison of the invariant mass distribution for γs (black) and π^0s (red) for the $60{<}E{<}65\,\mathrm{GeV}$ ($65{<}E{<}70\,\mathrm{GeV}$) energy range.
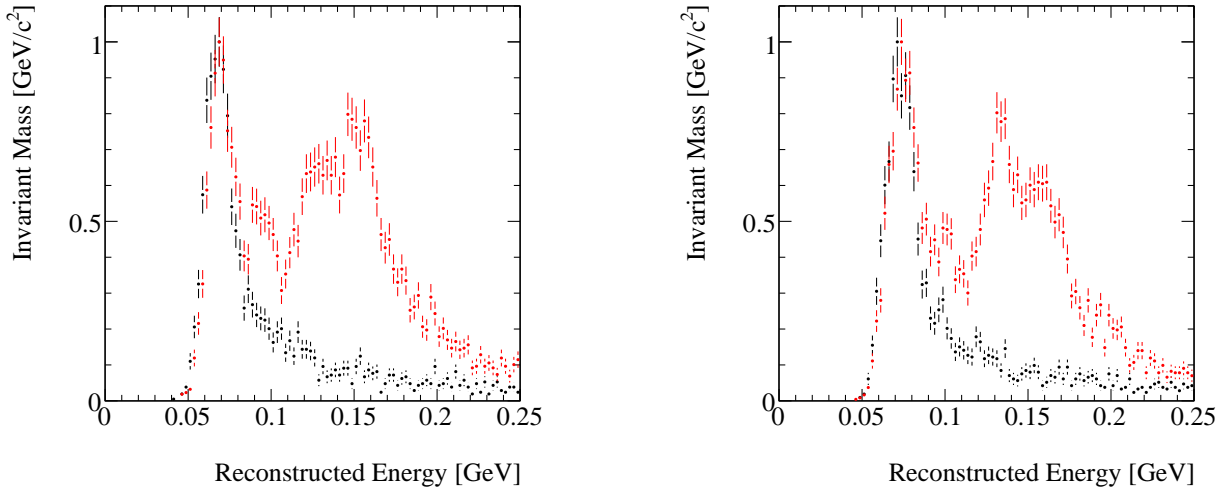
Figure 3.19: Comparison of the invariant mass distribution for γs (black) and π^0s (red) for the $70 < E < 75\,\text{GeV}$ ($75 < E < 80\,\text{GeV}$) energy range.
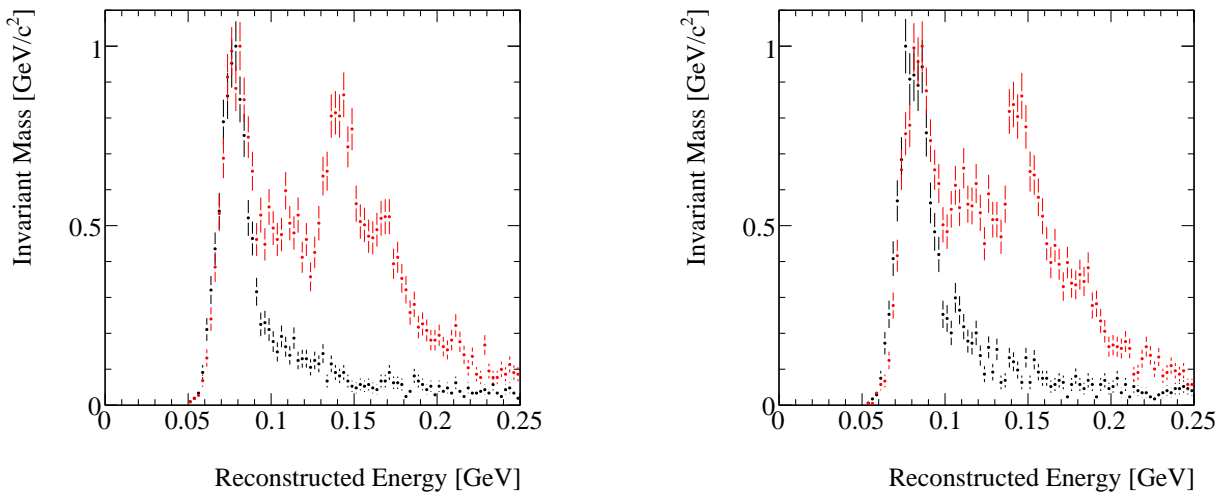
Figure 3.20: Comparison of the invariant mass distribution for γs (black) and π^0s (red) for the $80 < E < 85\,\text{GeV}$ ($85 < E < 90\,\text{GeV}$) energy range.

Single-Particle Reconstruction Efficiencies

Table 3.2: Single-Particle Reconstruction Efficiency. The first column are the number of MC particles thrown into MPCEX with the stated energy. The second column are the number in the reconstruction which passed all the cuts, note that there is no restriction on the incoming particle energy applied, so in- and out-flow are possible. The percentages in this column relative to the input tracks. The next columns are the number of tracks which "passed" the reconstruction cuts, the percentages are "per reconstructed track". Fail 1 (2) denotes the two failure categories discussed above.

Energy Range		Thrown	Passed	Inv. Mass >0	Fail 1	Fail 2
>20 GeV	γ	210773	186604	51468	15770	119366
		100%	88.5%	27.5%	8.4%	63.9%
	π^0	210628	204883	116969	13718	74196
		100%	97.2%	57%	6.6%	36.2%
20-25 GeV	γ	13217	10899	3765	1330	5804
		100%	82.4%	34.5%	12.2%	53.2%
	π^0	13378	11166	5675	1560	3931
		100%	83.4%	50.8%	13.9%	35.2%
25-30 GeV	γ	13256	10753	3503	1248	6002
		100%	81.1%	32.5%	11.6%	55.8%
	π^0	13173	11520	6111	1352	4057
		100%	87.4%	53%	11.7%	35.2%
30-35 GeV	γ	12953	10954	3365	1176	6413
		100%	84.5%	30.7%	10.7%	58.5%
	π^0	13133	11897	6782	1179	3936
		100%	90.5%	57%	9.9%	33%
35-40 GeV	γ	13122	10910	3189	1063	6658
		100%	83.1%	29.2%	9.7%	61%
	π^0	13070	12138	7155	1059	3924
		100%	92.8%	58.9%	8.7%	32.3%
40-45 GeV	γ	13040	11161	3189	1057	6915
		100%	85.5%	28.5%	9.4%	61.9%
	π^0	13264	12236	7233	967	4036
		100%	92.2%	59.1%	7.9%	32.9%
45-50 GeV	γ	13055	11176	3207	987	6982
		100%	85.6%	28.6%	8.8%	62.4%
	π^0	13217	12350	7562	861	3927
		100%	93.4%	61.2%	6.9%	31.7%

Table 3.3: Continuation of Tbl. 3.2.

Energy Range		Thrown	Passed	Inv. Mass >0	Fail 1	Fail 2
50-55 GeV	γ	13126	11283	3069	976	7238
		100%	85.9%	27.2%	8.6%	64.1%
	π^0	12879	12253	7514	789	3950
		100%	95.1%	61.3%	6.4%	32.2%
55-60 GeV	γ	13306	11576	3166	1011	7399
		100%	86.9%	27.3%	8.7%	63.9%
	π^0	13095	12571	7752	739	4080
		100%	95.9%	61.6%	5.8%	32.4%
60-65 GeV	γ	13273	11573	3235	904	7434
		100%	87.1%	27.9%	7.8%	64.2%
	π^0	13188	12865	7827	710	4328
		100%	97.5%	60.8%	5.5%	33.6%
65-70 GeV	γ	13438	11937	3404	879	7654
		100%	88.8%	28.5%	7.3%	64.1%
	π^0	13375	13003	7819	696	4488
		100%	97.2%	60.1%	5.3%	34.5%
70-75 GeV	γ	13187	12496	3322	924	8250
		100%	94.7%	26.5%	7.3%	66%
	π^0	13228	13732	7937	735	5060
		100%	103.8%	57.7%	5.3%	36.8%
75-80 GeV	γ	13155	12769	3346	848	8575
		100%	97%	26.2%	6.6%	67.1%
	π^0	13028	14418	8267	627	5524
		100%	110.6%	57.3%	4.3%	38.3%
80-85 GeV	γ	13338	12485	3133	895	8457
		100%	93.6%	25%	7.1%	67.7%
	π^0	13195	14074	7802	690	5582
		100%	106.6%	55.4%	4.9%	39.6%
85-90 GeV	γ	13136	12349	2949	844	8556
		100%	94%	23.8%	6.8%	69.2%
	π^0	13378	13536	7399	604	5533
		100%	101.1%	54.6%	4.4%	40.8%

3.2.4 χ^2 Calibration

The χ^2 calibration is an important piece of the electromagnetic shower reconstruction. The purpose is to remove contamination from charged hadrons, which may masquerade as e-m showers. E-M showers are distinct as, for a given energy, the shower profile is somewhat predictable. For charged hadrons, the shower profile is different, sometimes a shower develops, sometimes only MIPs are seen in the silicon.

A χ^2 is formed to characterize the shower profile at each layer in the silicon with the aim to reduce the charged hadron contamination. Both the energy deposited and the transverse profile of the shower in each layer are measured for many events, then the mean and RMS of those distributions are found as references. Figures 3.21 and 3.22 show the mean and RMS of the calibration, versus collision energy, for the energy deposition profile and transverse profile respectively. The calibration is performed twice, once for single-γs, and again as a cross-check with single-π^0s. The energy deposition, as expected, is very similar for the two cases, as the both are e-m showers. However, the width is distict, as the π^0 showers are from two separated γs. For higher reconstructed energies, those distributions start to approach each other, as the angular separation diminishes.
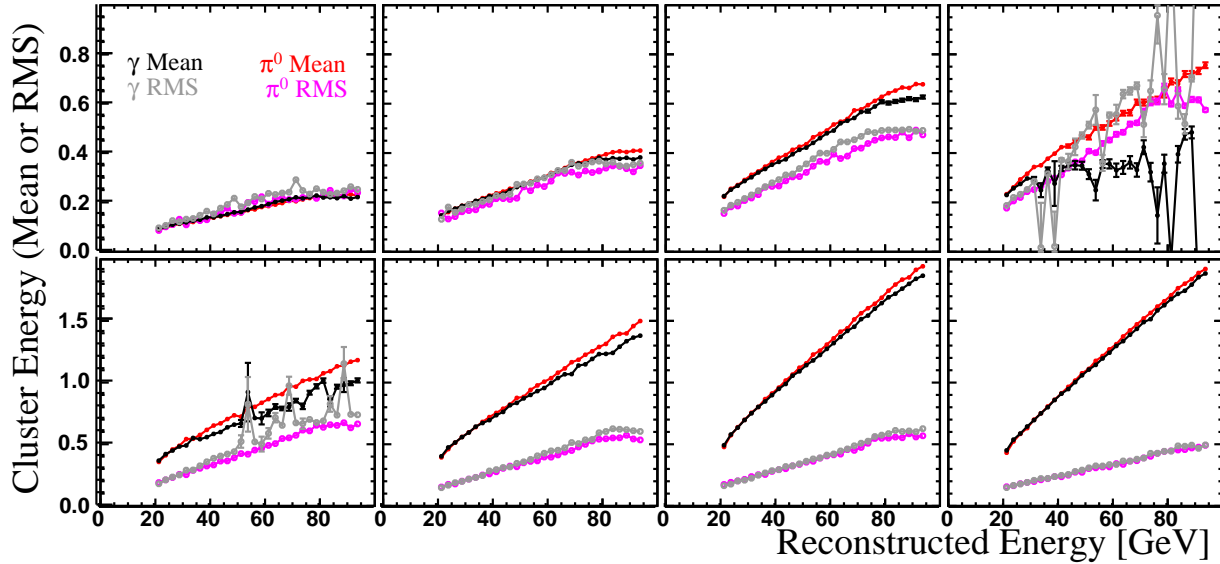
Figure 3.21: Calibration of the energy deposition profile for a reconstructed track. The calibration is performed using single-γs and single-π^0s. The top row (left to right) show the layers 0 through 3, the bottom row 4 through 7. The black/grey symbols show the mean/RMS of the single-γ distribution. The red/purple symbols show the mean/RMS of the single-π^0 distribution.

Four final χ^2 methods are used in the analysis, with varying degrees of success. Two (one in energy, the other in width) are based from the χ^2 formed from all layers, a second pair is derived from only the last 3 layers, where the showers are more definitely defined. As an example, Fig 3.23 shows the four cases for the lowest energy consid-
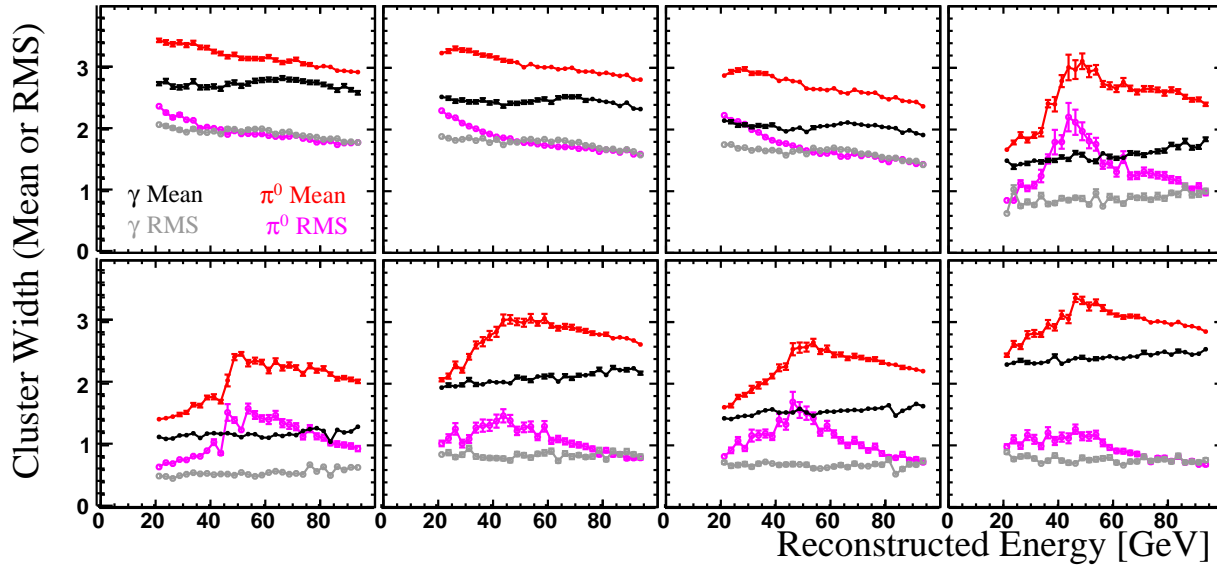
Figure 3.22: Calibration of the transverse profile at each layer for a reconstructed track. The calibration is performed using single-γs and single-π^0s. The top row (left to right) show the layers 0 through 3, the bottom row 4 through 7. The black/grey symbols show the mean/RMS of the single-γ distribution. The red/purple symbols show the mean/RMS of the single-π^0 distribution.

ered ($20.0 < E_{\text{Rec}} < 22.5$ GeV). Energy bins $40.0 < E_{\text{Rec}} < 42.5$ GeV, $60.0 < E_{\text{Rec}} < 62.5$ GeV, and $80.0 < E_{\text{Rec}} < 82.5$ GeV are shown in Figs. 3.24, 3.25, and 3.26 respectively.
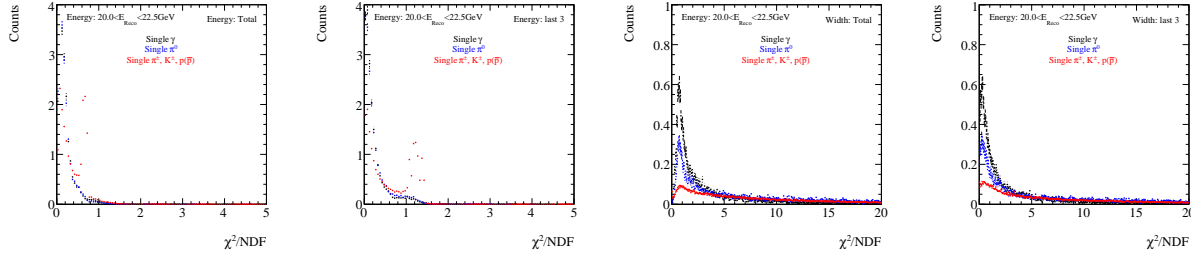
Figure 3.23: χ^2 calibration applied to single-γs (black), single-π^0s (red), and single-charged hadrons (mixed $\pi^\pm$, $K^\pm$, and $p(\overline{p})$), with reconstructed energy of $20 < E_{\text{Rec}} < 22.5$ GeV. Left to right, the panels show the calibration using energy (all layers), energy (last 3 only), width (all layers), and width (last 3 only).

Using these calibrations, one can define a χ^2 cut for each of the methods. Figure 3.30 shows the cut positions, as a function of reconstructed energy, which keeps about 90% of the single γs. The effect applying these cut to the single-π^0s, and single-charged hadrons is shown in Fig. 3.28 (energy χ^2) and Fig. 3.29 (width χ^2) as a fraction of the total which were reconstructed.

The χ^2 for any event sample is then calculated relative to those references, and summed over each layer.
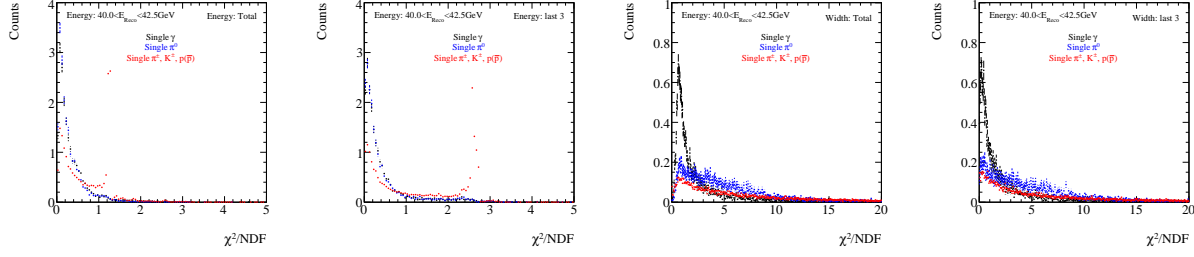
Figure 3.24: χ^2 calibration applied to single-γs (black), single-π^0s (red), and single-charged hadrons (mixed $\pi^\pm$, $K^\pm$, and $p(\overline{p})$), with reconstructed energy of $40 < E_{\text{Rec}} < 42.5$ GeV. Left to right, the panels show the calibration using energy (all layers), energy (last 3 only), width (all layers), and width (last 3 only).
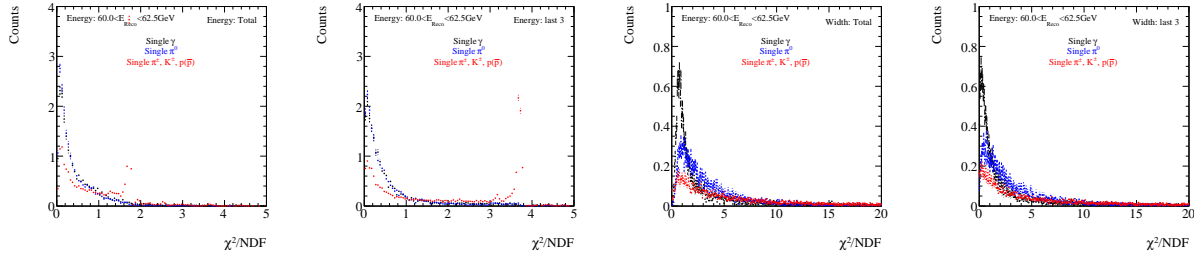
Figure 3.25: χ^2 calibration applied to single-γs (black), single-π^0s (red), and single-charged hadrons (mixed $\pi^\pm$, $K^\pm$, and $p(\overline{p})$), with reconstructed energy of $60 < E_{\text{Rec}} < 62.5$ GeV. Left to right, the panels show the calibration using energy (all layers), energy (last 3 only), width (all layers), and width (last 3 only).
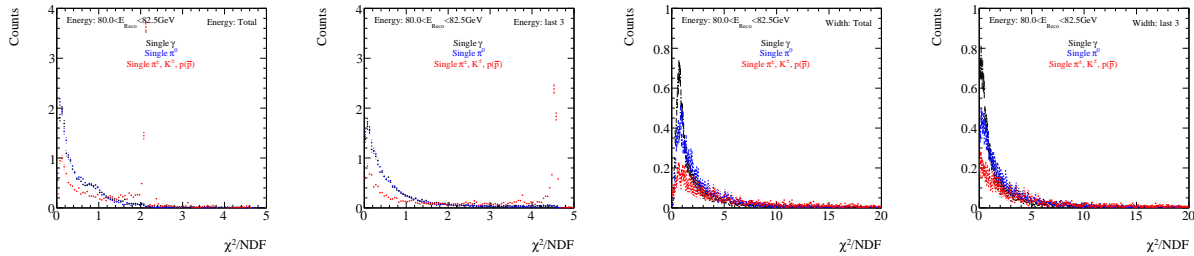
Figure 3.26: χ^2 calibration applied to single-γs (black), single-π^0s (red), and single-charged hadrons (mixed $\pi^\pm$, $K^\pm$, and $p(\overline{p})$), with reconstructed energy of $80 < E_{\text{Rec}} < 82.5$ GeV. Left to right, the panels show the calibration using energy (all layers), energy (last 3 only), width (all layers), and width (last 3 only).
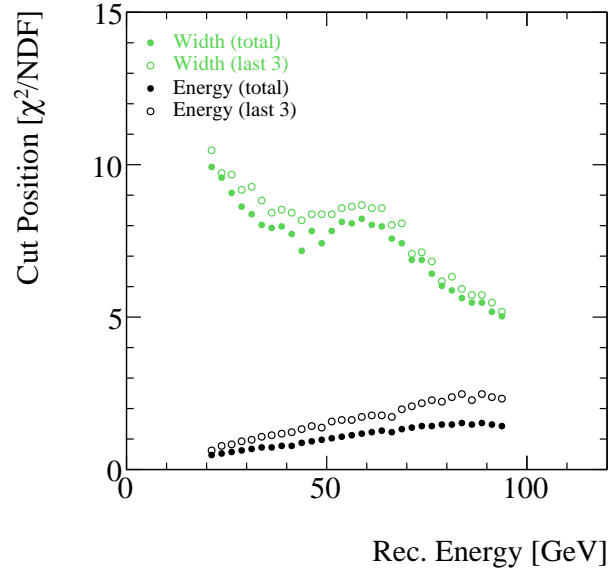
Figure 3.27: χ^2 cut positions, determined to retain 90% of single-γs for the energy (black) and width (green) methods. "Total" and "last 3" are depicted as closed and open symbols respectively.
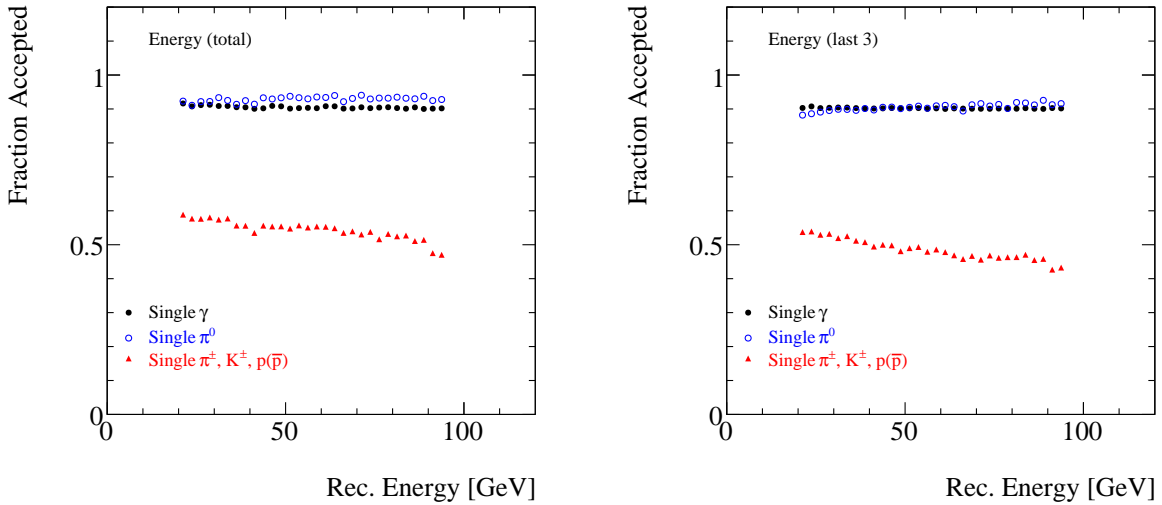
Figure 3.28: Fraction of single-γs (black), single-π^0 (blue), and charged hadrons (red) retained by the energy total (right panel) and last 3 method (left). The cut position was set such that 90% of single-γ passed the cuts.
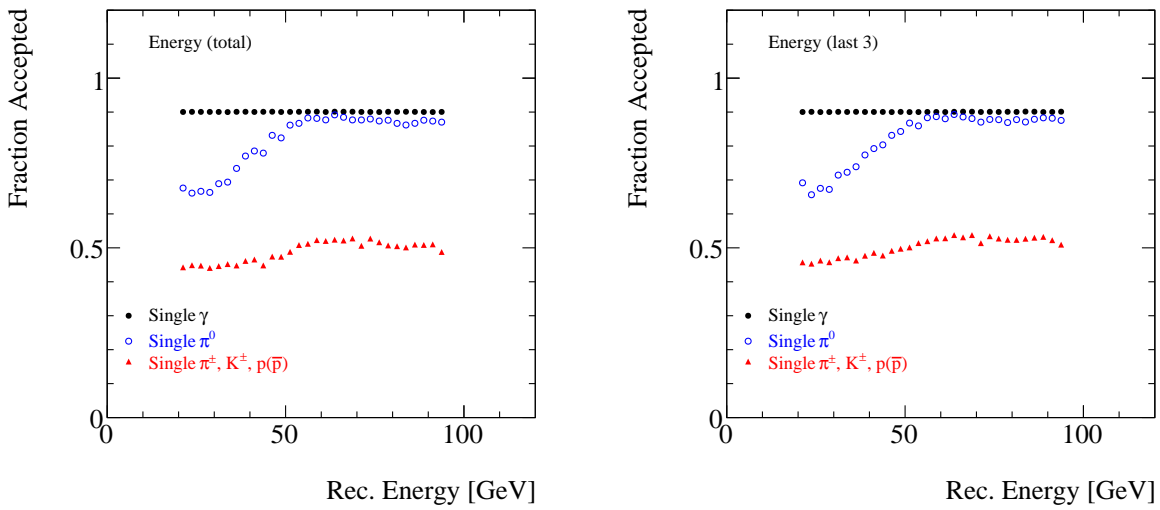
Figure 3.29: Fraction of single-γs (black), single-π^0 (blue), and charged hadrons (red) retained by the width total (right panel) and last 3 method (left). The cut position was set such that 90% of single-γ passed the cuts.
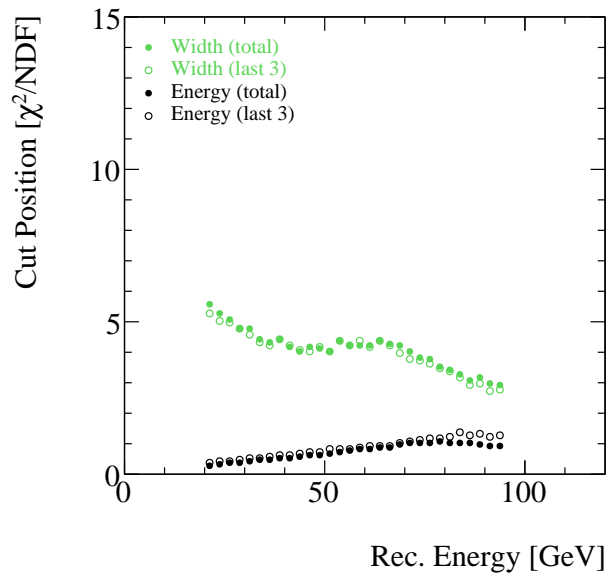
Figure 3.30: χ^2 cut positions, determined to retain 80% of single-γs for the energy (black) and width (green) methods. "Total" and "last 3" are depicted as closed and open symbols respectively.
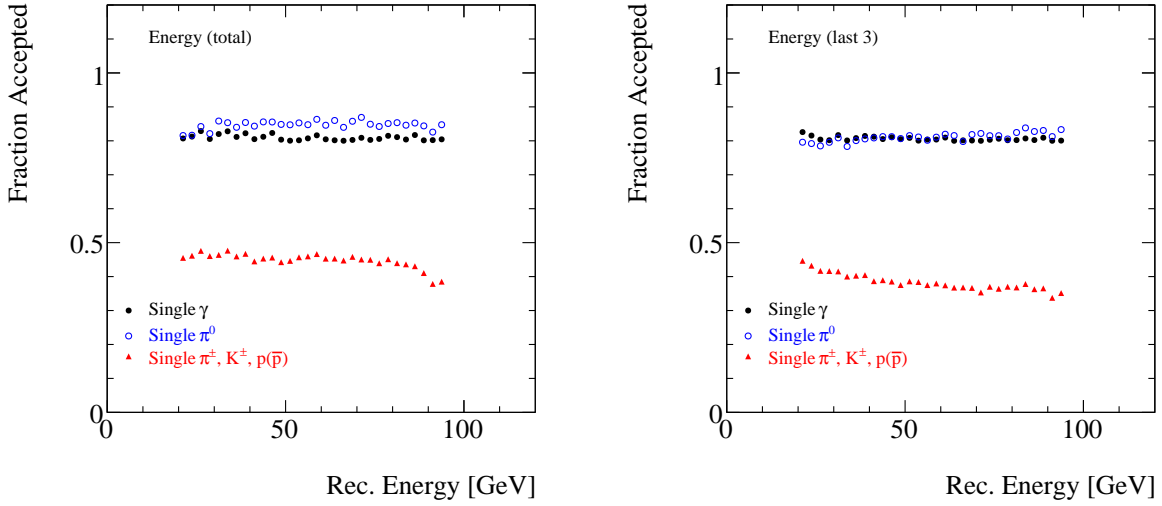
Figure 3.31: Fraction of single-γs (black), single-π^0 (blue), and charged hadrons (red) retained by the energy total (right panel) and last 3 method (left). The cut position was set such that 80% of single-γ passed the cuts.
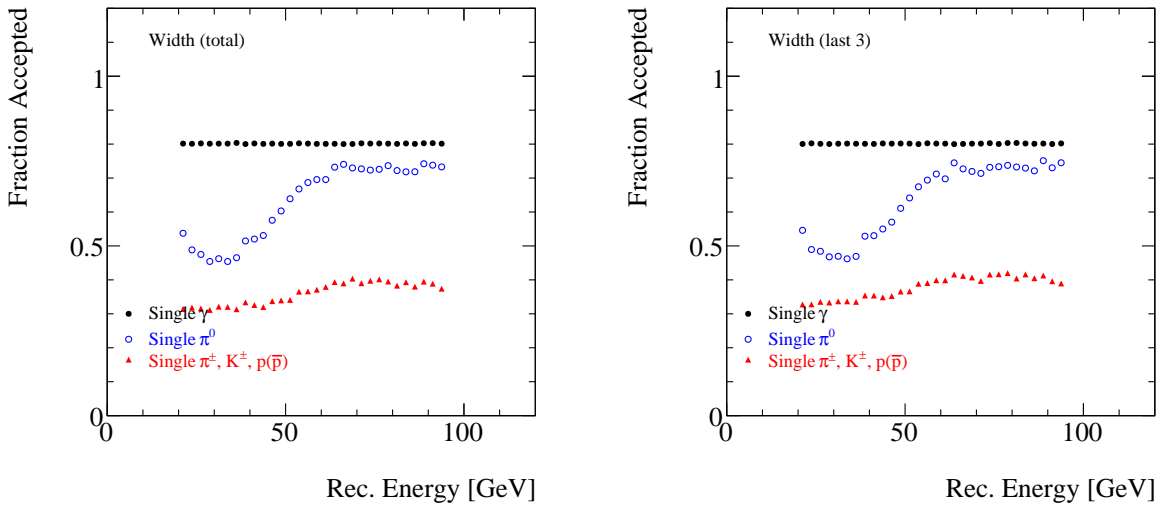
Figure 3.32: Fraction of single-γs (black), single-π^0 (blue), and charged hadrons (red) retained by the width total (right panel) and last 3 method (left). The cut position was set such that 80% of single-γ passed the cuts.

3.2.5   Reconstruction in PYTHIA events

Moving on from single-particle simulations, a full PYTHIA simulation was made to check for reconstruction features in a *pp* scenario. To gain a full understanding of the reconstruction, we match the closest match particle produced from PYTHIA and also the next-closest (to study effects due to track merging). The matching resolution between the reconstruction and PYTHIA is 0.13 in $\delta\eta$ and 0.05 in $\delta\phi$, see Fig. 3.33.
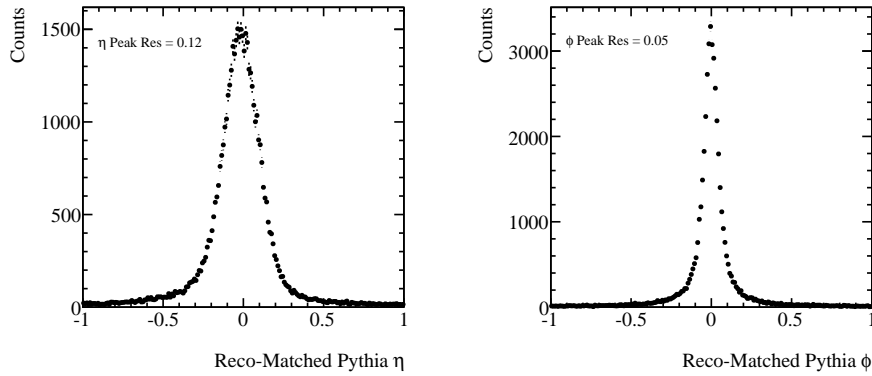
**Figure 3.33:** Resolution of matching between reconstructed and PYTHIA primary particles. The left panel shows the $\delta\eta$ resolution and the right shows the $\delta\phi$ resolution. The text states the Gaussian sigma of a fit to a region close to the peak, to exclude the outliers.

π^0 Reconstruction

The reconstruction of π^0s is critical in determining the direct-γ yields, as this is the largest contribution to the background. The reconstruction algorithms are well understood in single-particle events and are observed to find high-p_T π^0s. In PYTHIA, the addition of more particles, thus more energy in the MPC and preshower, could cause the algorithm to fail. This Section discusses this potential point of failure.

Figure 3.34 shows the reconstructed invariant mass in several bins of p_T; no quality-control cuts have been applied to the data – this is discussed later. In each panel, the black histogram shows the reconstructed data without knowing the origin of the particle which makes that track. Tracks which were created from π^0s are shown in red and, as expected, dominate the data. The legend in the figure denotes the fraction of all events in the given p_T bin. The first number is the fraction which passed all reconstruction cuts, but ignores the value determined for the invariant mass. The second number shows the fraction of that particular particle with a well-reconstructed invariant mass tracks (i.e. *Inv.Mass*>0). The final number shows the fraction of that particular particle which did not produce a well-reconstructed invariant mass. The numbers are summarized in Table 3.4. Further in the figure, more minor contributions to the total histogram are shown, specifically, η

and low-mass vector mesons contribute a significant fraction and are a further source of background to the direct-γs.
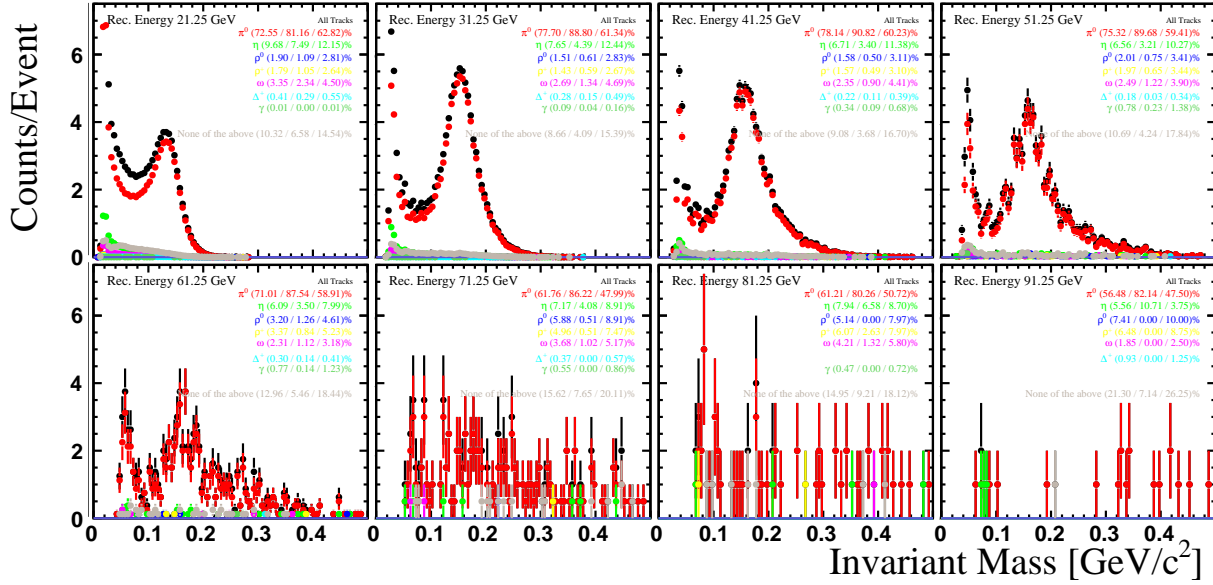
Figure 3.34: Reconstruction of all particles, showing the well reconstructed mass range. Numbers in the caption are: fraction of total / InvMass>0 / InvMass<0. different panels are energy dependence.

Figures 3.35 (linear scale) and 3.36 (logarithmic scale) show a summary of the data from Fig. 3.34 / Table 3.4. The left panels show the fraction of well reconstructed invariant mass data relative to the total number of tracks reconstructed. The right show the failed invariant mass. The data at high energy are statistics starved; additionally, there are no quality-control cuts applied. The fraction of γ events rises steadiily from low-to-high energy as the cross-section of the hadronic sources drops.
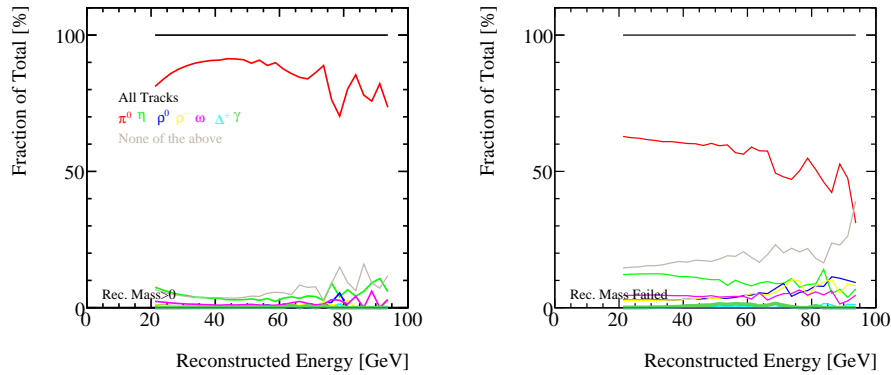
Figure 3.35: Energy dependence of fraction of each particle type, no cuts except fiducial cut. (Waiting for more data to process.)

Table 3.4: Breakdown by particle type of the contribution to the invariant mass spectrum. No cut refers to the all data (irrespective of whether the invariant mass was reconstructed or not. (<0) ≥ 0 are tracks with a (not) well reconstructed invariant mass. "–" denotes too low statistics to be reliable. No quality-control cuts are applied to this data.

| Energy GeV	Invariant Mass	π^0 %	η %	ρ^0 %	ρ^+ %	ω %	Δ^+ %	γ %	Something Else (%)
	No Cut	71.4	9.3	2.1	2.0	3.5	0.5	0.01	11.1
20-22.5	≥ 0	80.8	7.5	1.1	1.0	2.4	0.3	0.01	6.7
	<0	61.4	11.2	3.2	3.0	4.7	0.7	0.01	15.8
	No Cut	75.7	7.4	1.9	1.6	3.1	0.4	0.08	9.9
30-32.5	≥ 0	88.2	4.5	0.7	0.6	1.5	0.2	0.04	4.3
	<0	59.1	11.2	3.4	3.0	5.2	0.6	0.14	17.4
	No Cut	76.9	6.2	2.0	1.7	2.5	0.2	0.33	10.3
40-42.5	≥ 0	90.7	3.2	0.6	0.3	0.8	0.04	0.11	4.2
	<0	58.1	10.4	3.8	3.6	4.6	0.4	0.64	18.5
	No Cut	73.9	5.7	2.2	2.6	2.8	0.1	0.87	11.8
50-52.5	≥ 0	89.2	3.5	0.9	0.4	0.4	0.0	0.22	5.4
	<0	58.4	7.9	3.5	4.9	5.3	0.2	1.54	18.3
	No Cut	68.9	6.2	2.7	4.9	3.6	–	0.44	13.3
60-62.5	≥ 0	87.9	2.2	2.2	0.0	4.4	–	0.00	3.3
	<0	56.0	9.0	3.0	8.2	3.0	–	0.75	20.2
	No Cut	62.5	–	–	–	–	–	–	–
70-72.5	≥ 0	90.6	–	–	–	–	–	–	–
	<0	40.0	–	–	–	–	–	–	–
	No Cut	61.1	–	–	–	–	–	–	–
80-82.5	≥ 0	76.9	–	–	–	–	–	–	–
	<0	52.2	–	–	–	–	–	–	–
	No Cut	69.2	–	–	–	–	–	–	–
90-92.5	≥ 0	75.0	–	–	–	–	–	–	–
	<0	66.7	–	–	–	–	–	–	–

π^0 Reconstruction Failure

The main problem in the analysis of the π^0s is a physics property of the decay of the π^0. In the rest frame of the π^0, the decay angle is evenly distributed. As such, the energy of each daughter γ, when boosted into the collision rest frame, is not equally. In fact, it is unusual for an equal energy for each γ. This is not a particular problem for the two-track analyses, but for single tracks, where the distance between tracks is small, the lesser-energy track can be overwhelmed by it's counterpart. Overwhelmed to the degree that the signal is lost in the tails of the larger-energy γ. This can be illustrated by looking at the asymmetry of the decay versus the reconstructed invariant mass. Figure 3.37 shows this for the true decay asymmetry (left panel) and the estimated decay asymmetry based on the energy in
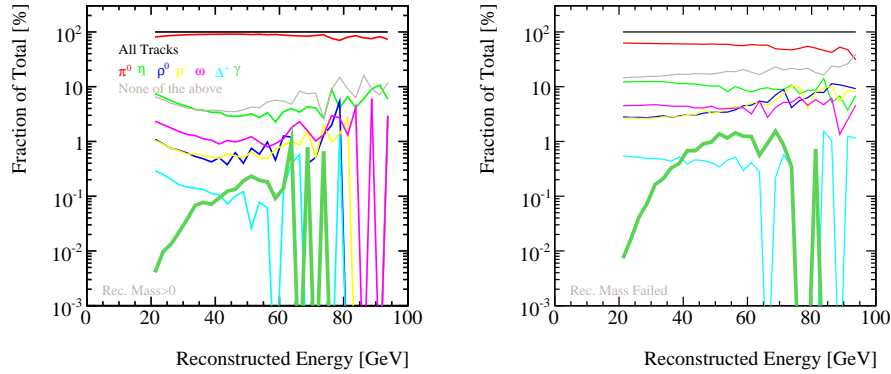
Figure 3.36: Same as Fig. 3.35, but logarithmic scale on the y-axis for detail.

the minipads associated to each track. For the true case, very asymmetric tracks mostly reconstruct as a 'single γ' at low invariant mass. For tracks with an asymmetry of 50% or less (zero is equally-shared energy), the mass is amost always well reconstructed. The estimated asymmetry from the reconstructed mini-pad energy associated to each γ does not reflect this. This is due to the small sampling fraction coupled with the optimization within the algorithm to separate the daughter *gamma*s.
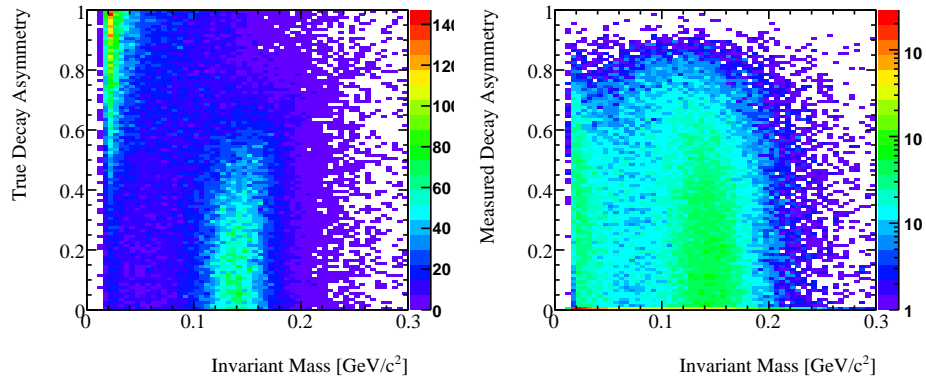
Figure 3.37: True (left) and measured (right) asymmetry versus the reconstructed invariant mass.

One can look at this in more detail with an energy dependence of the asymmetry, see Fig. 3.38. One finds that the fraction of mis-reconstructed mass is highest in the low-energy bins, whilst at higher energy, the mass becomes better defined, even for very asymmetry decays.
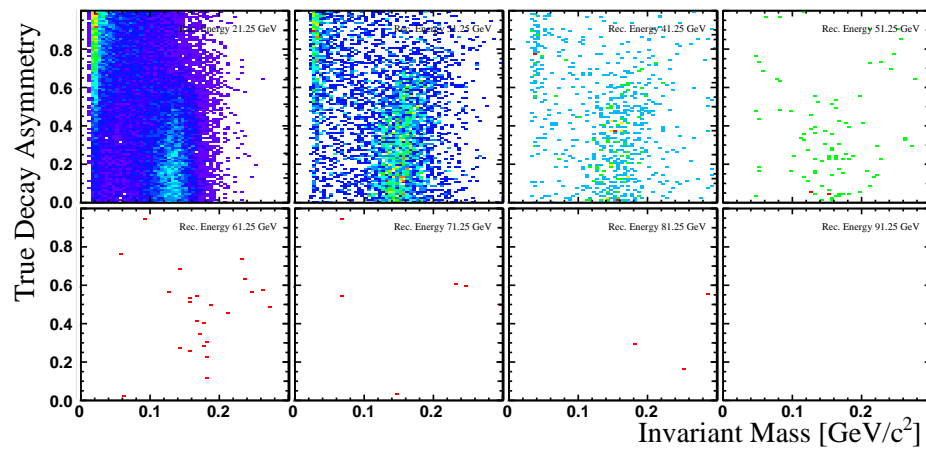
Figure 3.38: Energy dependence of true asymmetry vs inv mass. (Waiting for more data to process.)

3.2.6 Track Selection Cuts in Pythia events

3.2.7　Efficiencies from Pythia events

3.3   Direct Photons in d+Au Collisions

3.3.1   Simulation

The MPC-EX detector's ability to measure direct photons in d+Au collisions is determined using a minimum bias 200 GeV p+p Pythia simulation with a realistic vertex distribution. At transverse momenta above 3 GeV, where the direct photon measurement is performed, binary-scaled p+p events provide a good approximation of d+Au events. Of the approximately three-fourths of a billion simulated events, five million events contain a track with a combined MPC and MPC-EX energy above 20 GeV. The study of this subset is presented in this proposal.

The simulated events are reconstructed according to the procedure presented in Section 3. MPC-EX tracks are required to fall within the MPC-EX η acceptance ($3.1 > |\eta| > 3.8$), match to a unique MPC cluster, and have a MPC-to-MPC-EX hough separation below 0.005. The resulting tracks are well reconstructed and well matched to the MPC. Tracks are also matched to the pythia information. The reconstructed track and pythia separation in η-ϕ space is constrained to be less than one.

3.3.2   Photon Candidates

Charged hadrons[1] passing through the MPC-EX deposit a small amount of energy in each layer. They can be identified by requiring hits in each layer with small widths and energy deposited in a narrow region of interest. This is identical to the charged hadron identification used in Section 3.4. The energy asymmetery of the track is the ratio of the difference between the two track energies in the π^0 reconstruction divided by their sum, Equation 3.2.

$$asymmetry = \left| \frac{E_2 - E_1}{E_2 + E_1} \right| \qquad (3.2)$$

The asymmetry parameter ranges between zero and one with one being a highly asymmetric pair. Tracks that the fail the single track π^0 reconstruction, have a default asymmetry of zero. Charged hadrons and photons typically fail the single track π^0 reconstruction and so the majority of them have asymmetries of zero. Figure 3.39 presents the shape comparion of the asymmetry distributions for both photons and charged pions that did not fail the π^0 reconstruction. Tracks with asymmetries of less than 0.4 are kept.

Charged hadrons remain a signifigant background to the direct photon signal. A χ^2 cut comparing the shower widths and energies of charge hadrons and photons was considered but is currently too inefficient. This is most likely a result of the small amount of detector material and short depth of the MPC-EX detector making it difficult to distinguish between

---

[1]Neutral particles, such as neutrons, behave similarly and are removed in the same manor. The remaining neutral contribution is minimal.

Figure 3.39: A shape comparison of the asymmetry distribution for charged pions(green) and photons(orange).

the charged hadron and photon showers. Further tuning of the χ^2 variable may result in an improved charged hadron rejection. However, the benefit of an optimized the χ^2 cut may be limited.

An additional background track are the photons from hadronic decays. These tracks behave electro-magnetically in the MPC-EX and have a similar detector response. Photons from pion decays appear in the photon candidate mass spectrum as a peak at the pion mass with an additional low mass peak, as seen in Figure 3.40. The photons and charged hadrons mass distributions peak at the pion mass; this is most likely due to the single track π^0 reconstruction finding a neighboring shower that coincidentally is in the pion window.

Figure 3.40: The mass distribution of photon track candidates. All track candidates are in red, photons from hadronic decays are in pink, charged pions are in light green, neutrons are in blue, protons are in light blue, kaons are in dark green and non-hadronic photons are in grey.

The majority of photons and charged hadrons fail the single track π^0 reconstruction. These tracks are not visible in Figure **??** because their invariant masses are assigned negative values.

Photons from pion decays can be removed statistically using reference line shapes obtained from test beam data, simulations and real data. Currently these reference lines are not available and a separate simulation of the pion and direct photon line shapes has not yet been implemented.

With the current simulation we estimate the direct photon line shape by applying tight cuts requiring chi2 cut on the energy deposited (less than 1.65) and the shower widths (less than 1.7) and tight eta, phi and energy agreement between the reconstructed track and pythia, Figure. Because of the signal loss with these tight cuts we are unable to produce this line shape in each of the desired kinematic bins. Future work using a simulation dedicated to direct photon events will more acurately generate a direct photon line shape for all kinematic bins.

Photons from pion and eta decay may also be removed by pairing photon candidates within each event and removing tracks that can produce a pair with mass within 0.035 GeV of the pion and eta masses. This pair cut provides an lower limit on the MPC-EX's ability to remove photons from pion and eta decay.

Figure – mass distrib for tracks all eta, pt with line for those removed as pion pairs, line for remaining

Figure 3.41: The left panel shows the pair mass distribution for two photon candidate pairs. Single tracks that make pairs within a 0.035 GeV window of the pion and eta masses are removed from the photon candidate sample. The right panel shows the minimal effect this has on the single photon canidate mass spectrum. The unadjusted spectrum is shown in black, the spectrum of rejected tracks is in red, and the remaining spectrum is in blue.

Figure 3.41 shows the mass distribution for photon candidate pairs and Figure ??? shows the small effect this pair cut has on the photon candidate mass distribution. Table 3.5 shows the reduction in yields as a result of this cut. This cut has no effect on the relative contributions to the photon candidates. Widening the rejection region and relaxing of the requirements on the second track in the pair may improve the rejection but most likely the acceptance is not large enough to contain both of the photons from the hadronic decay.

Table 3.5: Photon candidate yields before and after pair-wise π^0 and η removal

Component	Before cut	after cut
Photon candidates	5498508	4987813
True photons	2688598	2422382
Hadronic photons	2420683	2179569
Non-hadronic photons	?	4796

3.3.3 Photon Candidate Sources

Using the pythia information we can identify the sources of the photon candidate tracks. Table 3.6 and Figures *EEP* show these. The sources are separated into the remaining Charged hadron contribution, hadronic photons and...

Table 3.6: Breakdown of direct photon candidates

Candidate Sources	all p_T, $3.1 < |\eta| < 3.8$	$p_T > 3$ GeV, $3.1 < |\eta| < 3.45$	$p_T > 3$ GeV, $3.45 < || < 3.8$	$p_T > 5$ GeV, $3.1 < |\eta| < 3.45$	$p_T > 5$ $3.45 < ||$
Charged hadrons	0	0	0	0	0
Hadronic photons	0	0	0	0	0
not direct	0	0	0	0	0
direct	0	0	0	0	0

Figure – mass distribs in eta, pt cuts

The d+Au direct photon spectrum measured in the MPC-EX detector provides access to nuclear structure functions at low x, as was presented in 1.1. The measured R_{dAu} may

constrain the EPS09 model for the gluon nuclear PDFs [23]. D Direct photon are simulated in rapidity bins and weighted according to the 31 PDFs in the EPS09 model[2].

The EPS09 model assumes a Glauber initial state. Including a PDF with a CGC initial state is also possible.

Estimations of the constraints on EPS09 using data from the MPC-EX require better a understanding of the systematic errors in the direct photon analysis, in particular the direct photon signal-to-background.

---

[2]These PDFs consist of a "best fit" result and functions from variations of the 15 model parameters.

3.4 π^0 Correlations in Jets

In this section we describe simulations to estimate the sensitivity of the MPC-EX detector to an asymmetry of neutral pions around a fragmenting quark in transversely polarized $p+p$ collisions. Our strategy is as follows. First, we describe a Monte Carlo model that was developed to include the effects of finite transversity and Collins fragmentation in the final state distribution of hadrons from a fragmenting quark. Using this model we generate a sample of events with roughly the same single-particle asymmetry A_N as that observed in neutral clusters in the PHENIX MPC, where the asymmetry is generated from the effects of transversity and Collins fragmentation. These events are put through a realistic simulation of the MPC-EX + MPC detectors, and are reconstructed and analyzed as physics data. The results of this exercise allows us to demonstrate the level of asymmetry due to transversity and Collins fragmentation that could be observed and make projections for a full event sample in real data.

3.4.1   The toyMC Monte Carlo Model

Simulations of the Collins asymmetry in jets in 200GeV $p+p$ collisions requires a model that can produce a sample of particles from parton fragmentation with the asymmetry built-in to the kinematic distributions. At the start of the simulations for the MPC-EX no such model existed that implemented the best information available from SIDIS experiments in an event generator format. The toyMC model was developed to address the need for just such an event generator.

The toyMC model starts with the event generator pythia (version 6.421) [34], configured only to perform the initial partonic event. All fragmentation of the partons is disabled. In addition, because we seek a leading-order model consistent with the SIDIS extractions we will use to implement transversity and the Collins fragmentation functions, all QED and QCD radiation from the parton legs is disabled. Pythia is run with the standard QCD 2x2 hard scattering processes enabled (process ID's 11,12,13,28,53,68 and 96) and we use TuneA pythia parameter set, as this has been shown to better produce the pion cross sections (albiet at lower rapidities). The cross section for all sampled processes is 22.3mb.

The spin of the incident protons are assigned randomly, and the spin of the scattered partons is set from the transversity distribution as parametrized in [11] and [12] at the scale of the hard interaction. Pions from quarks are generated according to the Collins fragmentations functions extracted from SIDIS and Belle data [12] and parametrized based on the DSS fragmentation functions (FF's), while pions from gluon fragmentation and all other particles are fragmented according to the spin-independent DSS FF's. The choice of favored/unfavored Collins FF's is made based on the fragmenting quark valence quark content of the hadron for charged pions, while it is assumed the the π^0 always fragments to pions according to the favored FF. The fragmentation functions are taken at the scale $\mu = p_T$ of the fragmenting parton. An example of the distribution of the Collins
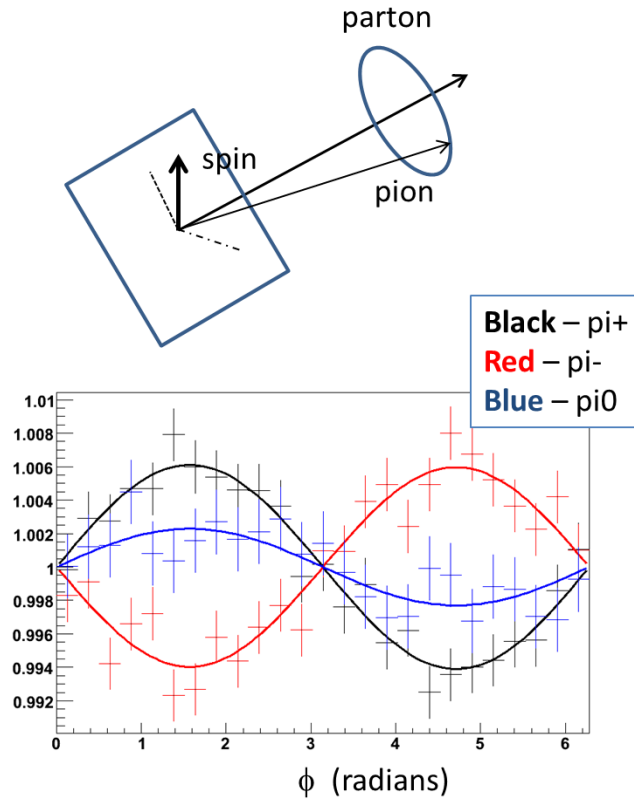
Figure 3.42: Sample toyMC distributions for pions, summed over all fragmenting quarks. The combination of transversity and the Collins FF's yields an asymmetry patern where the π^+ and π^- asymmetries are equal and opposite, and the π^0 asymmetry is the same sign as the π^+ asymmtery, although somewhat reduced. Note that the actual value of the asymmetries depends on the kinematic cuts and model parameters.

asymmetry as implemented in the toyMC model is shown in Figure 3.42.

The toyMC model also implements the Sivers distributions as a set of event weights which can also be used to generate asymmetries for the final state particles. Because these are not relevant to the MPC-EX analysis they will not be discussed further here.

In order to benchmark the model and tune the asymmtries it generated for MPC-EX studies, we compare the single-particle A_N for π^0 mesons in the MPC under various conditions in Figure 3.43. It should be noted that using the standard parametrizations for transversity and the Collins FF's yields a vanishingly small asymmtery at large x_F in 200GeV $p+p$ collisions. This may in part be due to the fact that the transversity distribution above x_F 0.3 is an extrapolation of the functional fit form and is not constrained by SIDIS data. Pushing transversity to the Soffer bound yields toyMC asymmetries that are similar to those observed in PHENIX (see Figure 3.44).

Figure 3.43: A_N single spin asymmetries (single particle) for π^0 in the acceptance of the PHENIX MPC under various tunings of the toyMC model.

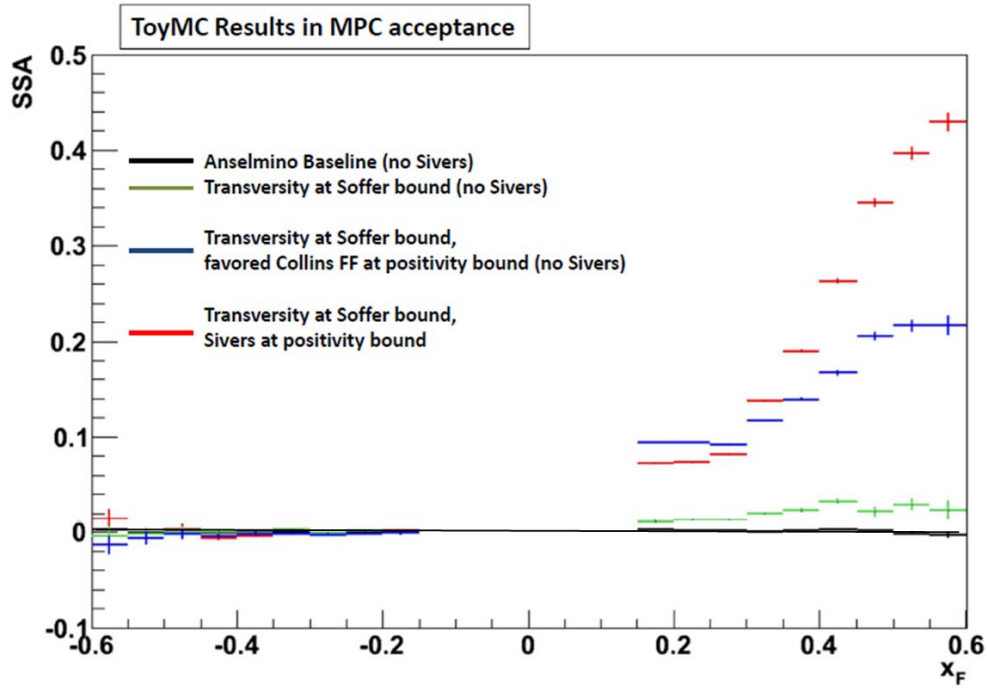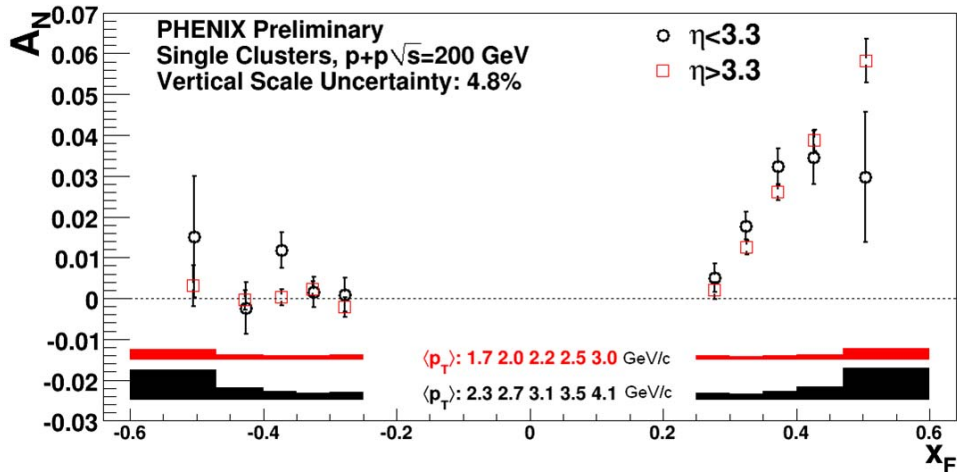
Figure 3.44: PHENIX preliminary results for the A_N single spin asymmetries (single particle) for neutral clusters in the acceptance of the MPC.

3.4.2 Event Generation and Statistics

Two large samples of toyMC events were generated to simulate the extraction of the Collins asymmetry in the MPC-EX. The first sample of 4.9M events was generated with transversity set to the Soffer bound and the Collins FF's set to the positivity limit. This set of events was used to examine the asymmetry for small systematic effects, such as an angular correlation between the extracted jet axis and the axis of the fragmenting parton. A second, larger set of 19.5M events was generated with transversity at the Soffer bound in order to match the single particle A_N observed in PHENIX. This sample is the main sample used to test the sensitivity of the MPC-EX analysis to the Collins asymmetry. In both samples an event was written out from the Monte Carlo only if there was a π^0 and at least one charged particle in the acceptance of the MPC-EX. The small event sample corresponds to a sample luminosity of $0.10pb^{-1}$, while the large sample corresponds to $0.41pb^{-1}$.

In both cases the event vertex along the beamline was chosen according to a Gaussian distribution matched to the real distrbution of events in 200GeV $p+p$ collisions. In the final analysis only events with a vertex between ± 70 centimeters were used.

The output of the toyMC event generator was then put through the GEANT3-based PHENIX Integrated Simulation Application (PISA) in order to simulate the response of the MPC-EX, MPC and BBC detectors to the event, and the PHENIX reconstruction and analysis framework was used to turn the simulated hits into raw data quantities in a simulated DST. These DSTs were then analyzed to produce physics quantities.

3.4.3 Charged Particle Reconstruction

Charged particles in the MPC-EX are reconstructed via a loose set of cuts. A charged particle is identified in the MPC-EX by demanding that the MPC-EX track have a hit in all eight layers, and that the energy within a narrow window around the tracks (+/-10 strips centered on the track) is less than 70MeV (see Figure 3.45. No check on the association of the MPC-EX track to a cluster in the MPC. A more restrictive cut was also explored that required that the RMS of the distribution of hits in each later be less than one strip, but the addition of this cut reduces the track finding efficiency and does not significantly reduce backgrounds.

3.4.4 π^0 Reconstruction

In jet events, reconstruction of π^0 mesons is done by single-track reconstruction for tracks with a total energy > 20GeV, and by two-track combinations for tracks with energies < 20GeV. The reconstruction method is described in section 3.1. Electromagnetic tracks are only required to have an associated MPC cluster and be flagged as the "closest" track
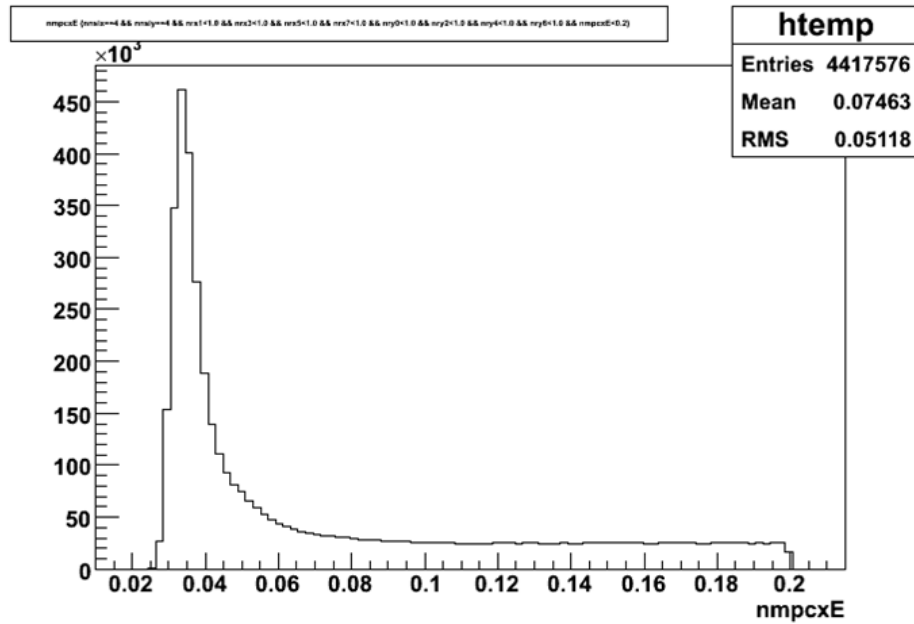
Figure 3.45: Energy distribution of MPC-EX tracks that hit all eight layers in the preshower in toyMC jet events. The MIP peak at 36MeV is clearly visible. In the analysis a cut is placed at 70MeV to select charged particle tracks.
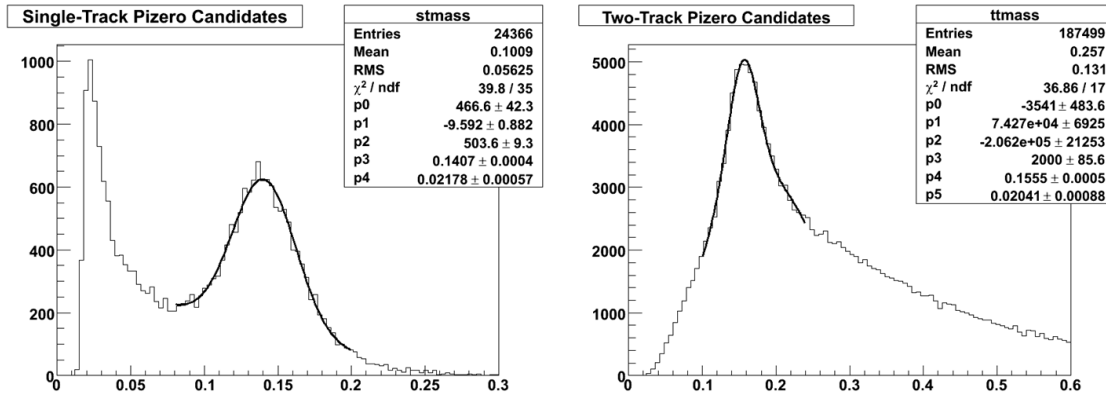
Figure 3.46: Invariant mass distributions for single-track (left) and two-track (right) π^0 reconstruction in toyMC jet events. The single-track π^0 distribution has less background, but lower statistics.

in hough space. In addition, an electromagnetic track must not pass the charged particle cuts described above. This eliminates charged tracks that pass through the MPC-EX and shower in the MPC.

Figure 3.46 shows the resulting invariant mass distributions for single-track and two-track π^0's in toyMC jet events. In general the single-track π^0 distribution has less background,
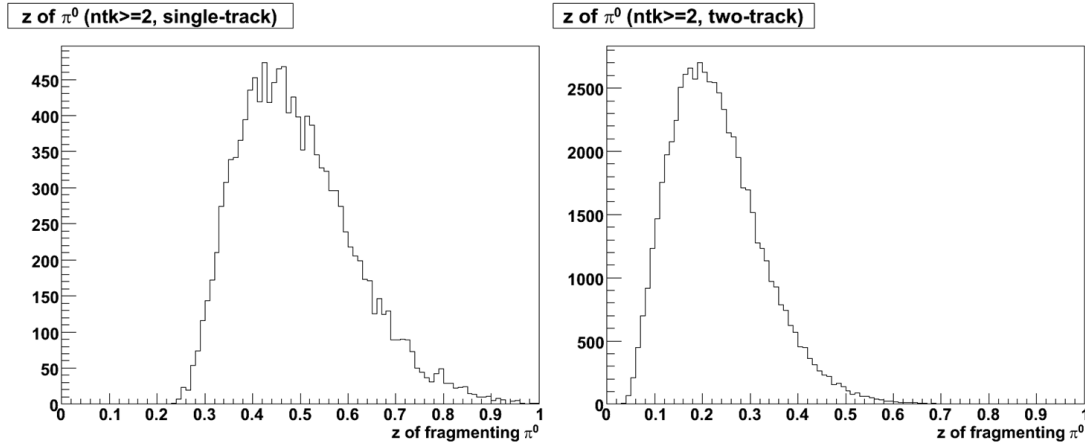
Figure 3.47: Distribution of fragmentation z for single-track (left) and two-track (right) π^0 reconstruction. The sample of events chosen were events with two tracks found making up a charged cluster, with the π^0 on the same side as the cluster in azimuthal angle.

particularly under the π^0 mass peak. Candidate π^0 mesons for correlations are selected by a 2.5σ mass cut in the reconstrcution, $0.105 < m < 0.205 GeV$ for two-track π^0's and $0.085 < m < 0.195 GeV$ for the single-track reconstruction.

Because the two-track and single-track π^0's are reconstructed in different energy ranges they sample different kinematics. In particular, the fragmentation $z = \frac{p_{\pi 0}}{p_{jet}}$ is higher for the single-track π^0's, as shown in Figure 3.47. Because the Collins fragmentation function extracted from SIDIS measurements and used in toyMC is a strong function of the fragmentation z, the single-track pizero sample will have a larger asymmetry. Conversely, measuring the two-track and single-track pizero samples would allow some experimental sensitivity to the z dependence of the Collins fragmentation function and would provide a greater constraint to theoretical models.

3.4.5 Jet Cluster Reconstruction

Jet cluster reconstruction proceeds by sorting MPC-EX tracks into charged track and electromagnetic track lists. For electromagntic tracks the total, calibrated energy deposited in the MPC-EX and MPC are used to define the track's momentum. However, we have no momentum measurement for charged tracks, so all charged tracks are arbitrarily assigned an equal momentum of 1GeV. The same jet cluster reconstruction is applied to both charged and EM tracks independently, but charged tracks and electromagnetic tracks are not combined in this analysis.

The jet cluster algorithm is a seeded cone algorithm that uses every particle in the track list as seed for a cluster cone. The cluster cone is take as a fixed radius in η and ϕ space of 1.0 units for both electromagnetic and charged track clusters. For each selection of a
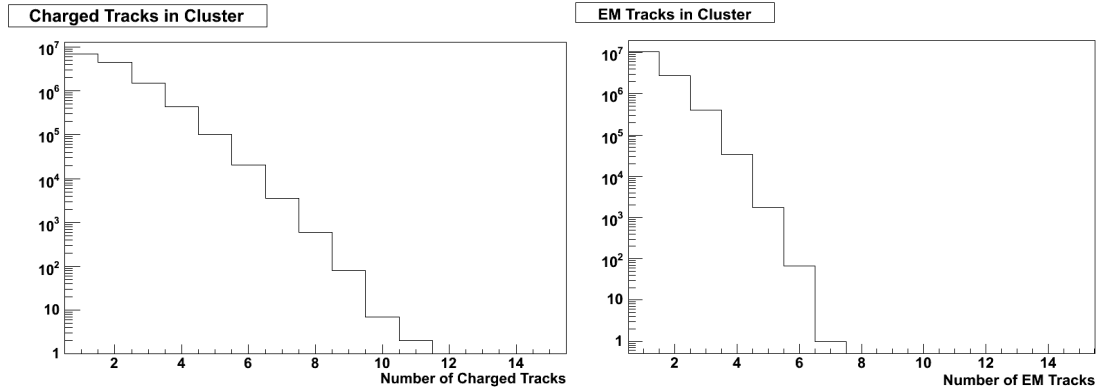
Figure 3.48: Distribution of number of tracks found in the highest p_T cluster in a sample of toyMC jet events, for both charged jet clusters (left) and electromagnetic jet clusters (right).

seed track, the cone algorithm and cluster axis are iterated until further iteration produces no change in the cluster axis. Finally, the cluster that resulted in the highest transverse momentum is selected. It should be noted that in principle we could be less sensitive to backgrounds from gluon jets by reducing the cone radius, but this has not been explored in this analsysis.

In the analysis of jet cluster + π^0 correlations that follows, we require the jet cluster be comprised of two or more, or three or more particles, effectively making a three-particle or four-particle requirement for the jet when the π^0 requirement is added. For a complete dataset of real collisions the asymmetries obtained could be examined as a number of the particles required in the cluster in order to study systematic effects and improve signal-to-background, but that is not possible with the limited statistics available in simulation.

3.4.6   Simulated Asymmetries

In this section we describe the simulated asymmetries based on the large statistics dataset, with single-particle A_N asymmetries that are comparable to those observed in the MPC. The goal of this exercise is to benchmark the sensitivity of this analysis in terms of the minimum asymmetry that should be visible at a given integrated luminosity.

Charged Cluster - π^0 Correlations

The low asymmetry toyMC event sample is used to gauge the size of the asymmetry expected as well as the total available statistics given the simulated luminosity. Correlations are examined individually for both the single-track and two-track pizero samples. This statistical power in the Monte Carlo sample allows us to make meaningful correlations with charged particle jet clusters that have $>= 2$ or $>= 3$ charged partciles in the cluster.

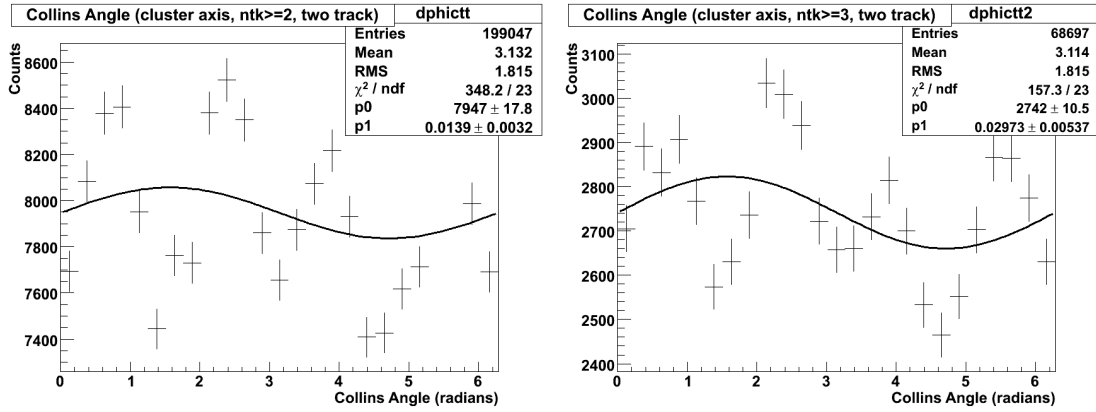**Figure 3.49:** Collins angle asymmetries for two-track π^0's correlated with charged clusters consisting of two or more particles in a charged cluster (left) and three or more particles. The shape of the distributions shows an acceptance effect that has not been accounted for.

Charged cluster - π^0 correlations is obtained by selecting events with a charged cluster and a reconstructed π^0 within $\pm\pi/2$ in azimuthal angle. The Collins correlation angle ϕ is calculated and binned, and the result can be fit to extract the spin asymmetry.

As anticipated, the asymmetries are small in the two track sample. In fact, they are small enough that acceptance corrections at the level of 1% are required to be able to reliably extract the asymmetries (see Figure 3.49). This can be demonstrated by dividing the asymmetry distributions by a distribution generated by using the same events but with a random spin orientation, thus cancelling any spin-dependent effects and leaving only acceptance effects (see Figure 3.51). Figure 3.51 shows the result of this exercise, and a small Collins asymmetry is visible after the correction is made. We note that dividing the spin-dependent by the spin-randomized distributions in this way does artificially inflate the error bars on each point because the two samples are not independent. However, a small but sigificant spin-dependent asymmetry is still visible.

Figure 3.52 shows the single-track π^0 asymmetries extracted from the low-asymmetry toyMC sample for π^0's correlated with different charged cluster samples. As with the two-track correlations, the spin-dependent distributions are divided by the spin-randomized distributions to eliminate acceptance effects. In the first sample two or more charged tracks are required to determine the charged cluster, while three or more are requred in the second sample. As expected, the extracted asymmetries are larger for the single-track correlations.

The Monte Carlo samples allow us to estimate how many pairs will be obtained in a given sample of integrated luminosity as well as the magnitude of the anticipated asymmetry. The statistics in each bin in Collins correlation angle can be scaled to the total sampled luminosity of $49pb^{-1}$. These numbers then provide the basis for the statistical error in each bin. We assume a 60% beam polarization, and scale the anticipated asymmetry down by

Figure 3.50: Collins angle asymmetries for two-track π^0's correlated with charged clusters consisting of two or more particles in a charged cluster (left) and three or more particles (right). The spin asymmetry in these distributions is destroyed by randomizing the spins, leaving only acceptance effects.
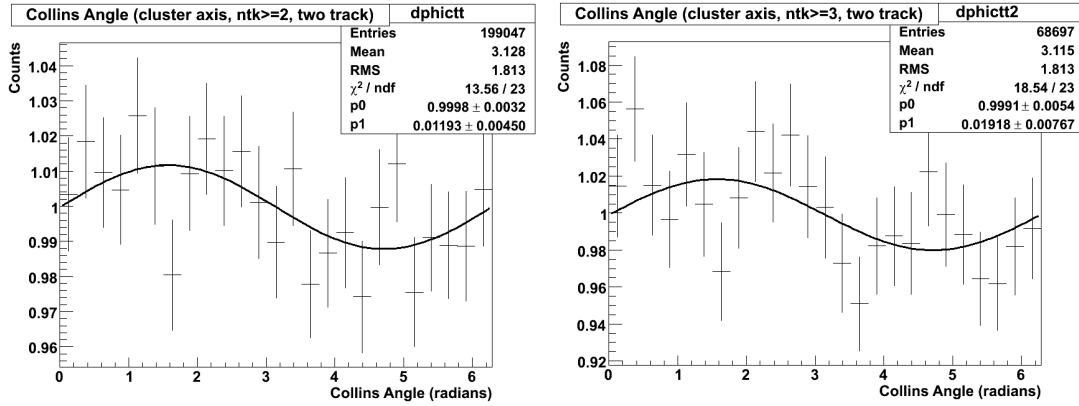
Figure 3.51: Correction of the acceptance effect in the two-track correlation sample after division by the spin-randomized distribution. Note that this process artificially inflates the error bars in the distribution because the two samples are correlated. A small Collins asymmtery is clearly visible after the correction. The correlation with charged track clusters containing two or more charged particles is shown on the left, and with three or more charged particles on the right.

0.6 to account for the imperfect beam polarization.

We show example asymmetries for two event selections. In Figure **??** we show the antipated asymmetry and statistical errors using two-track π^0's correlated with a jet axis determined using three or more charged tracks. In Figure 3.54 we show the antipated asymmetry and statistical errors using single-track π^0's correlated with a jet axis determined using three or more charged tracks. In both cases the anticipated statistical power is more than adequate to measure the expected asymmetries if the single particle A_N is
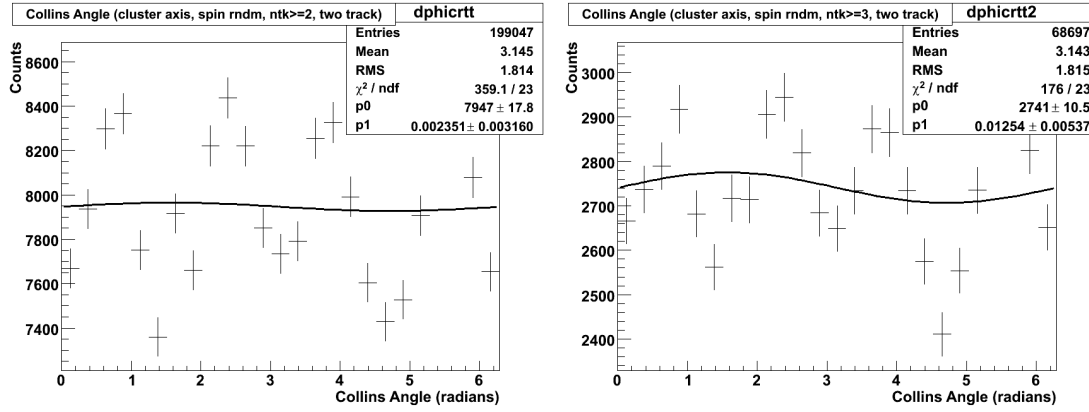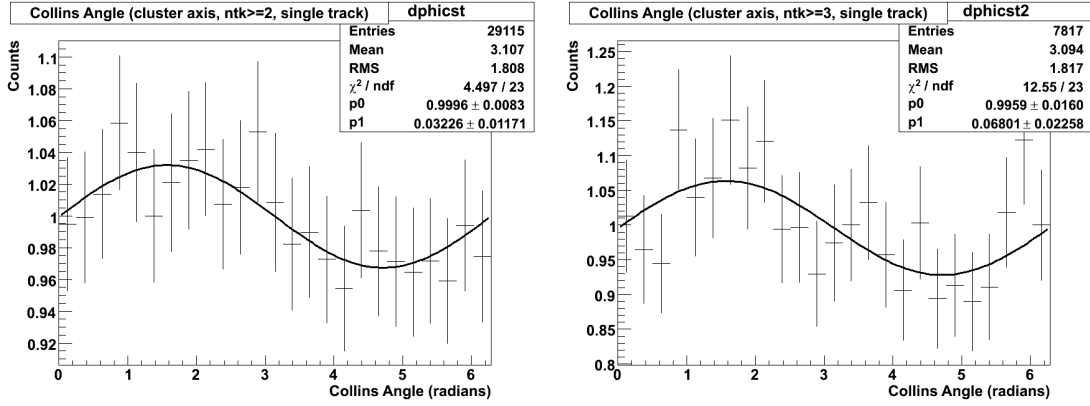
Figure 3.52: Collins angle asymmetries for single-track π^0's correlated with charged clusters consisting of two or more particles in a charged cluster (left) and three or more particles (right).
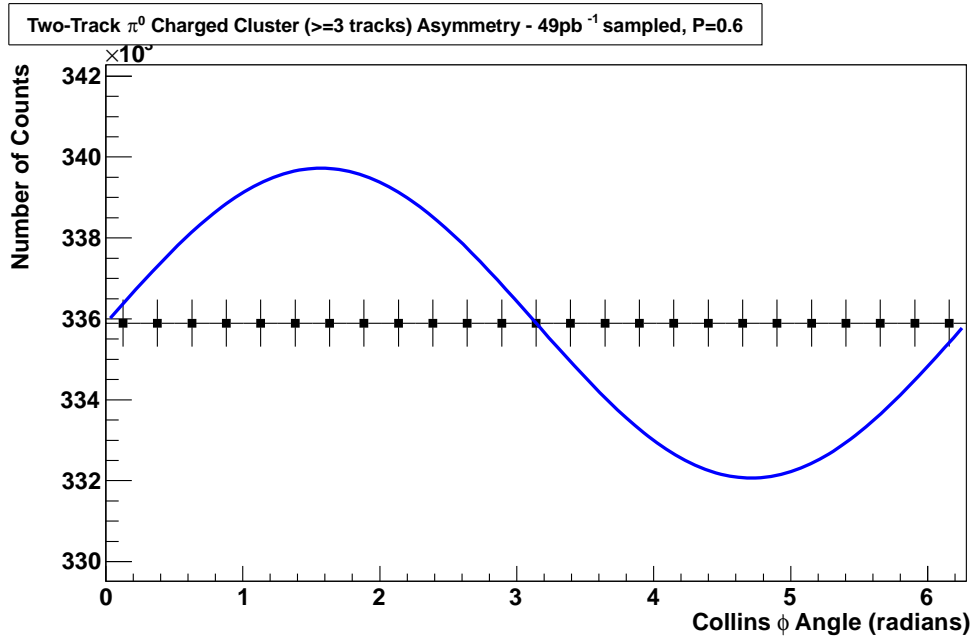
Figure 3.53: Anticipated statistics as a function of Collins angle for $49pb^{-1}$ sampled luminosity and average polarization of 60% using two-track π^0's correlated with a jet axis determined by three or more charged particles. The blue curve is the anticipated asymmetry for the data sample from the Monte Carlo, corrected for the beam polarization of 60%.

due to transversity and Collins fragmentation alone.

The minumum asymmetry that can be observed is set by the ability to ascertain if more π^0's go "left" with respect to the direction set by the spin axis and fragmenting parton, as opposed to "right". To estimate the smallest asymmetry that could be observed we make

Single-Track π^0 Charged Cluster (>=3 tracks) Asymmetry - 49pb^{-1} sampled, P=0.6
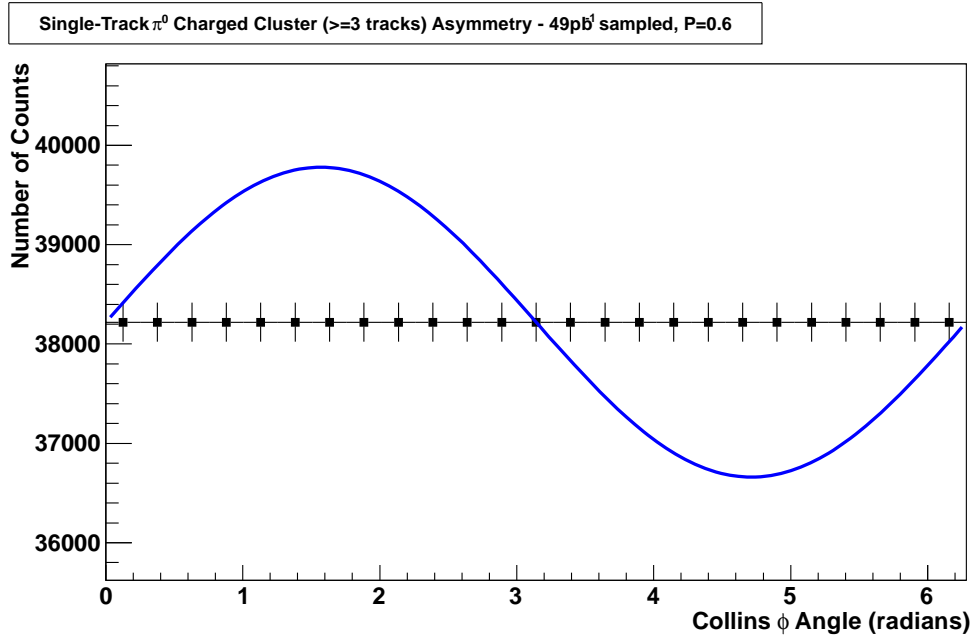
Figure 3.54: Anticipated statistics as a function of Collins angle for $49pb^{-1}$ sampled luminosity and average polarization of 60% using single-track π^{0}'s correlated with a jet axis determined by three or more charged particles. The blue curve is the anticipated asymmetry for the data sample from the Monte Carlo, corrected for the beam polarization of 60%.

maximum use of the statistical power of the data by dividing it into left and right, spin up and spin down samples, and calculating the asymmetry using the square root formula:

$$A_N^{raw} = \frac{\sqrt{N_L^\uparrow N_R^\downarrow} - \sqrt{N_L^\downarrow N_R^\uparrow}}{\sqrt{N_L^\uparrow N_R^\downarrow} + \sqrt{N_L^\downarrow N_R^\uparrow}} \tag{3.3}$$

Based on the assumed statistics and error propagation of the above formula, we can estimate the statistical error on the raw asymmetry A_N^{raw} for each event selection. For Table 3.7 this analysis should be sensitive to a raw asymmetry down to one-seventh of the expected asymmetry, at the level of 3σ. This means that this analysis will be capable of measuring a Collins asymmtery even if it is only responsible for as little as 14% of the overall single particle π^0 A_N in the two-track correlations, and 12% in in the single-track correlations.

Electromagnetic Cluster - π^0 Correlations

As noted above, we also reconstruct clusters of electromagnetic tracks in this analysis. While electromagnetic clusters have the added benefit of yielding energy information, they

Table 3.7: Three-sigma statistical errors assuming $49pb^{-1}$ and 60% polarization for two events samples.

Event Selection	Raw Asymmetry P = 0.6	3-σ statistical error on A_N^{raw}
two-track π^0, $>=$ 3 tracks in charged cluster	0.011	0.0017
single-track π^0, $>=$ 3 tracks in charged cluster	0.041	0.005
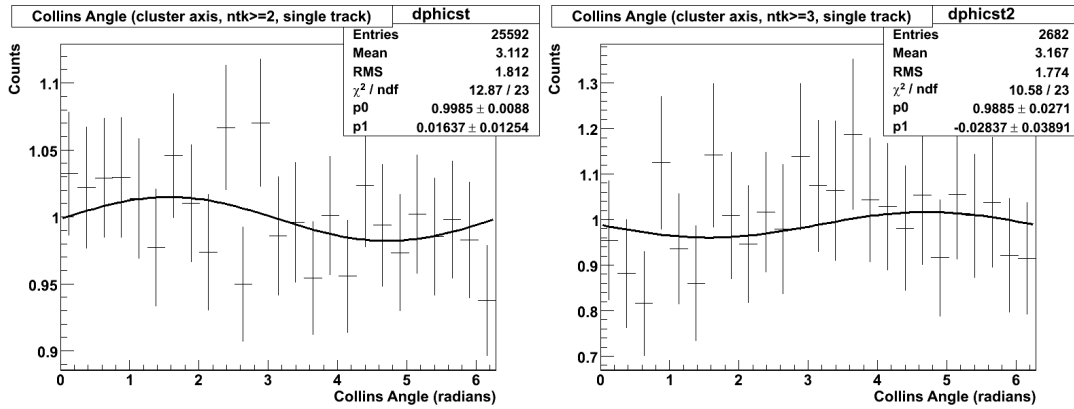
Figure 3.55: Collins angle asymmetries for single-track π^0's correlated with electromagnetic clusters consisting of two or more electromagnetic tracks (left) and three or more electromagnetic tracks (right). The asymmtery is dramatically reduced compared to the charged cluster correlations, see Figure 3.52.

are not appropriate for the determination of a Collins asymmetry through the correlation with π^0 mesons. The reason for this is simple - clusters determined with electromagnetic particles will contain the correlation that we are trying to measure, because most of the electromagnetic energy will come from π^0's. This effect will become worse for higher momentum π^0's because the cluster axis determination will be dominated by the π^0. In this case the correlation is increasingly like correlating the π^0 with itself.

To demonstrate this effect, we show the correlations between π^0 mesons and an electromagnetic jet axis determined with three or more electromagnetic tracks in the MPC-EX in Figure 3.55. The asymmetries when correlating with an electromagnetic axis are essentially zero within errors.

Jet Axis Resolution and Asymmetries

Using the Monte Carlo knowledge of the fragmenting parton axis in toyMC, we can determine the angular resolution of the cluster axis via the seeded cone algorithm. The
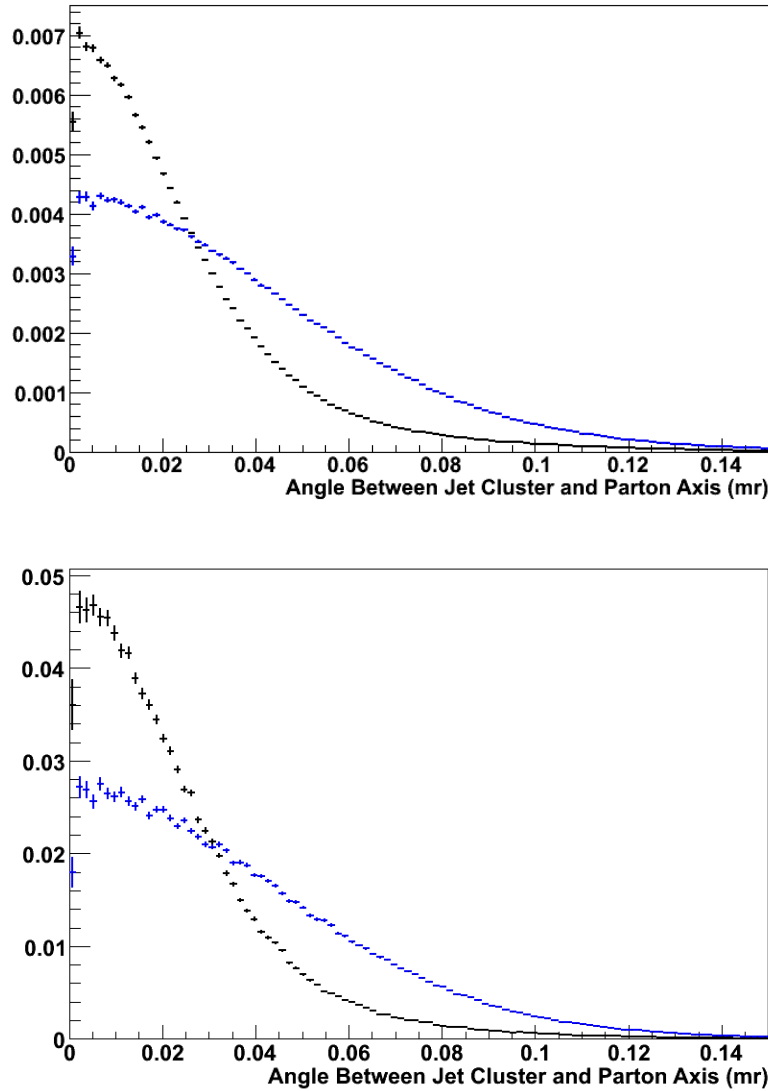
Figure 3.56: Distribution of the angle between the fragmenting parton axis and the resulting charged particle cluster, for clusters with two or more tracks (top) and three or more tracks (bottom) and jets with energies between 30 and 40GeV. The black curve is for the standard reconstruction, and the blue curve shows the result of artificially smearing the charged cluster axis by a Gaussian distribution with $\sigma = 34$mr. Both distributions are normalized to unit area in each plot.

resolution function is not Gaussian, but is best described as a Gaussian component with a long exponential tail. The toyMC model incorporates a simple, leading order model of independent fragmentation, and does not include gluon radiation and three-jet effects. In Figure 3.56 we show the angular resolution of the parton axis as determined by the charged cluster axis for a sample of jets with energies between 30 and 40GeV.
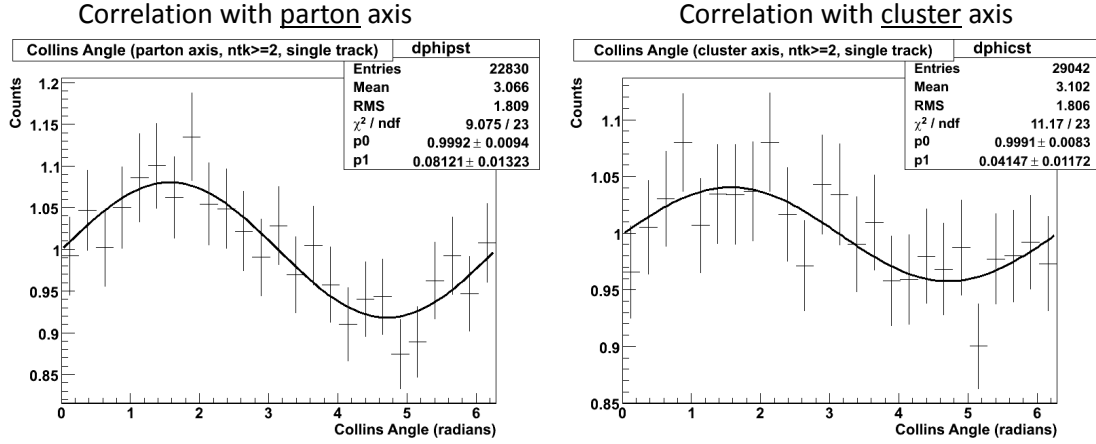
Figure 3.57: Angular correlations of π^0 mesons with respect to the true parton axis compared to the charged cluster axis, for clusters with two or more charged tracks. The charged cluster axis resolution dilutes the asymmetry by more than a factor of two. It should be noted that the correlations with the parton axis are still diluted by backgrounds and other effects.
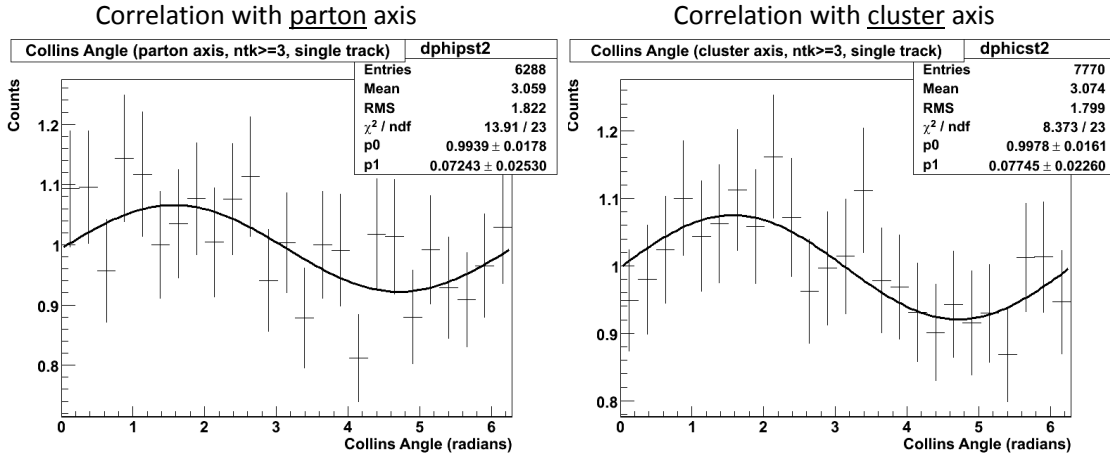
Figure 3.58: Angular correlations of π^0 mesons with respect to the true parton axis compared to the charged cluster axis, for clusters with three or more charged tracks.

The effect of the jet axis resolution can be observed in the Monte Carlo by comparing cluster correlations with correlations to the true parton axis, as shown in Figure 3.57 and Figure 3.58. Determination of the jet axis with charged clusters containing two or more charged tracks dilutes the observed asymmetry by more than a factor of two, although the statistical errors are large. With the requirement of three or more charged tracks the two asymmtries are the same within statistical error.

In order to investigate the effect of an overly optimistic fragmentation model we reconstruct the same events, but this time we artificially smear the charged cluster axis assuming a Gaussian distribution with $\sigma = 34$mr (see Figure 3.56). This does result in a small
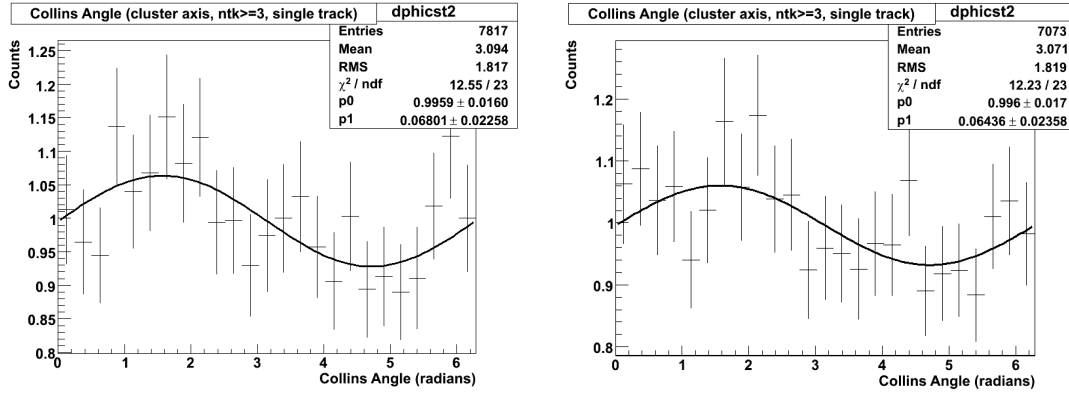
Figure 3.59: Angular correlations of single-track π^0 mesons for clusters with three or more charged tracks. The plot on the left shows the correlations with the standard reconstruction, and on the right for the same events the charged particle axis is further smeared using a Gaussian distribution with $\sigma = 34$mr. There is a small reduction in the asymmetry as the jet axis is smeared further.

reduction in the measured asymmetry when the same sample of events is compared with and without the additional jet axis smearing (see Figure 3.59).

When charged particles (mostly π^+ and π^-) are used to reconstruct the jet direction it is possible that the asymmetries that these particles carry could bias the jet axis and either dilute or induce an asymmetry when correlated with π^0's. However, any potential effect should be limited by the fact that the charged pions carry a roughly equal and opposite asymmetry, so that in the limit that a larger number of particles are used in the charged cluster any systematic effect should vanish.

This effect is too small to observe in the small asymmetry sample of events, but in Figure 3.60 we show the charged cluster asymmetry with respect to the jet axis for the large asymmetry sample of events. The large asymmetry sample enhances the effect, but it can be seen to diminish as a function of the number of charged particles required in the charged cluster. Studying the measured π^0 asymmetries as a function of the number of tracks in the charged cluster will provide a way to constrain any potential systematic error.

3.4.7 Effect of the Underlying Event

The previously described toyMC simulations included only the particles from jet fragmentation, and not additional particles from the underlying event (breakup of the target and projectile protons). In order to estimate this affect, a small sample of approximately 300k toyMC events were generated where the final jet particles were merged with an independent pythia minimum bias event. These merged events were reconstructed following the same procedure as the jet events, and the resulting asymmetries compared.
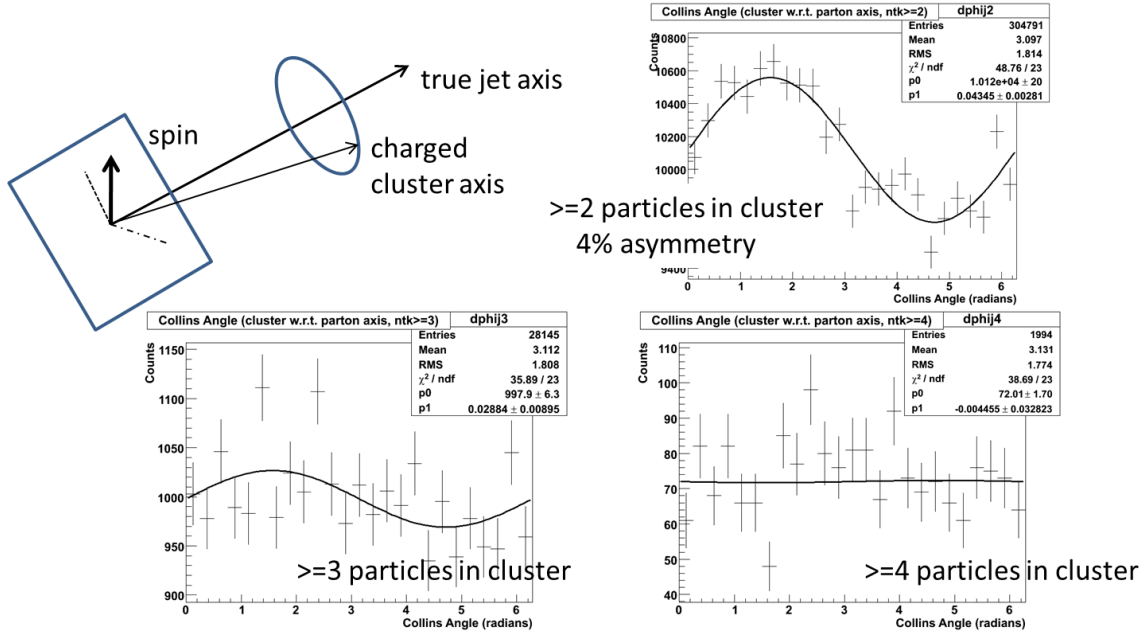
Figure 3.60: Asymmetry of the reconstructed charge cluster axis with respect to the parton axis for the large asymmetry sample of events. As a comparison the single particle A_N is 20% in these events, substantially larger than the observed A_N, which magnifies the asymmetry of the charged cluster axis. This effect essentially disappears when three or more charged particles are required in the jet determination.

Because of the lower statistics, a detailed comparison between the jet + minbias events and the low-asymmetry jet sample is not possible. However, we do not that even with the low statistics an significant asymmetry is still visible in the correlations. This gives us confidence that the presence of the underlying event does not destroy the correlations observed in the pure jet events.
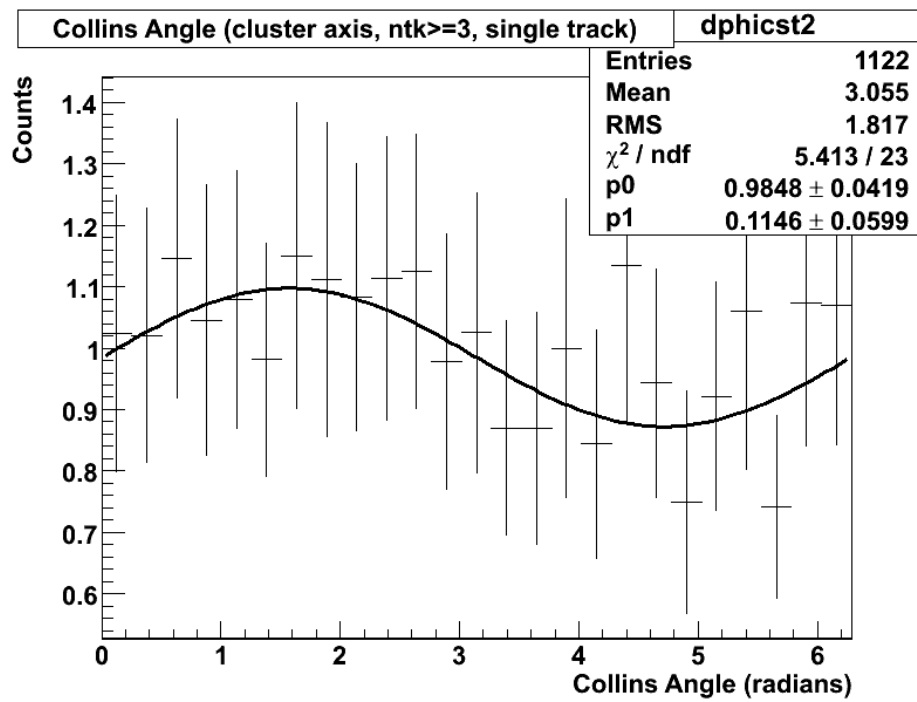
Figure 3.61: Angular correlations of π^0 mesons for clusters with three or more charged tracks in events where a toyMC jet event is merged with a pythia minbias event. While the statistics are lower due to the smaller number of these events generated, a clear asymmetry is still visible.

Chapter 4

Budget

At the present time the budget for the MPC-EX has been developed as fully as possible using known or quoted sources for item costs. It should be emphasized again that the design of the MPC-EX is intended to be truly "modular" in its construction, with mass-produced parts requiring only simple assembly.

The overall budget for the MPC-EX construction is summarized in Figure 4.1. The total cost is estimated to be $853k, with contingency at the 20% level and BNL overhead on purchases and labor fully accounted for. The cost estimates are based either on items purchased and/or built for the prototype detector and sensors, or quotes from the sources that are expected to supply the items. A detailed breakdown of the estimates for the main items follows in the next subsections.

4.0.8   Minipad Sensors

The base cost estimate for the MPC-EX silicon sensors is detailed in Figure 4.2, and was based on discussions with our collaborator at Yonsei University and the Korean foundries ETRI and nanoFAB. The discount levels used for the sensor processing apply to total order costs above $200K, yielding a 60% discount. The yield for sensor production was assumed to be 70%. In addition to the overall 20% contingency that is used for all items, we assumed an additional contingency of 15% to account for currency fluctuations between US dollars and Korean won.

4.0.9   Minipad Module Components and Assembly

Minipad module assembly will consist of attaching a minipad sensor module to a Minipad Readout Card (MRC). Fabrication, assembly and components for the MRC are listed, including one-time setup charges. Wire bonding the minipad sensor to the MRC and

MPC-EX Budget - 9/19/2011 - Total Cost for North and South Arms

Item	Quantity	NRE	Unit Cost	Base Cost	Contingency	Total	Overhead
Silicon sensors							
Strip silicon	384 + 40 spares			$151,846	15% + 20%	$209,547	
Minipad Module Components and Assembly							
Minipad Readout Cards (MRC)	424						
Fabrication		$500	$80	$34,420	20%	$41,304	
Assembly		$500	$80	$34,420	20%	$41,304	
Components			$20	$8,480	20%	$10,176	
Wire bonding and SVX4 attachment		$892	$67	$29,300	20%	$35,160	
Encapsulation			$7	$3,044	20%	$3,653	
Packaging			$8	$3,392	20%	$4,070	
Ceramic spacers			$5	$2,120	20%	$2,544	
Ground foils			$2	$848	20%	$1,018	
Tungsten							
Tungsten plates				$5,530	20%	$6,636	
Readout Electronics							
Carrier Boards (32 + 3 spares)	35						
Fabrication		$300	$400	$14,300	20%	$17,160	
Assembly		$300	$150	$5,550	20%	$6,660	
Components							
Minipad FEM cards (16 + 2 spares)	18						
Fabrication		$300	$200	$3,900	20%	$4,680	
Assembly		$300	$150	$3,000	20%	$3,600	
Components			$200	$3,600	20%	$4,320	
SVX4 Production (MOSIS + TSMC)							
SVX4.2b Production Masks		$150,000		$150,000	20%	$180,000	
SVX4.2b Production Run (12 wafers)		$50,000		$50,000	20%	$60,000	
Slow Controls							
Bias HV (16 + 1 spare)	17		$500	$8,500	20%	$10,200	
SC interface cards (4 + 1 spare)	5		$1,000	$5,000	20%	$6,000	
Support structures							
Support structures M & S				$10,000	20%	$12,000	
							Overhead 18%
Total M & S				$517,250		$660,033	$778,839
Labor							
Assembly Labor				$15,000	20%	$18,000	
Support structures & Installation Labor				$29,788	20%	$35,746	
							Overhead 39%
Total Labor						$53,746	$74,706
TOTAL MPC-EX							**$853,545**

Figure 4.1: Summary of the MPC-EX budget for both north and south arm detectors.

attaching the SVX4's will be done by Quik-Pak (San Diego, California, a division of Delphon Industries) and costs listed are based on the costs for the assembly of the strip modules used in the prototype detector.

4.0.10 Tungsten

The estimate for the tungsten plates is based on a quote from ATI Firth Sterling, one of the vendors that supplied quotes for the prototype and that BNL has a good experience with. The quote includes the cost of machining to the specifications that were provided in the form of drawings to the vendor. It includes plates for 24 towers in each arm, with 8 layers of 2mm tungsten. The contingency in this case reflects possible variations in the raw material market price.

MINIPAD SENSORS		min for discount	discount	discounted unit price			
						number of towers:	48
Number of sensors / tower	8					total sensors:	384
Spares needed	10%					spares needed:	38
						finished sensors needed:	422
Yield	70%						
						raw sensors needed:	604
Sensors per wafer	2						
						wafers needed	302
Cost per wafer	$100					total wafer cost:	$30,200
Packaging cost per sensor	$50					total packaging cost:	$30,200
Production cost per sensor	$378.50						
		0	1	$378.50			$228,614
		$50,000	0.5	$189.25			$114,307
		$200,000	0.4	$151.40		total production cost:	$91,446
		$500,000	0.3	$113.55			$68,584
						total cost:	$151,846
Currency contingency			15%			+ currency contingency	$174,622
Contingency			20%			+ contingency:	$209,547

Figure 4.2: Minipad sensors cost breakdown. The base cost of sensor production exceeds $200K, which yields a 60% volume discount.

4.0.11 Readout Electronics

The estimates for the readout electronics were compiled from price quotes and experience with the prototype detector. Each layer will require two carrier boards (top and bottom) and high gain and low gain readout will be through a separate minipad FEM cards. Each FEM card will read on readout channel from four carrier boards. The costs listed include setup costs and NRE in addition to fabrication and assembly of the carrier boards and FEM cards.

4.0.12 SVX4 Production

The full MPC-EX detector will require 848 SVX4 ASICS (two per MRC, including spares). At the present time the PHENIX Collaboration has approximately 283 SVX4.2b and 4.2a (combined). This is not sufficient for the full detector, so a production run for additional SVX4's will be required.

We have investigated the availablity of the SVX4.2b masks and design files with contacts at FNAL and LBNL. Unfortunatley, it appears that the actual production masks used are no longer available, although the production design files for the masks are. This will require an additional cost of $150K to produce the masks, and $50K for a 12 wafer production run. A production run guarantees at least 6 good wafers. With 312 SVX4's per wafer, and assuming a 75of the SVX4's on each wafer, this will yield a minimum of 1400 SVX4.2b ASICS. A single production run should provide sufficient SVX4's for the requirements of the MPC-EX, within a comfortable margin.

4.0.13 Slow Controls

Slow control cards will be necessary to download serial data to the SVX4's on the MRC. We estimate the costs for these cards at $1K each (production plus components). In addition, BIAS voltage supplies will be necessary for the minipad sensors. The costs listed are based on the price of the same supplies used for the PHENIX VTX detector (TTI model PLH250P).

4.0.14 Labor

This budget estimate includes labor costs for two items: the construction of the support structures, and the assembly and installation of the detector. Other steps in the detector construction, namely the assembly of the silicon modules, are planned to take place at the participating universities, and accordingly are considered in-kind contributions not charged to the project.

The assembly of the MPC-EX bricks to take place at BNL, using the pre-assembled modules and machined tungsten plates. The labor estimate assumes 3 months of a technician at 30%, and a full time graduate student for the same time period.

The support structure labor estimate includes construction, assembly, installation and quality assurance of the detector support structure. It assumes 100 hours of machine shop time, 20 days of a mechanical engineer and a mechanical technician at 30%, and 1 week of a full time graduate student. The detector installation estimate assumes 8 weeks of a mechanical engineer and a mechanical technician at 50%, 4 weeks of an electrical technician at 50%, and 2 weeks of a graduate student at 20%.

Chapter 5

Project Management

The organization and management of the MPC-EX effort is embedded in the management structure of the PHENIX experiment, which is part of the BNL RHIC project. The management organization satisfies a number of requirements including an interface to the existing RHIC and PHENIX management structure and roles and responsibilities within the existing PHENIX subsystem structure. Particular attention has been paid to the fact that a significant portion of the project effort is carried by PHENIX groups belonging to the international component of the PHENIX collaboration. Deliverables, responsibilities for deliverables and the accountability of the participating institutions are defined. These responsibilities will be formalized in memoranda of understanding (MOU's) between PHENIX and the participating institutions. In this section, we outline our proposed management organization and delineate responsibilities within the project.

5.0.15   PHENIX Management Structure

The MPC-EX project is part of the PHENIX project and as such integrated into the PHENIX management structure as described by the PHENIX bylaws. The PHENIX Collaboration Management has overall responsibility for the successful execution of the scientific operation of the PHENIX detector. Barbara Jacak (Stony Brook) is the PHENIX Spokesperson.

The PHENIX Detector Council (DC) will advise PHENIX management on the design, construction, and integration of the MPC-EX. The DC is chaired by the PHENIX Operations Manager (Edward O'Brien). The MPC-EX subsystem manager will serve as a member of the DC.

5.0.16   PHENIX Subsystem Leadership

We expect that the MPC-EX project will be funded through BNL beginning in January 2012. A successful completion of the MPC-EX will require close collaboration between participating institutions with a well-defined matrix of responsibilities and contributions in terms of deliverables. These deliverables and planned sources of contributions are outlined below. Within PHENIX the responsibility for the MPC-EX subsystem will be shared by the subsystem leader, John Lajoie (ISU) and his deputies, Edouard Kistenev (BNL) and Richard Seto (UCR). The subsystem leader reports to PHENIX PM and will represent the MPC-EX in the PHENIX DC.

5.0.17   Role of BNL

Because we expect that all funding for this effort will be directed through the BNL Physics Department, BNL line management will have ultimate fiscal and managerial responsibility for the construction of the MPC-EX and for its subsequent operation.

Fig. 5.1 shows a management chart of the MPC-EX project. The subsystem manager has general responsibility for the implementation of the project and is assisted by a deputy. In addition the manager and his deputies will have fiscal responsibilities. Similar to other upgrade projects in PHENIX, the PHENIX operations manager will assist the project in all integration matters and is responsible for the installation of the detector into the PHENIX experiment and for the safety of operations. The institutions that will participate in the implementation of individual tasks are given in the bottom of every task block in Fig. 5.2. PHENIX safety, DAQ, and infrastructure are common to all subsystems, so they are not listed as an explicit part of MPC-EX management.

5.0.18   Specification of Deliverables

The MPC-EX is divided into subprojects, which themselves are divided into tasks. The main tasks identified as blocks in Fig. 5.2 are closely related to deliverables, which need to be completed before the MPC-EX construction project can be considered complete. Below are the major deliverables and responsible institutions, along with a brief review of institutional responsibilities.

Preshower Detector

- Silicon minipad sensors designed and implemented to the specification: **BNL/Yonsei**

- Evaluation of production sensors: **Ewah/Hanyang**

- Detector Electronics
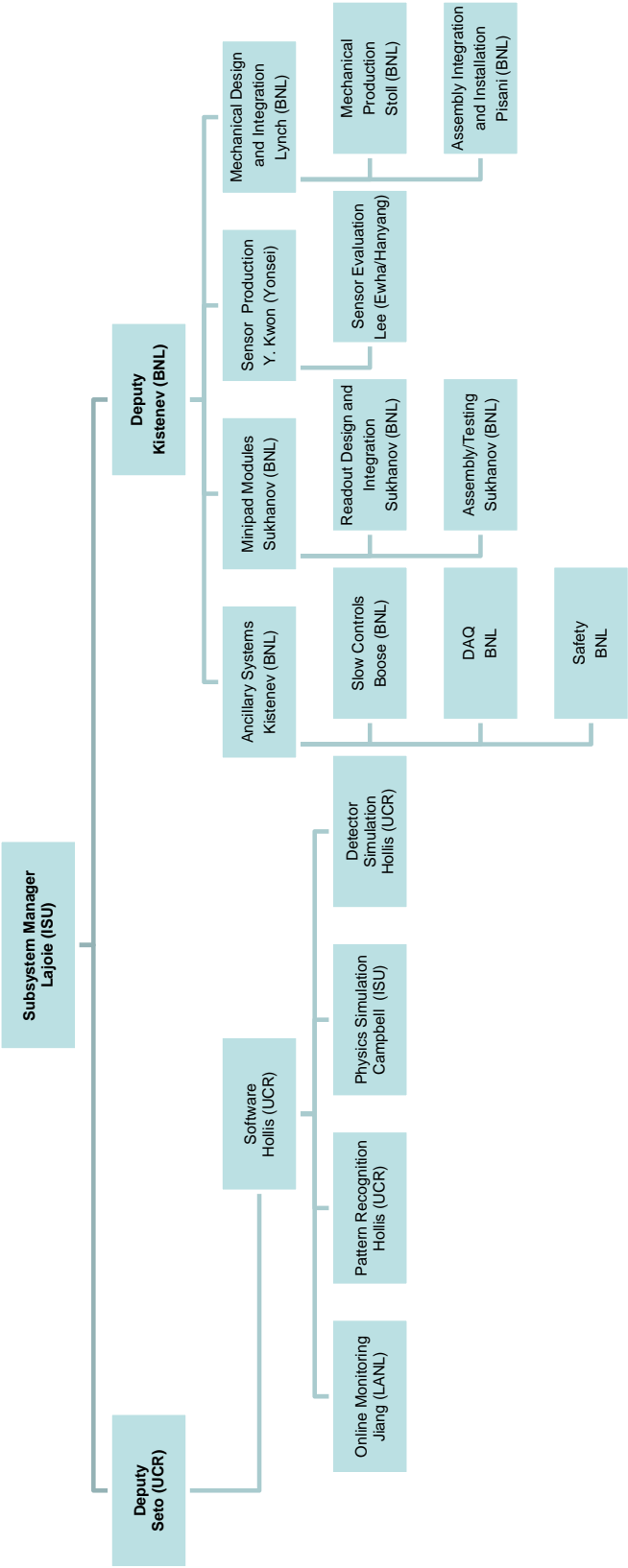
Figure 5.1: Management chart of the MPC-EX project.
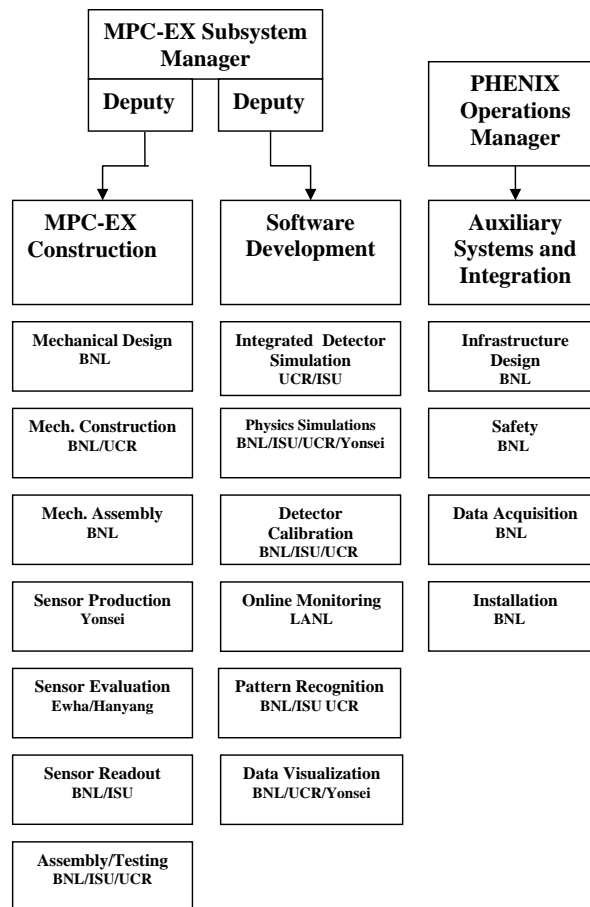
Figure 5.2: Institutional tasks for the MPC-EX project.

  – Readout units for minipad detectors: **BNL**

- Support structure: **BNL/UCR**

- Preshower mechanical components: **BNL**

- Assembly and testing of minipad modules **BNL/UCR/ISU**

- Assembly and testing of detector: **BNL/UCR/ISU**

DAQ System

- Data collection modules: **BNL/Nevis**

- Software development for data collection, monitoring and analysis: **BNL/UCR/LANL**

Auxiliary Systems and Integration

- System support requirements specification, including heat loads, power distribution, mechanical tolerances and grounding scheme: **BNL**

- Ancillary systems, including power distribution and cooling system: **BNL**

- Installation and integration:**BNL**

- Commissioning of full detector system: **BNL/UCR/ISU**

5.1 Institutional Involvement

Currently six institutions with over 45 individuals are involved in the MPC-EX project. The different institutions bring in diverse research backgrounds, physics interests and expertise, which form a broad base to carry out the proposed project. Each group assumes specific responsibilities and will participate actively in the MPC-EX project. According to their expertise and interests these groups will be involved in construction, installation, commissioning, operation, and data analysis. Formal commitments of the involved institutions will be specified in Memoranda of Understanding (MoU). Many of these groups have been actively involved in the R&D effort through institutional contributions, while others have joined the project only recently. Below are brief descriptions of expertise and potential involvement of the institutions.

5.1.1 US Based Institutions

The BNL Instrumentation Division have joined the MPC-EX project because of their interest in the technological development, but are not members of the PHENIX collaboration.

The PHENIX group at University of California, Riverside has taken primary responsibility for Simulations and Software development, and is heavily involved with ongoing MPC-EX related R&D. As a subsystem deputy, UCR group leader Richard Seto hasplayed a leading role in the management of the MPC-EX, and was instrumental in bringing the project to the proposal stage.

The BNL physics group brings management and physics experience and broad experience with silicon detector and calorimeter technology. Individual group members bring specific technical skills that will be important for the successful construction, installation, commissioning and operation of the MPC-EX in the RHIC environment. Edouard Kistenev of BNL has taken a leading role in developing the concept and design of the MPC-EX.

The PHENIX Group, led by Don Lynch from the BNL Physics Department provides infrastructure and technical support as part of Systems Engineering and Integration (SE&I)

for the entire PHENIX experiment. It has a staff of mechanical and electrical engineers and a group of experienced technicians who are intimately familiar with the detector, and work closely with the BNL Collider-Accelerator Department for operations and any modifications to its present design. They designed much of the infrastructure for the baseline detector, including racks, cable trays, electrical power, cooling, access, safety systems and numerous other services, and carried out the installation of all of the present subsystem detectors. This group will now be closely involved with the design of the infrastructure and support for the MPC-EX, and with its installation into PHENIX.

The PHENIX group from Iowa State University will take responsibility for overall management of the MPC-EX project, as well as contributing to the software, simulations, and physics analysis efforts. As subsystem manager, John Lajoie has played a leading role in the preparation of the proposal and in studying many of the relevant physics topics, particularly related to spin.

The PHENIX group from Los Alamos National Laboratory has extensive experience in both spin and cold nuclear matter physics, and will take responsibility for the online monitoring and slow controls software for the experiment. They will also be invloved in physics simulations and data analysis.

The BNL PHENIX group has primary responsibility for a number of major subsystems. These include Electronics Facilities and Infrastructure (EF&I), Online Computing Systems (ONCS) and Offline Computing. These groups will participate in the electronic integration and readout of the MPC-EX detector into the PHENIX data acquisition system, and will be involved with track reconstruction and offline data analysis.

The BNL PHENIX group will also serve as host institution for the project and will provide the lab space for the final detector assembly and testing.

5.1.2   International Participation

The Korean groups at Yonsei University, led by Ju Kang and Yongil Kwon and Ewha University, led by K.I. Hahn, and Hanyang University, led by Y.K. Kim have become involved in the development of the minipad sensors. The group is currently working on prototyping the MPC-EX minipad and has taken a major responsibility of a test beam prototype to be put into the CERN test beam in September. The group at Yonsei will also take major responsibilities in software and physics simulations.

Appendix A

Event Rates

A.0.3   Event Rates

In this section we estimate the event rates for selected processes in p+p and d+Au collisions. All rates are for an MPC-EX in both the south and north arms in p+p, and in the deuteron going direction only in the case of d+Au collisions. In calculating event rates we start with latest guidance document from the RHIC Collider Accelerator Division (CAD) [24], which lists the store average luminosity for the various species and the delivered luminosity per week. We then assume a 60% up time for the PHENIX detector, a DAQ live time of 90%, and minbias trigger efficiencies (see Table A.2) for a 12 week run to obtain the luminosity sampled by PHENIX (see Table A.2). Note that we do not include an event vertex cut efficiency, as the MPC-EX analysis will be able to use essentially the full vertex distribution delivered by RHIC.

NLO cross sections for π^0, direct and fragmentatation photons at 200GeV were obtained from Werner Vogelsang, for proton-proton collisions at 200GeV. These cross sections were calculated using the CTEQ6M5 pdf's, with the scale $\mu = p_T$, and no isolation cuts for the photons. The π^0 cross sections were calculated using the DSS fragmentation functions.These cross sections are plotted in Figure A.1. As one approaches very high p_T (near the luminosity limit) the direct photon production surpasses the pizero production

Table A.1: Efficiency factors used in the rate calculations. For A+A collisions the minimum bias trigger formed by the BBC is very close to 100% efficient, however in p+p and d+A collisions this is not the case.

Species	p+p 200 GeV	p+p 500 GeV	d+Au	Cu+Cu	Au+Au
min bias trigger eff	0.75	0.75	0.90	1.0	1.0

Table A.2: Luminosity guidance from CAD for RHIC. We then assume a 12 week run and a 60% uptime for PHENIX, a DAQ live time of 90% and a minbias trigger efficiency to obtain a PHENIX sampled integrated luminosity.

Species CM Energy	p+p 200 GeV	p+p 500 GeV	d+Au 200 GeV	Cu+Cu 200 GeV	Au+Au 200 GeV
store average luminosity $(s^{-1}cm^{-2})$	3×10^{31}	1.2×10^{32}	1.8×10^{29}	5×10^{28}	3.5×10^{27}
interaction rate (kHz)	1260	4200	328	124	17
lum/wk (pb^{-1}wk^{-1})	10	40	0.060	0.016	0.0011
int. sampled lum (pb^{-1})	49	190	0.350	0.100	0.0071

due to the fact that the pizeroes arise from fragmentation.
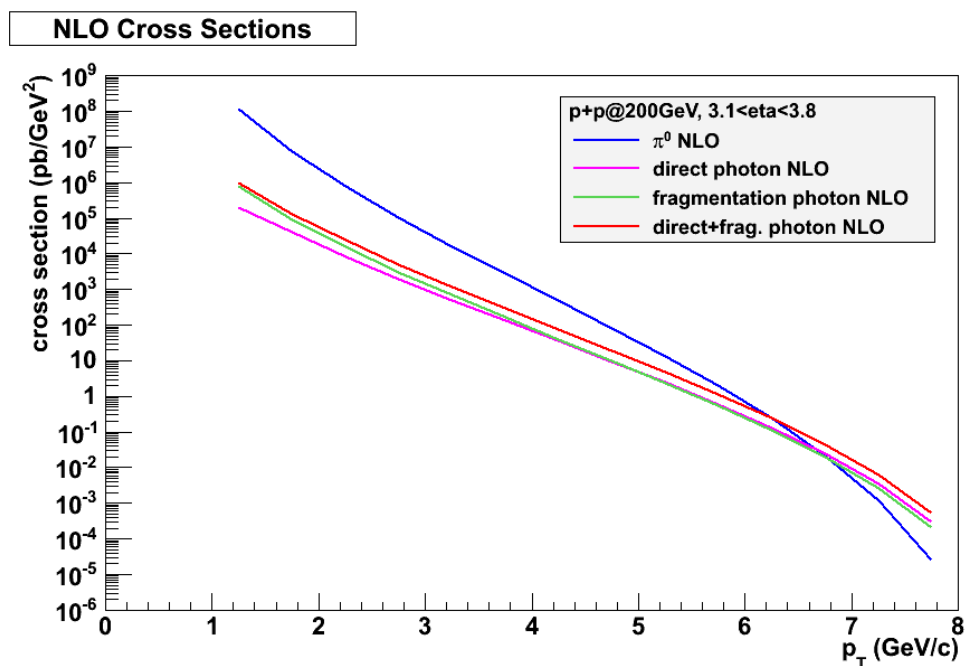

Figure A.1: NLO cross sections for pizero, direct photons, and fragmentation photons in the MPC-EX acceptance at 200GeV as a function of transverse momentum. From Werner Vogelsang.
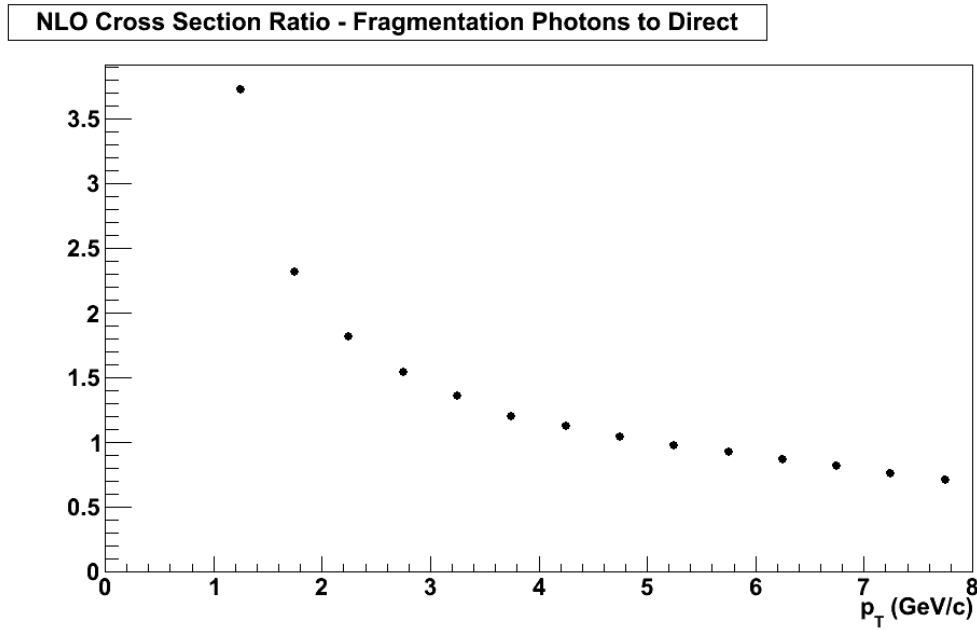
Figure A.2: Ratio of the NLO cross sections for fragmentation photons to direct photons in the MPC-EX acceptance at 200GeV as a function of transverse momentum. From Werner Vogelsang.

In order to estimate the available statistics in a d+Au run we start with the NLO cross sections and assume $< N_{coll} >$ scaling so that the cross sections are scaled up by a factor of 8.3, the mean number of binary collisions in a minbias d+Au collsions as determined by a Galuber simulation [1]. The estimated statistics in a RHIC d+Au run with $350nb^{-1}$ PHENIX integrated sampled luminosity (consistent with Table A.2) is shown in Table A.3 (without correction for suppression effects that will be present in d+Au collisions).

The estimated statistics in a transversely polarized RHIC p+p run with $49pb^{-1}$ PHENIX integrated sampled luminosity (consistent with Table A.2) is shown in Table A.4.

A.0.4   Triggering

Need to say something here about how we will trigger for the direct photon and jet samples, thresholds, rejections, etc.

Table A.3: Estimated statistics for dAu collisions, assuming PHENIX efficiencies (vertex and minbias trigger efficiency) but no correction for the MPC-EX reconstruction efficiency. These numbers are not adjusted for any suppression or shadowing effects.

p_T (GeV/c)	π^0	photons (direct + frag.)	photon/π^0
1.0-1.5	9.2×10^8	7.7×10^6	0.0084
1.5-2.0	8.2×10^7	1.5×10^6	0.018
2.0-2.5	1.1×10^7	3.5×10^5	0.031
2.5-3.0	1.8×10^6	9.0×10^4	0.050
3.0-3.5	3.3×10^5	2.5×10^4	0.075
3.5-4.0	6.5×10^4	7.1×10^3	0.11
4.0-4.5	1.3×10^4	2.1×10^3	0.16
4.5-5.0	2.5×10^3	600	0.24
5.0-5.5	450	160	0.36
5.5-6.0	73	42	0.58
6.0-6.5	10	10	1.0

Table A.4: Estimated statistics for p+p collisions, assuming PHENIX efficiencies (vertex and minbias trigger efficiency) but no correction for the MPC-EX reconstruction efficiency.

p_T (GeV/c)	π^0	photons (direct + frag.)
1.0-1.5	3.1×10^{10}	2.6×10^8
1.5-2.0	2.8×10^9	5.0×10^7
2.0-2.5	3.7×10^8	1.2×10^7
2.5-3.0	6.1×10^7	3.0×10^6
3.0-3.5	1.1×10^7	8.4×10^6
3.5-4.0	2.2×10^6	2.4×10^5
4.0-4.5	4.4×10^5	7.0×10^5
4.5-5.0	8.5×10^5	2.0×10^4
5.0-5.5	1.5×10^4	5.5×10^3
5.5-6.0	2.5×10^3	1.4×10^3
6.0-6.5	330	330
6.5-7.0	31	63
7.0-7.5	2	9

Appendix B

MPC-EX Participants – October 2011

Brookhaven National Laboratory,
Upton, NY 11973, USA
E. Kistenev, A. Sukhanov

Ewha Womens University,
Seoul, Korea
K.I. Hahn, D.H. Kim, S.Y. Han

Hanyang University,
Seoul, Korea
B.H. Kang, J.S. Kang, Y.K. Kim, J.S. Park

Iowa State University,
Ames, Iowa 50011, USA
S. Campbell, J.G. Lajoie, R. McKay, J. Perry, A. Timilsina

Los Alamos National Laboratory,
Los Alamos, New Mexico 87545, USA
J. Huang, X. Jiang, M. Leitch, M. Liu

University of California - Riverside,
Riverside, California 92521, USA
K.N. Barish, D. Black, L. Garcia, R.S. Hollis, A. Iordanova, R. Seto, W. Usher

Yonsei University, IPAP
Seoul, Korea
J.H Do, J.H. Kang, H.J. Kim, Y. Kwon, S.H. Lim, M. Song

Bibliography

[1] Phenix analysis notes 633, 381 and 295. A.0.3

[2] **STAR Collaboration Collaboration**, B. I. Abelev *et al.* Forward neutral-pion transverse single-spin asymmetries in $p + p$ collisions at $\sqrt{s} = 200$ GeV. *Phys. Rev. Lett.*, 101:222001, Nov 2008. Available from: `http://link.aps.org/doi/10.1103/PhysRevLett.101.222001, doi:10.1103/PhysRevLett.101.222001`. 1.2.1, 1.7, 1.8, 1.10

[3] **STAR Collaboration**, D.L. Adams *et al.* Analyzing power in inclusive π^+ and π^- production at high x_f with a 200 gev polarized proton beam. *Phys. Lett. B*, 265:462–466, 1991. 1.2.1

[4] A. Adare *et al.* Cold Nuclear Matter Effects on J/psi Yields as a Function of Rapidity and Nuclear Geometry in Deuteron-Gold Collisions at sqrt($s_N N$) = 200 GeV. 2010. `arXiv:1010.1246`. 1.1.1, 1.1.1

[5] **PHENIX Collaboration Collaboration**, A. Adare *et al.* Suppression of back-to-back hadron pairs at forward rapidity in d+Au Collisions at $\sqrt{s_{NN}}$ = 200 GeV. 2011. * Temporary entry *. `arXiv:1105.5112`. 1.1.1, 1.1.1

[6] **PHENIX Collaboration Collaboration**, Stephen Scott Adler *et al.* Absence of suppression in particle production at large transverse momentum in S(NN)**(1/2) = 200-GeV d + Au collisions. *Phys.Rev.Lett.*, 91:072303, 2003. `arXiv:nucl-ex/0306021, doi:10.1103/PhysRevLett.91.072303`. 1.1.1

[7] **The HERMES Collaboration Collaboration**, A. Airapetian *et al.* Single-spin asymmetries in semi-inclusive deep-inelastic scattering on a transversely polarized hydrogen target. *Phys. Rev. Lett.*, 94:012002, Jan 2005. Available from: `http://link.aps.org/doi/10.1103/PhysRevLett.94.012002, doi:10.1103/PhysRevLett.94.012002`. 1.2.1, 1.13

[8] A. Airapetian *et al.* Effects of transversity in deep-inelastic scattering by polarized protons. *Physics Letters B*, 693(1):11 − 16, 2010. Available from: `http://www.sciencedirect.com/science/article/pii/S0370269310009457, doi:10.1016/j.physletb.2010.08.012`. 1.2.1

[9] M. Alekseev *et al*. Collins and sivers asymmetries for pions and kaons in muon-deuteron dis. *Physics Letters B*, 673(2):127 – 135, 2009. Available from: `http://www.sciencedirect.com/science/article/pii/S0370269309000884`, `doi:10.1016/j.physletb.2009.01.060`. 1.2.1

[10] M.G. Alekseev *et al*. Measurement of the collins and sivers asymmetries on transversely polarised protons. *Physics Letters B*, 692(4):240 – 246, 2010. Available from: `http://www.sciencedirect.com/science/article/pii/S0370269310009184`, `doi:10.1016/j.physletb.2010.08.001`. 1.2.1, 1.2.1

[11] M. Anselmino, M. Boglione, U. D'Alesio, A. Kotzinian, F. Murgia, *et al*. Transversity and Collins functions from SIDIS and e+ e- data. *Phys.Rev.*, D75:054032, 2007. `arXiv:hep-ph/0701006`, `doi:10.1103/PhysRevD.75.054032`. 3.4.1

[12] M. Anselmino, M. Boglione, U. D'Alesio, A. Kotzinian, F. Murgia, *et al*. Update on transversity and Collins functions from SIDIS and e+ e- data. *Nucl.Phys.Proc.Suppl.*, 191:98–107, 2009. `arXiv:0812.4366`, `doi:10.1016/j.nuclphysbps.2009.03.117`. 3.4.1

[13] M. Anselmino, M. Boglione, U. D'Alesio, A. Kotzinian, F. Murgia, A. Prokudin, and S. Melis. Update on transversity and collins functions from sidis and data. *Nuclear Physics B - Proceedings Supplements*, 191(0):98 – 107, 2009. ¡ce:title¿Proceedings of the Ringberg Workshop¡/ce:title¿ ¡ce:subtitle¿New Trends in HERA Physics 2008¡/ce:subtitle¿. Available from: `http://www.sciencedirect.com/science/article/pii/S0920563209003727`, `doi:10.1016/j.nuclphysbps.2009.03.117`. 1.2.1

[14] Nestor Armesto. Nuclear shadowing. *J. Phys.*, G32:R367–R394, 2006. `arXiv:hep-ph/0604108`, `doi:10.1088/0954-3899/32/11/R01`. 1.1.1

[15] **BRAHMS Collaboration Collaboration**, I. Arsene *et al*. Quark gluon plasma and color glass condensate at RHIC? The Perspective from the BRAHMS experiment. *Nucl.Phys.*, A757:1–27, 2005. `arXiv:nucl-ex/0410020`, `doi:10.1016/j.nuclphysa.2005.02.130`. 1.1.1, 1.1.1

[16] **BRAHMS Collaboration Collaboration**, I. Arsene *et al*. Single-transverse-spin asymmetries of identified charged hadrons in polarized pp collisions at $\sqrt{s} = 62.4$ GeV. *Phys. Rev. Lett.*, 101:042001, Jul 2008. Available from: `http://link.aps.org/doi/10.1103/PhysRevLett.101.042001`, `doi:10.1103/PhysRevLett.101.042001`. 1.2.1

[17] A. Bacchetta *et al*. Sivers single-spin asymmetry in photon-jet production. *Phys. Rev. Lett.*, 99:212002, 2007. 3

[18] Alessandro Bacchetta, Aurore Courtoy, and Marco Radici. First glances at the transversity parton distribution through dihadron fragmentation functions. *Phys. Rev. Lett.*, 107:012001, Jun 2011. Available from: `http://link.aps.org/doi/10.1103/PhysRevLett.107.012001`, `doi:10.1103/PhysRevLett.107.012001`. 1.2.1

[19] F. Bradamante. Measurement of the collins asymmetries on transversely polarised protons. *Transversity-2011 Workshop*, 2011. 1.2.1, 1.11, 1.13

[20] Stanley J. Brodsky, Dae Sung Hwang, and Ivan Schmidt. Final-state interactions and single-spin asymmetries in semi-inclusive deep inelastic scattering. *Physics Letters B*, 530(1-4):99 – 107, 2002. Available from: `http://www.sciencedirect.com/science/article/pii/S0370269302013205`, `doi:10.1016/S0370-2693(02)01320-5`. 1.2.1, 1.2.1

[21] Umberto D'Alesio and Francesco Murgia. Parton intrinsic motion in inclusive particle production: unpolarized cross sections, single spin asymmetries, and the sivers effect. *Phys. Rev. D*, 70:074009, Oct 2004. Available from: `http://link.aps.org/doi/10.1103/PhysRevD.70.074009`, `doi:10.1103/PhysRevD.70.074009`. 1.2.1, 1.7, 1.8

[22] Danil and Boer. On a possible node in the sivers and qiusterman functions. *Physics Letters B*, 702(4):242 – 245, 2011. Available from: `http://www.sciencedirect.com/science/article/pii/S0370269311007842`, `doi:10.1016/j.physletb.2011.07.006`. 1.2.1

[23] K.J. Eskola, H. Paukkunen, and C.A. Salgado. EPS09: A New Generation of NLO and LO Nuclear Parton Distribution Functions. *JHEP*, 0904:065, 2009. `arXiv:0902.4154`, `doi:10.1088/1126-6708/2009/04/065`. 1.1.1, 1.1.2, 3.3.3

[24] W. Fisher, T. Roser, M. Bai, J. Alessi, H. Huang, C. Montag, M. Blaskiewicz, and V. Schoefer. Rhic collider projections (fy2012-fy2016), 14 october 2011. A.0.3

[25] Zhong-Bo Kang, Jian-Wei Qiu, Werner Vogelsang, and Feng Yuan. Observation concerning the process dependence of the sivers functions. *Phys. Rev. D*, 83:094001, May 2011. Available from: `http://link.aps.org/doi/10.1103/PhysRevD.83.094001`, `doi:10.1103/PhysRevD.83.094001`. 3

[26] Dmitri Kharzeev, Eugene Levin, and Marzia Nardi. QCD saturation and deuteron nucleus collisions. *Nucl.Phys.*, A730:448–459, 2004. `arXiv:hep-ph/0212316`, `doi:10.1016/j.nuclphysa.2004.06.022,10.1016/j.nuclphysa.2004.06.022`. 1.1.1

[27] Dmitri Kharzeev and Marzia Nardi. Hadron production in nuclear collisions at RHIC and high density QCD. *Phys.Lett.*, B507:121–128, 2001. `arXiv:nucl-th/0012025`, `doi:10.1016/S0370-2693(01)00457-9`. 1.1.1

[28] Chris Kouvaris, Jian-Wei Qiu, Werner Vogelsang, and Feng Yuan. Single transverse-spin asymmetry in high transverse momentum pion production in *pp* collisions. *Phys. Rev. D*, 74:114013, Dec 2006. Available from: `http://link.aps.org/doi/10.1103/PhysRevD.74.114013`, `doi:10.1103/PhysRevD.74.114013`. 1.2.1, 1.7, 1.8

[29] Matthew Luzum and Paul Romatschke. Conformal Relativistic Viscous Hydrodynamics: Applications to RHIC results at s(NN)**(1/2) = 200-GeV. *Phys.Rev.*, C78:034915, 2008. `arXiv:0804.4015`, `doi:10.1103/PhysRevC.78.034915,10.1103/PhysRevC.79.039903,10.1103/PhysRevC.78.034915,10.1103/PhysRevC.79.039903`. 1.1.1, 1.2

[30] Larry D. McLerran and Raju Venugopalan. Computing quark and gluon distribution functions for very large nuclei. *Phys. Rev.*, D49:2233–2241, 1994. `arXiv:hep-ph/9309289`, `doi:10.1103/PhysRevD.49.2233`. 1.1.1

[31] **Jefferson Lab Hall A Collaboration Collaboration**, X. Qian *et al*. Single spin asymmetries in charged pion production from semi-inclusive deep inelastic scattering on a transversely polarized ^{3}He target at $Q^2 = 1.4\text{\textasciicaron}2.7$ gev^2. *Phys. Rev. Lett.*, 107:072003, Aug 2011. Available from: `http://link.aps.org/doi/10.1103/PhysRevLett.107.072003`, `doi:10.1103/PhysRevLett.107.072003`. 1.2.1

[32] John P. Ralston and Davison E. Soper. Production of dimuons from high-energy polarized proton proton collisions. *Nucl. Phys.*, B152:109, 1979. 1, 1.2.1

[33] Torbjorn Sjostrand *et al*. High-energy-physics event generation with pythia 6.1. *Comput. Phys. Commun.*, 135:238–259, 2001. `arXiv:hep-ph/0010017`. 1.2.1, 1.10

[34] Torbjorn Sjostrand, Stephen Mrenna, and Peter Z. Skands. PYTHIA 6.4 Physics and Manual. *JHEP*, 0605:026, 2006. `arXiv:hep-ph/0603175`, `doi:10.1088/1126-6708/2006/05/026`. 3.4.1

[35] Mark Strikman and Werner Vogelsang. Multiple parton interactions and forward double pion production in pp and dA scattering. *Phys.Rev.*, D83:034029, 2011. `arXiv:1009.6123`, `doi:10.1103/PhysRevD.83.034029`. 1.1.1